High-Order Integral Equation Methods for Diffraction Problems Involving Screens and Apertures

Thesis by

Stéphane K. Lintner

In Partial Fulfillment of the Requirements

for the Degree of

Doctor of Philosophy

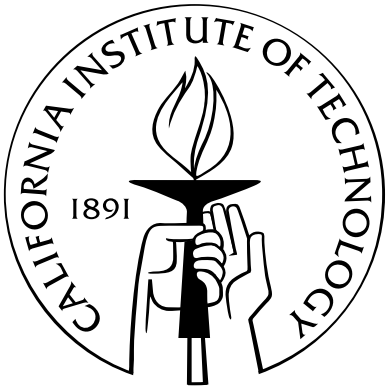

California Institute of Technology

Pasadena, California

2012

(Defended June 1 , 2012)

To my beloved family

Acknowledgements

I will remain forever in debt to my wife Marta for bearing with my desire to bring this thesis to a full completion. Nor will I ever be able to thank enough my advisor, mentor and friend, Prof. Oscar P. Bruno, for his guidance and unfaltering patience over a decade-long collaboration which, having started over an unforgettable summer internship, has continued through my five years in Pasadena and what has, by now, turned into five years on Wall Street. My gratitude also goes to the dear group of friends I met during my years at Caltech, all of whom I continue to be incredibly close to as well. Caltech is a wonderful institution to pursue graduate studies; it provided me with a few years of exposure to cutting-edge sciences and unbounded intellectual freedom, the memory of which I shall cherish for the rest of my life. The wonderful flexibility of Caltech's program is perhaps best illustrated by the brief, yet extremely enriching opportunity I had to work for a period of eight months at Caltech's photonics lab run by Pr. Changhuei Yang, to whom I am deeply grateful for his kindness. I would also like to thank Pr. Yves Meyer and Pr. Jean-Michel Morel at the Centre des Mathematiques et de Leurs Applications (CMLA), at the Ecole Normale Supérieure de Cachan in France, for encouraging me and supporting my decision to apply to Caltech and pursue a doctoral degree abroad.

Finally, I owe most of what I know and care for to my parents and sisters who are too far away; I look forward to spending more time with all of you.

Abstract

This thesis presents a novel approach for the numerical solution of problems of diffraction by infinitely thin screens and apertures. The new methodology relies on combination of *weighted versions* of the classical operators associated with the Dirichlet and Neumann open-surface problems. In the two-dimensional case, a rigorous proof is presented, establishing that the new weighted formulations give rise to second-kind Fredholm integral equations, thus providing a generalization to open surfaces of the classical closed-surface Calderón formulae. High-order quadrature rules are introduced for the new weighted operators, both in the two-dimensional case as well as the scalar three-dimensional case. Used in conjunction with Krylov subspace iterative methods, these rules give rise to efficient and accurate numerical solvers which produce highly accurate solutions in small numbers of iterations, and whose performance is comparable to that arising from efficient high-order integral solvers recently introduced for closed-surface problems. Numerical results are presented for a wide range of frequencies and a variety of geometries in two- and three-dimensional space, including complex resonating structures as well as, for the first time, accurate numerical solutions of classical diffraction problems considered by the 19th-century pioneers: diffraction of high-frequency waves by the infinitely thin disc, the circular aperture, and the two-hole geometry inherent in Young's experiment.

Contents

List of Figures

List of Tables

Chapter 1

Diffraction, Screens and Apertures

Lumen propagatur seu diffunditur non solum Directe, Refracte, ac Reflexe, sed etiam alio quodam Quarto modo, DIFFRACTE —1665, Grimaldi on the first recorded observation of the phenomenon of diffraction

1.1 Introduction

In this thesis, we present a novel and efficient approach for the numerical solution of scattering problems of acoustic and electromagnetic waves by *infinitely thin* surfaces; depending on the domain of application (optics, antenna design, photonics, radar detection) such problems are also referred to as screen diffraction problems.

Mathematically, screen problems are modeled in terms of *open*-surface boundary value problems, and have been notoriously more challenging to solve than *closed*-surface problems[1]. The latter have been extensively studied over the last century: existence and regularity of solutions for the closed-surface case are well established, and the past twenty years have seen the emergence of algorithms which can accurately solve problems of acoustic and electromagnetic scattering by closed scatterers that are hundreds of wavelengths in size [13, 14, 18, 67]. Screen problems have eluded a similar treatment: while it has long been known that solutions exist, their regularity properties were not fully understood until recently [42], and only numerical solutions for open-surface problems of very low frequencies had previously been presented with any level of accuracy, mostly in the simpler context of open arcs in two-dimensional space.

Infinitely thin screens are of course idealized objects: any physical body presents a

[1] A closed surface separates space into two distinct region: an interior domain, and an exterior domain. An open surface, such as an infinitely thin disc, is by definition, not closed.

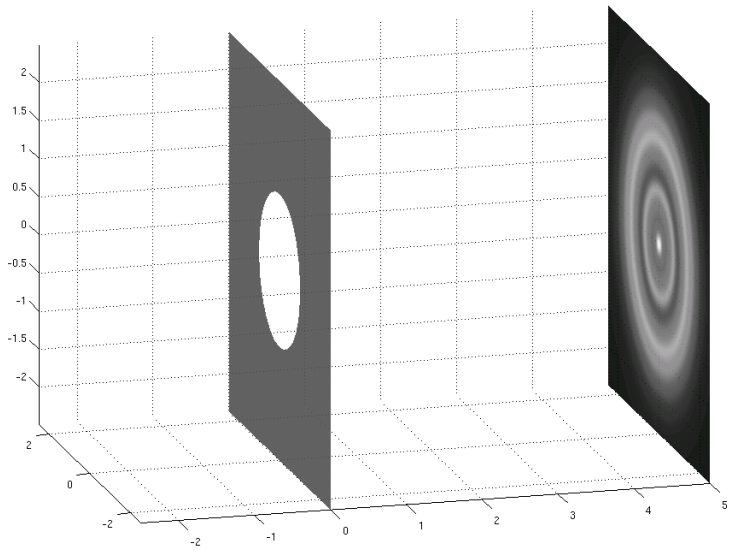

Figure 1.1: Classical screen diffraction problem: a circular aperture in an infinitely thin screen

certain thickness and could therefore be treated, in theory, as a closed surface. From a practical standpoint, however, an object whose thickness is negligible with respect to its other dimensions presents serious difficulties, which arise from the extreme proximity of the two scattering sides of the surface, as well as the existence of points of very large curvature around the edges. Closed-surface resolution methods for such problems require prohibitively large number of discretization points and large numbers of iterations if used in conjunction with Krylov-subspace linear iteration techniques.

Yet, very thin objects do play a critical role in a wide variety of modern applications, ranging from small-aperture diffraction devices in high-precision interferometric telescopes, to thin antenna design for wireless communications, airplane tails and wing tips scattering signature, photonic near-field aperture calculations, to cite but a few examples. In all of these applications, the thickness of the scattering body is such that modeling of the object as an open surface (essentially neglecting its thickness altogether) is a reasonable approach—provided, of course, that an *efficient* mathematical and numerical treatment of open surfaces exists.

As it happens, however, the treatment of open surfaces has historically been challenging, even for such simple shapes as those first considered in the early 19th century: the disc and

the circular aperture. These two classical problems alone, which have been the subject of multiple studies over the last two hundred years (each providing particular asymptotic or approximate solutions under various regimes or in various regions of space), had, until the present study, lacked an accurate methodology for numerical solution. It is not a coincidence therefore to find Born and Wolf's treatise on optics [6] opening the chapter on diffraction with the following remark: *Diffraction problems are amongst the most difficult ones encountered in optics. Solutions which, in some sense, can be regarded as rigorous are very rare in diffraction theory. The first such solution was given as late as 1896 by A. Sommerfeld when, in an important paper, he discussed the diffraction of a plane wave by a perfectly conducting semi-infinite plane screen. Since then rigorous solutions of a small number of other diffraction problems (mainly two-dimensional) have also been found, but because of mathematical difficulties, approximate methods must be used in most cases of practical interest.*

The work presented in the upcoming chapters aims at analyzing and resolving some of those 'mathematical difficulties' in the context of screens: it will be shown that those difficulties can be solved by means of a novel set of weighted integral operators, and that high-order numerical methods can in fact be developed to produce highly accurate solutions to open-surface problems.

1.2 Historical Overview of Diffraction and Wave Scattering Problems

This section provides an overview of the history of diffraction and scattering problems; given the breadth of the domain, the section is bound to omit many important aspects.

1.2.1 Early days of diffraction

Prior to the mid-seventeenth century, light was commonly understood to be a stream of particles whose trajectory paths were dictated by simple geometrical laws: in an isotropic medium, the path is rectilinear, and at an interface between two media of different composition, an incoming ray is split into two new rays: a reflected ray and a refracted ray, the respective angles of which were known to follow Snell's law, which depends on the incident ray's angle with respect to the surface, and the refractive indices of the materials. Light

therefore could 1) propagate directly, 2) reflect, and 3) refract. In 1665 however, Francisco Grimaldi reported a fourth and completely different phenomenon [21], which he discovered through two experiments, which are described in what follows. In Grimaldi's first experi-

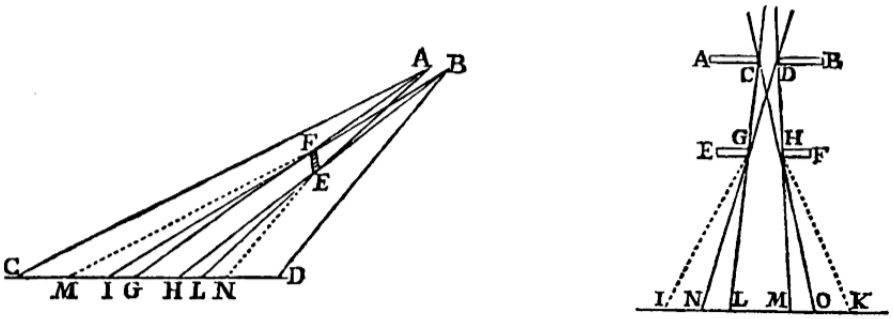

Figure 1.2: Grimaldi's two experiments, as depicted in his 1665 volume. Left: observation of diffraction fringes. Right: the observed shadow IK is larger than the geometrical shadow.

ment, illustrated on the left portion of Figure 1.2, Grimaldi allowed for a fine pencil of light to enter a dark room, and noted that a thin rod placed on the path of light generated a shadow whose intensity, instead of being uniform as predicted by the geometrical theory of rays, was instead variable, with noticeable fringes. Grimaldi's second experiment, in turn, involved two apertures of equal size, for which the illuminated area, the segment IK on the right of Figure 1.2, consistently appeared larger than the geometrical prediction. These two observations suggested that, upon interacting with the rod or the apertures, light was 'broken up'—or, in the Latin word coined by Grimaldi, 'diffracted' [21].

This new phenomenon seriously challenged the corpuscular model of light: Grimaldi provided detailed arguments to show that a stream of light made of particles could under no circumstances explain diffraction, and that light must therefore be explained in terms of waves. However, the rudimentary wave models of the time could not account for simple rectilinear propagation and the 18th century became the stage for intense debates as to the very nature of light; some in the steps of Newton continued to affirm a particle model which best explained the ray propagation, generally ignoring the phenomenon of diffraction, or accounting for it, in some unsatisfactory form or another (Newton referred to the phenomenon as 'inflexion', rather than diffraction). Hook, Huygens and others, in turn, developed increasingly complex wave models, without however being able to fully account for diffraction in a rigorous manner either [6, 38].

1.2.2 Poisson spot and Huygens-Fresnel principle

The debate on the nature of light was eventually ended with Fresnel's construction of the first mathematically robust wave theory, based on the principle bearing the Huygens-Fresnel name. Fresnel's famous mémoire was presented to the French Académie des Sciences as a contender for an 1819 prize for the best piece of work on the nature of light. As is well known [6, 38], his mémoire was at first dismissed by proponents of the particle theory (Poisson in particular) who noted that the framework implied the presence of a bright spot in the shadow area behind a circular disc, a fact which defeated common sense. Upon careful experimentation however, Arago confirmed shortly thereafter the existence of this very spot in practice, thus providing a spectacular validation of the wave theory, which prompted the scientific community to rapidly abandon the particle approach for the remaining of the century [2]–until the advent of modern quantum theory.

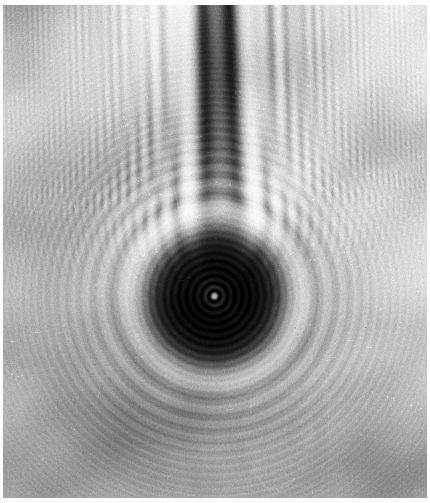

Figure 1.3: Experimental observation of the Poisson spot (compare to Figure 1.1). The upper artefact is due to the pin used to hold the diffracting disc. (Photograph graciously provided by Pr. Jones from Union College, Schenectady, NY.)

The *Huygens-Fresnel* principle at the heart of Fresnel's construction describes light in

[2] Anecdotally, we note the article [52] which places this famous story in a slightly different perspective: there was only one other contender for the prize besides Fresnel, and the contender's work was known to be fraught with deficiencies. The commission further consisted of a panel which, while being in its majority a strong proponent of a particle theory of light, was very close to Fresnel through the Ecole Polytechnique. In particular, the opinion of the panel, summarized over 9 pages, only dedicates two lines to the Poisson spot, and makes no reference to the Poisson shadow which was inferred by Arago to also appear in the illuminated area behind an aperture. According to [52] thus, Fresnel was bound to win; his work had also already been presented to the Académie in 1815, the 1818 mémoire was, to some extent, a more complete and very anticipated version.

terms of spherical 'wavelets' which interfere with each other in the direction of propagation, generating along the wavefront a new set of wavelets [6]. As such, the principle does not provide a complete description of waves and is difficult to apply in practice; yet, from it Fresnel was able to deduce that the diffracted field or 'perturbance' could be expressed entirely in terms of an integral along the diffracting screen of some 'diffraction coefficient' multiplied by a spherical point source located at the point of integration:

$$u(\mathbf{r}) = \int_{\Gamma} \chi(\mathbf{r}') \frac{e^{ik|\mathbf{r}-\mathbf{r}'|}}{|\mathbf{r}-\mathbf{r}'|} dS', \quad \mathbf{r} \quad \text{outside} \quad \Gamma \tag{1.1}$$

where $\mathbf{r}$ is a point located away from the diffracting screen, $\chi(\mathbf{r}')$ denotes the diffraction coefficient, and Γ is the diffracting surface. As we shall see, this integral representation still provides the basis of today's numerical methods.

1.2.3 Classical vector and scalar models of light

The decades that followed the work of Fresnel witnessed refinements of the Huygens-Fresnel model and the construction of increasingly complex mechanical models to explain the propagation of light in terms of waves in an elastic 'caloric' or 'aether' medium. In 1888, however, it was found by Hertz that light was in fact an electromagnetic wave: light's modes of propagation could therefore be fully described by Maxwell's equations, and thus, from a mathematical standpoint, the old problem of evaluating the diffraction of light had been finally cast in terms of well-defined general boundary value problems. As an example, the diffraction problem for a perfectly conducting body illuminated by a time-harmonic electromagnetic wave $(\mathbf{E}, \mathbf{H})$ which satisfies the time-harmonic Maxwell equations

$$\begin{cases} \operatorname{curl} \mathbf{H} = -ik\mathbf{E} \\ \operatorname{curl} \mathbf{E} = ik\mathbf{H}, \end{cases} \tag{1.2}$$

(where $k = \frac{\omega}{c}$ is the wave-number and ω the frequency of the incident wave), takes the following form:

Definition 1 (Vector Diffraction Problem)**.** *Given an incident electromagnetic Field* $(\boldsymbol{E}^i, \boldsymbol{H}^i)$*, find a scattered field* $(\mathbf{E}^s, \mathbf{H}^s)$ *satisfying Maxwell's equations* (1.2) *throughout* $\mathbb{R}^3 \backslash \Omega$ *(here* Ω *is the scattering body, whose surface* $\partial_\Omega = \Gamma_c$ *is perfectly conducting with a normal* $\mathbf{n}$

defined on any point) also satisfying the boundary condition

$$\mathbf{n} \times (\mathbf{E}^i + \mathbf{E}^s) = 0, \quad \text{on } \Gamma_c, \tag{1.3}$$

as well as the Silver-Müller radiation condition at infinity

$$\lim_{|\mathbf{r}|\to\infty} (\mathbf{H}^s \times \mathbf{r} - |\mathbf{r}|E^s) = 0. \tag{1.4}$$

Though the 'aetheric' constructions underlying the original derivations of Maxwell's equations have been long abandoned, the equations themselves continue to provide a very robust model of electromagnetic wave propagation in low- and high-frequency regimes alike; only at scales which involve relativistic and/or quantum adjustments do the equations fail to describe real-world phenomena.

In some regimes (notably high-frequency nonpolarized light [6], or in the two-dimensional case), the electromagnetic vector boundary value problem can be reduced to a simpler formulation which involves only scalar quantities, and the Helmholtz equation for time-harmonic scalar wave-propagation given by

$$\Delta u + k^2 u = 0. \tag{1.5}$$

Scalar boundary value problems involving the Helmholtz equation play a significant role in other domains of physics and engineering (unrelated to electromagnetic and light propagation models), especially in the field of acoustics, where the study of the interaction of sound waves with objects of various shapes plays a critical role in applications such as sonar design and detection, noninvasive sonography, etc. The scalar time-harmonic counterpart to the vector problem characterized by 1 takes the form

Definition 2 (Scalar Diffraction Problems)**.** *Given an incident wave u^i satisfying (1.5) in space, find a solution u^s to (1.5) in $\mathbb{R}^3\backslash\Omega$, satisfying either:*

$$u^s_{|\Gamma_c} = -u^i_{|\Gamma_c}, \ \textit{Dirichlet Problem} \tag{1.6}$$

or

$$\frac{\partial u^s}{\partial \mathbf{n}}|_{\Gamma_c} = -\frac{\partial u^i}{\partial \boldsymbol{n}}|_{\Gamma_c}, \ \textit{Neumann Problem}, \tag{1.7}$$

and the Sommerfeld radiation condition at infinity

$$\lim_{r\to\infty} r\big(\frac{\partial u^s}{\partial r} - iku^s\big) = 0. \tag{1.8}$$

If the total field $u^t = u^s + u^i$ is understood as a pressure wave, then the Dirichlet Problem imposes that the pressure vanish at the boundary of the object, which models the behavior of a perfectly soft obstacle. The Neumann Problem on the other hand, by imposing that the normal velocity of the underlying fluid be zero at the boundary, is a good model for perfectly hard objects.

Solving the acoustic problem of Definition 2 in the case where the closed surface Γ^c is replaced by an *open* surface Γ is the main purpose of this thesis: given that neither the scalar nor the electromagnetic open-surface problems had previously been satisfactorily solved, tackling the scalar problem is an important and reasonable first step. It should also be pointed out that in the case of the diffraction by open arcs in two-dimensional space, the electromagnetic scattering problem can be reduced to a combination of the scalar Dirichlet and Neumann problems, by decomposing the incoming waves in terms of TE and TM polarization. In the two-dimensional case, therefore, solution of the full vector electromagnetic problem follows from the corresponding solution in the scalar case.

We continue our historical overview with an emphasis on the scalar wave problems that form the focus of the present thesis.

1.2.4 Classical methods: separation of variables, Kirchhoff and Fraunhofer integrals

As pointed out in [6, 38], there are very few scattering geometries with enough symmetry for an exact solution to the boundary value problem given in Definition 2 (and Definition 1) to be derived analytically; when such a solution can be produced however, it is usually in terms of summations of special functions obtained by separation of variables. The canonical disc scattering problem, for example, can be solved in the orthogonal oblate spheroidal coordinate system (see Figure 1.4), and closed-form solutions to the scalar and electromagnetic boundary value problems have been obtained in terms of oblate spheroidal functions of the first, second and third kind [10, 19, 20]. These spheroidal solutions however can only be used numerically for fairly small discs, since the series involved in their calculation become

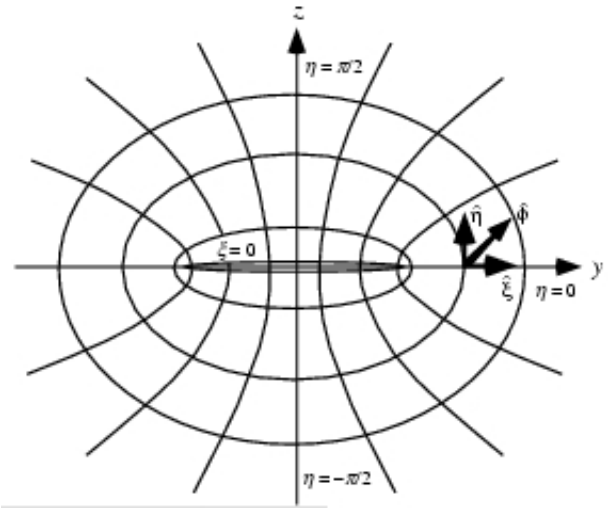

Figure 1.4: Oblate coordinate system. ($x = \sqrt{1+\xi^2}\sqrt{1-\eta^2}\cos\phi$, $y = \sqrt{1+\xi^2}\sqrt{1-\eta^2}\sin\phi$, $z = \xi\eta$). The disc is defined by $\xi = 0$.

increasingly difficult to sum accurately as the frequency of the problem increases.

In the absence of general analytic solutions, and prior to the recent development of modern computational techniques, many methods have been developed over the last century to produce approximations to the solutions of the scalar and electromagnetic scattering problems of Definitions 1 and 2.

At the heart of most approximations is the use of Green's formula, which for solutions to Helhmoltz' equation (1.5) satisfying the radiation condition (1.8), provides a rigorous generalization of Fresnel's original assumption (1.1) that the field at one point can be expressed as an integral along the surface of the product of some unknown density function and a source field located at the integration point. The formula is stated below, its proof can be found in any textbook on scattering and wave propagation problems [24, 51].

Theorem 1 (Green's formula)**.** *For any compact closed region* Ω *with a smooth, closed boundary* $\partial\Omega$*, let* u *be a smooth radiating solution of* (1.5) *outside* Ω*, and* $\mathbf{r}$ *be any point outside* Ω*. Then,*

$$u(\mathbf{r}) = \int_{\partial_\Omega} \left\{ u(\mathbf{r}') \frac{\partial G_k(\mathbf{r}, \mathbf{r}')}{\partial \boldsymbol{n}_{\mathbf{r}'}} - \frac{\partial u(\mathbf{r}')}{\partial \boldsymbol{n}_{\mathbf{r}'}} G_k(\mathbf{r}, \mathbf{r}') \right\} dS'. \tag{1.9}$$

Here $G_k(\mathbf{r}, \mathbf{r}')$ is the free-space Green's function defined by

$$G_k(\mathbf{r}, \mathbf{r}') = \begin{cases} \frac{e^{ik|\mathbf{r}-\mathbf{r}'|}}{4\pi|\mathbf{r}-\mathbf{r}'|}, & k \geq 0, \quad \text{three-dimensional space} \\ -\frac{1}{2\pi}\log|\mathbf{r}-\mathbf{r}'| & k = 0, \quad \text{two-dimensional space} \\ \frac{i}{4}H_0^1(|\mathbf{r}-\mathbf{r}'|) & k > 0, \quad \text{two-dimensional space.} \end{cases} \tag{1.10}$$

Clearly, equation (1.9) does not in itself provide an explicit expression for the solution u^s of the Dirichlet problem on the surface $\partial\Omega$, since $\frac{\partial u^s}{\partial \mathbf{n}}$ is unknown along the surface. Similarly for the Neumann problem, the value of u^s along the surface is unknown.

An approximation that can be derived from Green's theorem is known by the name of the Fresnel-Kirchhoff integral, which applies to the case of an infinite flat screen punctured by an aperture $\mathcal{A}$ and illuminated by a point source lying at $\mathbf{r}_0$, on one side of the screen. Kirchhoff's approximation consists of assuming that 1) k is large with respect to the size of $\mathcal{A}$; that 2) The total field and its normal derivative along the screen is null, and that 3) The total field is continuous along the aperture $\mathcal{A}$. It follows from applying (1.9) to a closed volume which extends $\mathcal{A}$ to a region behind the screen (see [6]), that the total field can be reduced for any point $\mathbf{r}$ behind the screen to the Fresnel-Kirhchoff integral

$$u^t(\mathbf{r}) = -\frac{i|\mathcal{A}|}{2\lambda}\int_{\mathcal{A}} \frac{e^{ik(|\mathbf{r}-\mathbf{r}'|+|\mathbf{r}_0-\mathbf{r}'|)}}{|\mathbf{r}-\mathbf{r}'||\mathbf{r}_0-\mathbf{r}'|}\left(\cos(\mathbf{n}_{\mathbf{r}'}, \mathbf{r}_0-\mathbf{r}') - \cos(\mathbf{n}_{\mathbf{r}'}, \mathbf{r}-\mathbf{r}')\right) dS'. \tag{1.11}$$

Here, $|\mathcal{A}|$ denotes the area of the aperture , $\lambda = \frac{2\pi}{k}$ is the wavelength, and $\mathbf{n}_{\mathbf{r}'}$ denotes the normal with respect to the aperture at the point $\mathbf{r}'$. After further approximations (under notably, paraxial assumptions that the angle δ between $\mathbf{r}-\mathbf{r}_0$ and the normal $\mathbf{n}$ remains small), the solution of the scalar problem can be reduced further [6, 35] to the familiar Fraunhofer integral:

$$u^t(\mathbf{r}) \sim -\frac{i|\mathcal{A}|}{\lambda}\frac{\cos\delta}{|\mathbf{r}||\mathbf{r}_0|}\int_{\mathcal{A}} e^{ik(|\mathbf{r}-\mathbf{r}'|+|\mathbf{r}_0-\mathbf{r}'|)} dS'. \tag{1.12}$$

This integral expression is probably the best known approximate solution to diffraction problems, and provides very satisfactory results for a number of applications; it remains limited however to a high-frequency, paraxial far-field setup and in particular, it cannot be used to evaluate near-field aperture diffraction solutions.

1.2.5 Geometrical theory of diffraction

In the time-period spanning the introduction of Kirchhoff's integrals and the development of modern numerical solutions, almost a century elapsed during which various heuristic corrections to the geometrical theory of optics and the Kirchhoff approximations were proposed in an effort to obtain simple, yet more accurate formulas to evaluate diffracted fields. One of the most successful examples of extensions is provided by Keller's geometrical theory of diffraction, first introduced in 1953 [34, 38]. Keller's approach rested on the postulate that along with the usual rays of geometrical optics, there exist *diffracted rays* which account for the phenomenon of diffraction. These rays originate at edges, corners and stationary points; Keller's theory describes how to evaluate the contribution of each ray in term of diffraction coefficients which can be calculated locally as a function of the incidence wave, the geometry, and other properties of the scatterer. Even though essentially heuristic, the theory has proven relatively accurate over time, even at wavelengths of roughly the size of the scatterer [10]; it provided scientists in the 1960s and 1970s with a general tool for dealing with objects that could not be treated via a simple separation of variables. The method does not handle more complex phenomena such as foci, caustics, shadow boundaries and other transition regions well; while increasingly complex refinements have been proposed since then, those remain limited in their overall generality [10]. However, the insights gained from Keller's theory are valuable in many ways and, in particular, as an element of rigorous and convergent solvers for high-frequency problems [15].

1.3 Modern Theoretical and Numerical Methods: Closed-Surface Case

1.3.1 Boundary integral equations: preliminaries

The boundary integral approach to diffraction problems relies on the original intuition behind Fresnel's integral that the scattered wave should be expressible solely in terms of an unknown density along the surface. Simply generalizing the expression (1.1) by allowing for other kernel functions $K(\mathbf{r}, \mathbf{r}')$ in the integral, and replacing the diffraction coefficient χ by an unknown density φ, the integral equation method consists in seeking solutions in the

form of potentials

$$h(\mathbf{r}) = \int_{\Gamma_c} K(\mathbf{r}, \mathbf{r}')\varphi(\mathbf{r}')dS', \quad \mathbf{r} \text{ outside } \Gamma_c, \tag{1.13}$$

where $\Gamma_c = \partial\Omega$ is the (closed) boundary of the domain Ω introduced in Definition 2. Provided that for any $\mathbf{r}' \in \Gamma$, $K(\mathbf{r}, \mathbf{r}')$ is a radiative solution of the Helmholtz equation (as a function of $\mathbf{r}$), then clearly, so is the potential $h(\mathbf{r})$; in particular, $h(\mathbf{r})$ thus provides a solution to the scalar problem if and only if it satisfies the boundary conditions along Γ_c, that is, if and only if the density φ satisfies the integral equation resulting from taking the limiting values of (1.13) (or its normal derivative) as $\mathbf{r}$ approaches the surface Γ_c.

One of the early proposals for use of integral equations as a general alternative to the traditional separation of variable techniques can be found in Maue's seminal 1949 paper [45]. Making use of Green's formula, Maue showed that the solution to the Dirichlet and Neumann scalar problems could naturally be expressed as double- and single-layer potentials respectively,

$$u(\mathbf{r}) = \int_{\Gamma_c} \frac{\partial G_k(\mathbf{r}, \mathbf{r}')}{\partial \mathbf{n}_{\mathbf{r}'}} \varphi(\mathbf{r}')dS', \quad v(\mathbf{r}) = \int_{\Gamma_c} G_k(\mathbf{r}, \mathbf{r}')\psi(\mathbf{r}')dS' \tag{1.14}$$

where $G_k(\mathbf{r}, \mathbf{r}')$ is the free-space Green's function given in equation (1.10). In particular, Maue established that the solutions φ and ψ must satisfy the second-kind integral equations of the form

$$\frac{\varphi}{2} + \mathbf{D}_c[\varphi] = -u^i_{|\Gamma_c}, \quad -\frac{\psi}{2} + \mathbf{D}_c^*[\psi] = -\frac{\partial u^i}{\partial \mathbf{n}}|_{\Gamma_c} \tag{1.15}$$

respectively, where the double-layer operator $\mathbf{D}_c$ and its adjoint $\mathbf{D}_c^*$ are defined as

$$\mathbf{D}_c^*[\varphi](\mathbf{r}) = \int_{\Gamma_c} \frac{\partial G_k(\mathbf{r}, \mathbf{r}')}{\partial \mathbf{n}_r} \varphi(\mathbf{r}')dS', \quad \mathbf{D}_c[\psi](\mathbf{r}) = \int_{\Gamma_c} \frac{\partial G_k(\mathbf{r}, \mathbf{r}')}{\partial \mathbf{n}_{r'}} \varphi(\mathbf{r}')dS'. \tag{1.16}$$

As pointed out by Maue, one immediate advantage inherent in equations (1.15) is that the original volumetric partial differential equation boundary-value problem has been reduced to the determination of the values of a surface density: the dimensionality has thus been reduced by one, and the values to be found limited to a bounded domain. In particular, as soon as densities φ or ψ have been determined which solve (1.15), the solution to the original scalar problem is fully known and easily evaluated anywhere in $\mathbb{R}^3\backslash\Omega$ by means of the potential representation (1.14).

While general in nature, Maue's paper did not pose the questions of uniqueness or

solvability of equations (1.15); as is now well known, these equations do not in fact possess a unique solution for all choices of the wave number k [24, 51]. Nor did Maue's paper address the numerical challenges associated with the solution of these equations for general surfaces; rather, in a statement reflecting the limited computational capabilities of the time, the paper opens explicitly with the (retrospectively amusing) disclaimer that "considerations of practical usability must be put aside for now"[3].

1.3.2 Existence, uniqueness and regularity of solutions for closed Lipschitz surfaces

1.3.2.1 General results

It was not until the 1980s that existence and uniqueness results for the scalar problem of Definition 2 were fully established for the general case of a Lipschitz surface (a surface which is continuous, but allowed to have corners and edges); as inferred in [26], there are unique solutions in the space $H^1_{loc}(\mathbb{R}^3\backslash\Omega)$ to the scalar Neumann and Dirichlet boundary problems, provided the incident wave u^i admits boundary values on the surface which are in the space $H^{\frac{1}{2}}(\Gamma_c)$. The spaces $H^1_{loc}(\mathbb{R}^3\backslash\Omega)$ and $H^{\frac{1}{2}}(\Gamma_c)$ are defined, for example, in [51], and provide for a complete variational framework for the scalar problem of Definition 2. These general results built upon decades of fundamental research on singular-integral operators, pioneered by the works of Calderòn, Zygmund, Meyer, Mikhlin and others, and rely in particular on the study of the integral operators $\mathbf{D}_c$, $\mathbf{D}_c^*$ introduced above in equation (1.16) as well as the single-layer and hypersingular operators denoted by $\mathbf{S}_c$ and $\mathbf{N}_c$, respectively, which arise as the boundary values and normal derivatives of the single-layer and double-layer potentials defined in equation (1.14):

$$\mathbf{S}_c[\varphi](\mathbf{r}) = \int_{\Gamma_c} G_k(\mathbf{r},\mathbf{r}')\varphi(\mathbf{r}')dS', \quad \mathbf{r}\in\Gamma_c \tag{1.17}$$

$$\mathbf{N}_c[\psi](\mathbf{r}) = \int_{\Gamma_c} \frac{\partial^2 G_k(\mathbf{r},\mathbf{r}')}{\partial_{\mathbf{n}_\mathbf{r}}\partial_{\mathbf{n}'_\mathbf{r}}}\varphi(\mathbf{r}')dS', \quad \mathbf{r}\in\Gamma_c. \tag{1.18}$$

$\mathbf{N}_c$ is said to be a hypersingular operator, since it is defined by a nonintegrable kernel via a generalization of the concept of Cauchy principal value integral. We note, for fu-

[3]Original text: Bei der Allgemeinheit des betrachteten Beugunsgproblems erscheint es wünschenswert, die vorliegenden Zusammenhänge auch von einem anderen als dem üblichen Standpunkte aus zu überblicken, *auch wenn man die Frage der Nützlichkeit für praktische Rechnungen zunächst offenlässt.*

ture reference, that the various operators mentioned above define the following bounded mappings [26]:

$$\mathbf{S}_c : H^{-\frac{1}{2}}(\Gamma_c) \to H^{\frac{1}{2}}(\Gamma_c), \tag{1.19}$$

$$\mathbf{D}_c : H^{\frac{1}{2}}(\Gamma_c) \to H^{\frac{1}{2}}(\Gamma_c), \tag{1.20}$$

$$\mathbf{D}_c^* : H^{\frac{1}{2}}(\Gamma_c) \to H^{\frac{1}{2}}(\Gamma_c), \tag{1.21}$$

$$\mathbf{N}_c : H^{\frac{1}{2}}(\Gamma_c) \to H^{-\frac{1}{2}}(\Gamma_c). \tag{1.22}$$

Notice that while the most general existence and uniqueness results were only established in the mid-1980s, complete proofs of existence, uniqueness and regularity in the context of Hölder and $C^{1,\alpha}$ continuous functions had been established much earlier (see, e.g., [24] and references therein), already providing a solid framework for the pursuit of robust numerical algorithms. The results in [26] provided the additional generality to establish convergence of Galerkin-based approaches for the most general Lipschitz setup.

1.3.2.2 Additional regularity results

In the case where the surface is smooth (instead of merely Lipschitz), more can be said about the regularity of the solutions than mere existence in the space $H^1_{loc}(\mathbb{R}^3\backslash\Omega)$; in particular, introducing the family of Sobolev spaces $H^s(\Gamma_c)$ $(s > -\frac{1}{2})$ (see eg [51]) it can be shown that the four operators introduced so far define bounded (continuous) mappings

$$\mathbf{S}_c : H^s(\Gamma_c) \to H^{s+1}(\Gamma_c), \tag{1.23}$$

$$\mathbf{D}_c : H^s(\Gamma_c) \to H^s(\Gamma_c), \tag{1.24}$$

$$\mathbf{D}_c^* : H^s(\Gamma_c) \to H^s(\Gamma_c), \tag{1.25}$$

$$\mathbf{N}_c : H^{S+1}(\Gamma_c) \to H^s(\Gamma_c). \tag{1.26}$$

These mapping results are important in that they allow for precise quantification, if the surface is smooth, of the regularity of the solution[4] of the integral equations under consideration, in terms of the regularity of the right-hand side. In particular, *for closed* infinitely smooth surfaces, if the incident wave is infinitely smooth, then the solutions to the boundary-integral equations are infinitely smooth as well.

Finally, we mention here that the operators $\mathbf{S}_c$, $\mathbf{D}_c^*$ and $\mathbf{D}_c$ define compact operators from $H^s(\Gamma_c)$ into $H^s(\Gamma_c)$; in particular, their spectrum is discrete and accumulates at zero, which has important implications for numerical applications.

1.3.2.3 Second-kind equations and well-posedness

Depending on the representation chosen for the solutions u and v to the Dirichlet and Neumann problems in terms of single-layer and double-layer potentials, different integral equations are obtained on the surface, which involve the operators introduced above. However, while bounded, the operators $\mathbf{S}_c$, $\mathbf{N}_c$, $\mathbf{D}_c^*$ and $\mathbf{D}_c$ are not always invertible: as shown, for example, in [24, 51], for every closed surface Γ_c there exists a discrete set of values for the wave number k (associated with resonances of the interior problem) for which the mappings (1.23) through (1.26) are not bijective. In particular, the early equations (1.15) derived by Maue are not invertible for some frequencies.

Fortunately, a variety of combinations of the single- and double-layer potentials can be constructed to produce potential representations of the form (1.13) whose boundary values result in boundary integral operators which are invertible at all frequencies. We cite the potential introduced by Brakhage and Werner [11] as a good example: seeking a solution to the Dirichlet problem in Definition 2 of the form

$$u(\mathbf{r}) = \int_{\Gamma_c} \left\{ i\alpha G_k(\mathbf{r}, \mathbf{r}') - \frac{\partial G_k(\mathbf{r}, \mathbf{r}')}{\partial_{\mathbf{n_r}}} \right\} \varphi(\mathbf{r}') dS', \tag{1.27}$$

gives rise to the boundary integral equation

$$i\alpha \mathbf{S}_c[\varphi] + \frac{\varphi}{2} - \mathbf{D}_c^*[\varphi] = -u^i_{|\Gamma}, \tag{1.28}$$

[4]We recall here that the spaces $H^s(\Gamma_c)$ contain functions of a certain degree of smoothness, which is enforced through imposition of square integrability of the Fourier transform of its derivatives up to the order s. In particular a function belonging to $H^s(\Gamma_c)$ for $s > 1 + k$ has at least k continuous surface derivatives on Γ_c (see, e.g., [48, p. 198 and p. 203]).

which can be shown, if α is real, to be uniquely invertible at all frequencies. Equation (1.28) is also a second-kind Fredholm integral equation [5], since the operators $\mathbf{S}_c$ and $\mathbf{D}_c^*$ define compact mappings from $H^s(\Gamma_c)$ into Γ_c. In particular, it follows that the spectrum associated with the operator is discrete, bounded, and accumulates around $-\frac{1}{2}$. Numerically therefore, provided that the equation can be discretized in an efficient manner, the resulting discretized linear system is well posed and, if solved, for instance, using iterative Krylov subspace linear algebra solvers, requires a small number of iterations to converge to a solution.

The quest for the most practical potential representations for the solution of the Dirichlet and Neumann problems has given rise to interesting work in the last few decades, starting with the determination of the optimal parameter α to be used in practice should one be using the potential (1.28). A recent discussion can be found in [14], which provides well-conditioned equations for the acoustic Neumann problem. We note for future reference that the choices of potentials for the Neumann problem usually make use in one form or another of the Calderón formulae [24, 51]:

$$\mathbf{N}_c\mathbf{S}_c = -\frac{I}{4} + (\mathbf{D}_c^*)^2\,, \tag{1.29}$$

$$\mathbf{S}_c\mathbf{N}_c = -\frac{I}{4} + (\mathbf{D}_c)^2\,, \tag{1.30}$$

which establishes that the combination of the operator $\mathbf{N}_c$ and $\mathbf{S}_c$ gives rise to bounded, second-kind Fredholm operator from $H^s(\Gamma_c)$ into $H^s(\Gamma_c)$. Interestingly, use of the sole Calderón formula as a means of preconditioning the Dirichlet and Neumann problems was reported in [22], even though the combination itself suffers from the same invertibility issues around resonant frequencies than the operators $\mathbf{S}_c$ and $\mathbf{N}_c$ alone.

1.3.3 Numerical methods for closed-surface problems

Numerical methods for the resolution of scattering problems can broadly be grouped into two categories: volumetric PDE discretizations and boundary integral discretization; these are, in turn, reviewed (briefly) in the following two sections.

[5] It involves an integral operator of the form $I + T_K$, T_K compact.

1.3.3.1 Volumetric PDE discretizations

Volumetric discretizations seek to solve the corresponding boundary value problems by discretizing a region of space around the scattering body, and imposing a radiation condition across the outer boundary of the computational domain(see, e.g., [63]). The resulting linear systems (obtained by considering finite difference schemes of the Helmholtz operator) are sparse, but depending on the frequency and the size of the computational domain, a very large number of unknowns may be required. Volumetric methods based on finite-differences or finite elements tend to suffer from well-known pollution/dispersion effects [3, 36].

1.3.3.2 Boundary integral methods

The Boundary Finite Element Methods (Galerkin discretization of boundary integral equations) proceeds by introducing discrete subspaces V_h of $H^{\frac{1}{2}}(\Gamma_c)$ associated with a certain mesh-size h, and basis functions (the elements) defined on V_h. The projection of the variational formulation of the boundary integral equation, results in a linear system for the coefficients of the solution in the basis associated with a given subspace V_h. Many choices of bases (elements) can be defined, as well as integration techniques. The literature on this topic is extremely rich, we refer to [23, 30, 50] for an overview. The Galerkin BEM has the advantage of being directly applicable on standard triangular meshes that are often available in industrial applications.

1.3.3.3 High-order integral solvers

An alternative to the Galerkin Boundary Element Methods is given by the Nyström formulations [25, 39]. Recent fast, high-order Nyström formulation for three-dimensional problems [13, 14, 17] have enabled accurate solution in short computing times for scattering problems involving three-dimensional scatterers hundreds of wavelengths in size. Since the methodology presented in this thesis relates to this approach, we refer the reader to Chapter 4 for a full description in these regards. Here we merely mention that the new fast, high-order Nyström methods proceed by seeking values of the unknown density φ at points distributed on overlapping patches that describe the given scattering surface Γ_c, without use of triangulations, on the basis of fast and high-order quadrature rules, to accurately evaluate the action of the various operators on the density φ at a given set of collocation

points. Such rules thus provide a means for evaluation of the action of the operator on a given density function, and by application of iterative Krylov subspace linear algebra techniques to these maps, accurate solutions can then be obtained in a small number of iterations, where each iteration requires a single evaluation of the forward map.

1.4 The Open-Surface Problem

In what follows, and for the rest of this thesis, Γ designates a smooth open surface with a smooth boundary (respectively an open arc) in three dimensional space (respectively in two-dimensional space). Throughout this work we consider the sound-soft and sound-hard problems of acoustic scattering by the open screen Γ, that is, the Dirichlet and Neumann boundary value problems

$$\begin{cases} \Delta u + k^2 u = 0 \quad \text{outside} \quad \Gamma, \quad u|_\Gamma = f, & \text{(sound-soft)}, \\ \Delta v + k^2 v = 0 \quad \text{outside} \quad \Gamma, \quad \frac{\partial v}{\partial n}|_\Gamma = g, & \text{(sound-hard)}, \end{cases} \tag{1.31}$$

for the Helmholtz equation, where u and v satisfy the radiation condition (1.8) at infinity[6].

1.4.1 Existence and uniqueness of solutions

The first complete proof of existence and uniqueness of solutions to the open-surface problems (1.31) was provided by Stephan in [59] for the three-dimensional case, nearly at the same time as the general results [26] on general Lipschitz surfaces were put forth by Costabel. Existence and uniqueness proofs for open-surface scattering in the two-dimensional case where also provided in [60, 61]. As shown in all three contributions [59–61], the open-surface Dirichlet and Neumann problems admit, in close analogy with the results for closed surfaces of [26], unique solutions in $H^1_{loc}(\mathbb{R}^3 \setminus \Gamma)$ (or $H^1_{loc}(\mathbb{R}^2 \setminus \Gamma)$ for two-dimensional problems), which can be expressed in terms of single-layer and double-layer potentials, respectively:

$$u(\mathbf{r}) = \int_\Gamma G_k(\mathbf{r}, \mathbf{r}')\mu(\mathbf{r}')dS' \tag{1.32}$$

[6] In the two-dimensional case [25], this condition needs to be replaced by $\lim_{r\to\infty} \sqrt{r}\left(\frac{\partial u}{\partial r} - iku\right) = 0, \quad r = |\mathbf{r}|$.

and

$$v(\mathbf{r}) = \int_\Gamma \frac{\partial G_k(\mathbf{r},\mathbf{r}')}{\partial \mathbf{n}'_\mathbf{r}} \nu(\mathbf{r}')dS', \tag{1.33}$$

for $\mathbf{r}$ outside Γ. Here G_k denotes the free-space Green's function (1.10), and $\mathbf{n}_{\mathbf{r}'}$ is a unit vector normal to Γ at the point $\mathbf{r}' \in \Gamma$ (we assume, as we may, that $\mathbf{n}_{\mathbf{r}'}$ is a smooth function of $\mathbf{r}' \in \Gamma$). Letting $\mathbf{S}$ and $\mathbf{N}$ denote the classical single-layer and hypersingular operators

$$\mathbf{S}[\mu](\mathbf{r}) \equiv \int_\Gamma G_k(\mathbf{r},\mathbf{r}')\mu(\mathbf{r})dS', \qquad \mathbf{r} \text{ on } \Gamma \tag{1.34}$$

and

$$\mathbf{N}[\nu](\mathbf{r}) \equiv \lim_{z\to 0} \frac{\partial}{\partial \mathbf{n}_\mathbf{r}} \int_\Gamma \frac{\partial G_k(\mathbf{r},\mathbf{r}'+z\mathbf{n}_{\mathbf{r}'})}{\partial \mathbf{n}'_\mathbf{r}} \nu(\mathbf{r}')dS', \qquad \mathbf{r} \text{ on } \Gamma \tag{1.35}$$

the densities μ and ν are the unique solutions of the integral equations

$$\mathbf{S}[\mu] = f \quad \text{and} \tag{1.36}$$

$$\mathbf{N}[\nu] = g. \tag{1.37}$$

As further shown in [33, 59, 61, 65], the operators $\mathbf{S}$ and $\mathbf{N}$ define bounded and continuously invertible mappings

$$\mathbf{S}: \ \tilde{H}^{-\frac{1}{2}}(\Gamma) \to H^{\frac{1}{2}}(\Gamma), \quad \text{and} \tag{1.38}$$

$$\mathbf{N}: \ \tilde{H}^{\frac{1}{2}}(\Gamma) \to H^{-\frac{1}{2}}(\Gamma), \tag{1.39}$$

where for $s \in \mathbb{R}$, the space $\tilde{H}^s(\Gamma)$ is defined below.

Definition 3. *Let G_1 be a domain in space (or the plane for the two-dimensional problem), with a smooth boundary $\dot{G}_1$, let $s \in \mathbb{R}$, and assume $\dot{G}_1$ contains the smooth open curve Γ. The Sobolev space $\tilde{H}^s(\Gamma)$ is defined as the set of all elements $f \in H^s(\dot{G}_1)$ satisfying* $\text{supp}(f) \subseteq \overline{\Gamma}$.

Interestingly thus, the problem of noninvertibility around certain frequencies associated with resonances inside a closed surface disappears in the context of an open surface: $\mathbf{S}$ and $\mathbf{N}$ are invertible at all frequencies.

While the results mentioned above establish uniqueness of solutions in the same generality as for the closed-surface case discussed in Section 1.3.2.1, two difficulties inherent to screen problems must be highlighted at this point:

- In view of singular behavior at the edge, the open-surface mapping results (1.38) and (1.39), which bear close resemblance to their corresponding close-surface counterparts (1.19) and (1.22), cannot be directly extended to higher-order Sobolev spaces, even in the case of a smooth surface and a smooth boundary, in sharp contrast with the closed-surface properties (1.23) and (1.26). Section 2.5.2 provides a striking illustration: a constant function across Γ_c gets mapped via $\mathbf{S}$ to a function whose first derivative has a nonintegrable singularity at the edge. (However, as we will establish in Chapter 2, this situation can be corrected, and full regularity mappings recovered after appropriate introduction of modified weighted integral operators).

- The equations (1.36) and (1.37) are first-kind integral equations, and may thus result in large number of Krylov subspace iterations if the methods of Section 1.3.3 are used to solve the problem.

The next two paragraphs provide more details on these difficulties.

1.4.2 Singularity at the edge

It was known as early as 1896 that solutions of diffraction problems might develop singularities in a neighborhood of the edge: Sommerfeld's exact solution [57] for electromagnetic scattering by a half-plane contains the singular term $\sqrt{y}$ (where $y = 0$ denotes the edge of the half-plane), the derivative of which tends to infinity as $y \to 0$. Still, the question as to whether the solution to open-surface problems could present singularities was a subject of debate for quite some time, into the late 1940s and 1950s.[7] Most notably, we highlight the corrections [8, 9] to early contributions by Bethe and Meixner [4, 46], and the well-known finite-energy condition introduced in [47]. Interestingly, Maue had also considered open

[7] The theoretical difficulties associated with the presence of edge singularities is perhaps best illustrated by the anecdotal discussion by Bouwkamp in [7] which mentions a contradiction in Sommerfeld's results [57] in these regards. Bouwkamp writes:

> *A few sentences written by Sommerfeld in his original paper... do not seem to be in agreement with the fact that actually singularities occur in his final mathematical result: "Weiter werden wir verlangen dass der Lichtvector überall endlich sei, ausser in dem leuchtendem Punkt", and on the account of the experimental fact that the diffraction edge seems to radiate as a fine line.... "Das ist natürlich eine optische Täuschung. Im Wahrheit gibt es im Windungspunkte keine Unendlichkeitsstelle... Der Auge sollte die analytische Fortsetzung... von der exacten Formel bilden". We have seen, however, that the exact formula does show a singularity at the edge of the screen!*

[In summary, Sommerfeld's German text above states that the field must be finite everywhere, and that the eye's interpretation of the existence of point sources along the edge of a diffraction screen observed from the shadow is an optical illusion, and that the eye should trust the formulae and not what it sees.]

surfaces in his 1949 contribution [45], and established to some extent that the solutions to the integral equations (1.36) and (1.37) must present a square-root singularity in the neighborhood of the edge. This square-root asymptotic behavior was eventually confirmed rigorously by the work of Stephan [59], where it was established that the solutions μ and ν to equations (1.36) and (1.37) can be expressed in the forms

$$\mu = \frac{\chi_1}{\sqrt{d}} + \zeta_1, \tag{1.40}$$

$$\nu = \chi_2\sqrt{d} + \zeta_2, \tag{1.41}$$

where χ_1 and χ_2 are smooth cut-off functions, ζ_1 and ζ_2 belong to $H^{\frac{1}{2}}(\Gamma)$ and $H^{\frac{3}{2}}(\Gamma)$, respectively, and d denotes the euclidean the distance to the edge. Interestingly, Stephan's doctoral thesis [58] pushed the analysis further, establishing that α and β could be expressed in terms of an additional power of $d^{\frac{1}{2}}$:

$$\mu = \frac{\chi_1}{\sqrt{d}} + \chi_3\sqrt{d} + \zeta_3, \tag{1.42}$$

$$\nu = \chi_2\sqrt{d} + \chi_4 d^{\frac{3}{2}} + \zeta_4 \tag{1.43}$$

where ζ_3 belongs to $H^{\frac{3}{2}}$ and ζ_4 belongs to $H^{\frac{5}{2}}$.

While the above expressions establish the first- and second-order singularity of the solutions, in view of the very general work by Grisvard [29], additional terms involving logarithmic singularities could in principle be present in the solutions; it wasn't until the recent work of [42] that the logarithmic terms were shown to *not* arise in the open-surface scattering solutions. What is more, the results of [42] establish that, as long as the degree of the surface and of the right-hand side in (1.31) allow it, the solutions μ and ν can be expressed in terms of a power series in $\sqrt{d}$ and a smoother residual (thus extending the results (1.42) and (1.43) beyond the first two terms). It follows in particular, that for any smooth open surface, the solutions to (1.36) and (1.37) can be expressed fully as

$$\mu = \frac{\alpha}{\sqrt{d}}, \tag{1.44}$$

$$\nu = \beta\sqrt{d}, \tag{1.45}$$

where α and β are infinitely differentiable functions throughout Γ, *up to and including the endpoints*. Thus the singular nature of these solutions is fully characterized by the factors $d^{1/2}$ and $d^{-1/2}$ in equations (1.44) and (1.45).

Remark 1. *The results in [42, 59] establish uniqueness, existence and regularity of solutions to the open-surface problem without requiring the explicit use of Meixner's 'edge-condition'. Rather the uniqueness and correctness of the solution from the physics standpoint (satisfaction of Meixner's integrability condition) is ensured by the fact that the solutions are elements of the Sobolev space* $H^1_{loc}(\mathbb{R}^3 \setminus \Gamma)$.

1.4.3 First-kind integral equations

As discussed in Section 1.3.2.3, second-kind Fredholm equations are obtained for closed surfaces by either 1) making use of the classical jump relations of the double-layer potential and the normal derivative of the single-layer potential [25] across the scattering surface, or 2) by relying on the Calderón formulae (1.29) and (1.30).

In the case of an open surface however, the requirement (1.31) that the same limit be achieved on both sides of the surface prevents the use of discontinuous potentials. And, use of the Calderón formula (1.29) does not give rise to a Fredholm equation in the function spaces associated with open-screen problems: for example, the composition of $\mathbf{N}$ and $\mathbf{S}$ is not even defined in the functional framework set forth in [59]—since, as demonstrated in Section 2.5.2, the image of the operator $\mathbf{S}$ (the Sobolev space $H^{\frac{1}{2}}(\Gamma)$) is larger than the domain of definition of $\mathbf{N}$ (the Sobolev space $\tilde{H}^{\frac{1}{2}}(\Gamma)$). It is interesting to note, further, that, as shown in Section 2.5.4, in the two-dimensional case, the image of a constant function has a strong edge singularity,

$$\mathbf{NS}[1](\mathbf{r}) = O(\frac{1}{d(\mathbf{r})}), \tag{1.46}$$

where $d(\mathbf{r})$ denotes the distance to the edge—which demonstrates the degenerate character of the composite operator $\mathbf{NS}$.

1.4.4 Previous work

Significant effort has been devoted to the treatment of the various difficulties arising in connection with open-surface scattering problems. The contributions [22, 53] sought to generalize the Calderón relations in the open-surface context, as a means to derive second-

kind Fredholm equations for these problems. In [53], it is shown that the combination **NS** can be expressed in the form $\mathbf{I}+\mathbf{T}_K$, where the kernel $\mathbf{K}(x,y)$ of the operator $\mathbf{T}_K$ has a *polar* singularity of the type $O\left(\frac{1}{|x-y|}\right)$. This result is not uniform throughout the surface, and it does not take into account the singular edge behavior: the resulting operator $\mathbf{T}_K$ is not compact (in fact it gives rise to strong singularities at the surface edge, see (1.46)), and the operator $\mathbf{I}+\mathbf{T}_K$ is therefore not a second-kind operator in any meaningful functional space. When used in conjunction with boundary elements that vanish on the edges, however, the combination **NS** does gives rise to reduction of iteration numbers, at least for low-frequency problems, as demonstrated in reference [22] through low-frequency numerical examples. This contribution does not include details on accuracy, and it does not utilize integral weights to resolve the solution's edge singularity. A related but different method was introduced in [1] which exhibits, once again, small iteration numbers at low frequencies, but which does not resolve the singular edge behavior and for which no accuracy studies have been presented.

An effective approach for regularization of the singular edge behavior in the two-dimensional open-arc problem is based on use of a cosine change of variables; The approach [2], some aspects of which are incorporated in our contribution, treats the Dirichlet problem for Laplace's equation by means of second-kind equations; the basis of this approach lies in the observation that the cosine basis has the dual positive effect of diagonalizing the logarithmic potential for a straight arc and removing the singular edge behavior; thus, its inverse can be easily computed and can be used as a preconditioner to produce a second-kind operator for a general arc. The approach [49], which also uses a cosine basis, treats the Neumann problem for the nonzero frequency Helmholtz equation with spectral accuracy by means of first-kind equations. The contribution [37], finally, treats, just like [2], the Laplace problem by means of second-kind equations resulting from inversion of the straight-arc logarithmic potential; like [49], further, it produces spectral accuracy through use of the cosine transforms. The second-kind integral approach developed in [2] and later revisited in [37] seems essentially limited to the specific problem for which it was proposed: neither an extension to the Neumann Problem nor to the full three-dimensional problem seem straightforward. And, more importantly, this approach does not lead to adequately preconditioned equations for nonzero frequencies: a simple experiment conducted in Section 3.2 shows in fact that it requires significantly *more* linear algebra iterations, as k increases, than are necessary if

the operator $\mathbf{S}_\omega$ alone is used.

Finally, in the three-dimensional case, high-order integration rules for the single-layer and hypersingular operators were introduced in [31, 32, 62], but these methods have only been applied to problems of low frequency, and they have not been used in conjunction with iterative solvers.

1.5 Content and Layout of the Thesis

In the remainder of this thesis, we present a new framework for the treatment of the open-surface problems defined by (1.31). Our framework, which is laid-out fully in Chapter 2, aims at combining both, the smoothness results of equations (1.44)–(1.45) with the original suggestion put forth in [53] that, even for open surfaces, the combination of $\mathbf{N}$ and $\mathbf{S}$ ought to lead, in some way, to second-kind integral equations. We achieve this by introducing a weight ω with square-root singularity at the edge in the operators, thus leading to the definition of a new set of *weighted* operators $\mathbf{S}_\omega$ and $\mathbf{N}_\omega$, as well as the combination $\mathbf{N}_\omega\mathbf{S}_\omega$. Through this framework, as we establish in Chapter 2 for the two-dimensional case, a picture emerges for the open-surface case which resembles closely the one found for closed-surface configurations:

- the new operators enjoy regularity results akin to equations (1.23) and (1.26), across an entire family of periodized Sobolev spaces $H^s_e(2\pi), \quad s > 0$.
- the combination $\mathbf{N}_\omega\mathbf{S}_\omega$ gives rise to a generalized Calderón formula; in particular, it is a second-kind integral operator.

We show in Chapters 3 and 4 that the enhanced regularity properties can be exploited to construct high-order quadrature rules for the discretization of the operators $\mathbf{N}_\omega$ and $\mathbf{S}_\omega$. The construction of those rules in the three-dimensional case is not a trivial task since the presence of the weight essentially requires any quadrature rule to resolve two singularities at once, namely the Green's function singularity and the edge singularity. Resolving both singularities efficiently and to high-order on a general surface becomes particularly delicate in the presence of principal-value surface integrals, such as those arising in the operator $\mathbf{N}_\omega$. The quadrature rules presented in Chapter 4 achieve this, and thus give rise, for the first time, to a fast and efficient high-order solver for three-dimensional problems, whose

performance is analogous to that previously achieved by the closed-surface solvers [13, 14, 17]. A high-order solver for the corresponding two-dimensional problems is presented in Chapter 3. As demonstrated throughout Chapters 3 and 4, our solvers enable evaluation of highly accurate solutions for a variety of geometries and wide ranges of frequencies, including, for the first time, accurate high-frequency solutions to such classical 19th-century problems as the (scalar) diffraction by a disc, a circular aperture, and the two-hole Young experiment.

Chapter 2

Generalized Calderón Formula for Open-Arcs

In this chapter, we introduce a novel set of weighted integral operators for the resolution of the scalar open-surface problems (1.31), and we establish that, in the two-dimensional case, the new operators can be combined to give rise to a second-kind integral operator, thus generalizing the closed-surface Calderón formula (1.29); we further establish regularity results which pave the way to the construction of the high-order quadrature rules which will are presented in Chapter 3.

From here on and throughout this chapter, Γ denotes a smooth open-arc in the two-dimensional plane.

2.1 Weighted Operators and Generalized Calderón Formula

In view of equations (1.44) and (1.45), for any nonvanishing function $\omega(\mathbf{r}) > 0$ such that

$$\omega \sim d^{1/2}, \quad \text{(by which it is meant that } \omega/\sqrt{d} \text{ is } C^\infty \text{ up to the endpoints of } \Gamma), \tag{2.1}$$

we define the weighted operators

$$\mathbf{S}_\omega[\alpha] = \mathbf{S}\left[\frac{\alpha}{\omega}\right] \tag{2.2}$$

and

$$\mathbf{N}_\omega[\beta] = \mathbf{N}\left[\beta \cdot \omega\right], \tag{2.3}$$

and we consider the weighted versions

$$\mathbf{S}_\omega[\alpha] = f \tag{2.4}$$

and

$$\mathbf{N}_\omega[\beta] = g \tag{2.5}$$

of the integral equations (1.36) and (1.37); clearly, in view of the discussion of Section 1.4.2, for smooth Γ and smooth right-hand sides f and g, the solutions α and β of (2.4) and (2.5) are smooth up to the endpoints of Γ.

Without loss of generality we use a smooth parameterization $\mathbf{r}(t) = (x(t), y(t))$ of Γ defined in the interval $[-1, 1]$, for which $\tau(t) = |\frac{d\mathbf{r}(t)}{dt}|$ is never zero. For definiteness and simplicity, throughout the rest of this chapter we select ω, as we may, in such a way that

$$\omega(\mathbf{r}(t)) = \sqrt{1 - t^2}. \tag{2.6}$$

The operators $\mathbf{S}_\omega$ and $\mathbf{N}_\omega$ thus induce the parameter-space operators

$$S_\omega[\varphi](t) = \int_{-1}^{1} G_k\left(\mathbf{r}(t), \mathbf{r}(t')\right) \frac{\varphi(t')}{\sqrt{1 - t'^2}}\, \tau(t')dt', \tag{2.7}$$

and

$$N_\omega[\psi](t) = \lim_{z \to 0^+} \frac{\partial}{\partial z} \int_{-1}^{1} \frac{\partial}{\partial \mathbf{n}_{\mathbf{r}(t')}} G_k\left(\mathbf{r}(t) + z\mathbf{n}_{\mathbf{r}(t)}, \mathbf{r}(t')\right) \psi(t')\tau(t')\sqrt{1 - t'^2}dt'; \tag{2.8}$$

defined on functions φ and ψ of the variable t, $-1 \le t \le 1$; clearly, for $\varphi(t) = \alpha(\mathbf{r}(t))$ and $\psi(t) = \beta(\mathbf{r}(t))$ we have

$$\mathbf{S}_\omega[\alpha](\mathbf{r}(t)) = S_\omega[\varphi](t) \tag{2.9}$$

and

$$\mathbf{N}_\omega[\beta](\mathbf{r}(t)) = N_\omega[\psi](t). \tag{2.10}$$

In order to proceed we further transform our integral operators: using the changes of variables $t = \cos\theta$ and $t' = \cos\theta'$ and, defining $\mathbf{n}_\theta = \mathbf{n}_{\mathbf{r}(\cos\theta)}$ and using (2.9) and (2.10), we

re-express equations (2.4) and (2.5) in the forms

$$\tilde{S}[\tilde{\varphi}] = \tilde{f} \tag{2.11}$$

and

$$\tilde{N}[\tilde{\psi}] = \tilde{g}, \tag{2.12}$$

where $\tilde{S}$ and $\tilde{N}$ denote the operators

$$\tilde{S}[\gamma](\theta) = \int_0^\pi G_k(\mathbf{r}(\cos\theta), \mathbf{r}(\cos\theta'))\gamma(\theta')\tau(\cos\theta')d\theta' \tag{2.13}$$

and

$$\tilde{N}[\gamma](\theta) = \lim_{z\to 0^+} \frac{\partial}{\partial z} \int_0^\pi \frac{\partial}{\partial \mathbf{n}_{\theta'}} G_k(\mathbf{r}(\cos\theta) + z\mathbf{n}_\theta, \mathbf{r}(\cos\theta'))\gamma(\theta')\tau(\cos\theta')\sin^2\theta' d\theta', \tag{2.14}$$

and where

$$\tilde{f}(\theta) = f(\mathbf{r}(\cos\theta)) \quad , \quad \tilde{g}(\theta) = g(\mathbf{r}(\cos\theta)); \tag{2.15}$$

clearly, the solutions of equations (2.7)-(2.12) are related by

$$\tilde{\varphi}(\theta) = \varphi(\cos\theta) \quad , \quad \tilde{\psi}(\theta) = \psi(\cos\theta). \tag{2.16}$$

In view of the symmetries induced by the $\cos\theta$ dependence in equations (2.13) through (2.15), it is natural to study the properties of these operators and equations in appropriate Sobolev spaces $H_e^s(2\pi)$ of 2π periodic and even functions defined below; cf. [16, 66].

Definition 4. *Let $s \in \mathbb{R}$. The Sobolev space $H_e^s(2\pi)$ is defined as the completion of the space of infinitely differentiable 2π-periodic and even functions with respect to the norm*

$$\|v\|_s^2 = |a_0|^2 + 2\sum_{m=1}^{\infty} m^{2s}|a_m|^2, \tag{2.17}$$

where a_m denotes the m-th cosine coefficient of v:

$$v(\theta) = \frac{1}{2}a_0 + \sum_{m=1}^{\infty} a_m \cos(m\theta). \tag{2.18}$$

Clearly the set $\{\cos(n\theta) : n \in \mathbb{N}\}$ is a basis of the Hilbert space $H_e^s(2\pi)$ for all s.

We are now ready to state the theorem at the heart of this chapter. Here and throughout this text an operator L between two Hilbert spaces is said to be bicontinuous if and only if L is invertible and both L and L^{-1} are continuous operators.

Theorem 2. *The composition $\tilde{N}\tilde{S}$ defines a bicontinuous operator from $H_e^s(2\pi)$ to $H_e^s(2\pi)$ for all $s > 0$. Further, this operator satisfies a generalized Calderón formula*

$$\tilde{N}\tilde{S} = \tilde{J}_0^\tau + \tilde{K}, \tag{2.19}$$

where $\tilde{K} : H_e^s(2\pi) \to H_e^s(2\pi)$ is a compact operator, and where $\tilde{J}_0^\tau : H_e^s(2\pi) \to H_e^s(2\pi)$ is a bicontinuous operator, independent of k, with point spectrum equal to the union of the discrete set $\Lambda_\infty = \{\lambda_0 = -\frac{\ln 2}{4}, \quad \lambda_n = -\frac{1}{4} - \frac{1}{4n} : n > 0\}$ and a certain open set set Λ_s which is bounded away from zero and infinity. The sets Λ_s are nested, they form a decreasing sequence, and they satisfy $\bigcap_{s>0} \bar{\Lambda}_s = \{-\frac{1}{4}\}$, where $\bar{\Lambda}_s$ denotes the closure of Λ_s. In addition, the operators

$$\tilde{S} : \ H_e^s(2\pi) \to H_e^{s+1}(2\pi) \quad \textit{and} \tag{2.20}$$

$$\tilde{N} : \ H_e^{s+1}(2\pi) \to H_e^s(2\pi) \tag{2.21}$$

are bicontinuous.

It follows that the open-arc TE and TM scattering problems (1.31) can be solved by means of the second-kind integral equations

$$\tilde{N}\tilde{S}[\tilde{\varphi}] = \tilde{N}[\tilde{f}] \quad \text{and} \tag{2.22}$$

$$\tilde{N}\tilde{S}[\tilde{\psi}] = \tilde{g}, \tag{2.23}$$

respectively. The smooth and periodic solutions $\tilde{\varphi}$ and $\tilde{\psi}$ of these equations are related to the singular solutions μ and ν of equations (1.36) and (1.37) via

$$\mu\left(\mathbf{r}(\cos\theta)\right) = \tilde{\varphi}(\theta)/\sin\theta \tag{2.24}$$

$$\nu\left(\mathbf{r}(\cos\theta)\right) = \sin\theta \tilde{S}[\tilde{\psi}](\theta). \tag{2.25}$$

We thus see that, through introduction of the weight ω and use of spaces of even and

2π periodic functions, a picture emerges for the open-surface case that resembles closely the one found for closed-surface configurations: the generalized Calderón relation (2.19) is analogous to the Calderón formula (1.29), and mapping properties in terms of the complete range of Sobolev spaces are recovered for $\tilde{S}$ and $\tilde{N}$, in a close analogy to the framework embodied by equations (1.23) and (1.26).

We note, for future reference, that in a nonperiodized formulation, equations (2.22)–(2.23) take the form

$$\mathbf{N}_\omega \mathbf{S}_\omega[\varphi] = \mathbf{N}_\omega[f], \tag{2.26}$$

$$\mathbf{N}_\omega \mathbf{S}_\omega[\psi] = g, \tag{2.27}$$

where the solutions φ and ψ relate to the solutions of (1.36) and (1.37) via the relations

$$\mu = \frac{\varphi}{\omega}, \quad \nu = \omega \cdot \mathbf{S}_\omega[\psi]. \tag{2.28}$$

In the remainder of this chapter we present a proof of Theorem 2. This proof is based on a number of elements, the first one of which, introduced in Section 2.2, concerns the operator $\tilde{J}_0^\tau$ in (2.19)—which corresponds, in fact, to the zero-frequency/straight-arc version of Theorem 2.

2.2 Straight Arc at Zero Frequency: Operators $\tilde{J}_0$ and $\tilde{J}_0^\tau$

2.2.1 Boundedness of $\tilde{J}_0$ and link with the Cesàro operator

In the case in which Γ is the straight-arc $[-1, 1]$ and $k = 0$, $\tilde{S}$ reduces to Symm's operator [16, 66]

$$\tilde{S}_0[\tilde{\varphi}](\theta) = -\frac{1}{2\pi} \int_0^\pi \ln|\cos\theta - \cos\theta'| \tilde{\varphi}(\theta) d\theta, \tag{2.29}$$

whose diagonal property

$$\tilde{S}_0[e_n] = \lambda_n e_n, \ \lambda_n = \begin{cases} \frac{\ln 2}{2} & n = 0 \\ \frac{1}{2n}, & n \geq 1 \end{cases} \tag{2.30}$$

in the cosine basis $\{e_n : n \geq 0\}$ of $H_e^s(2\pi)$ ($e_n(\theta) = \cos n\theta$) is well documented [44].

Remark 2. *Equation* (2.30) *shows that* $\tilde{S}_0$ *is a bounded and continuously invertible operator*

from $H_e^s(2\pi)$ to $H_e^{s+1}(2\pi)$ for all real values of s.

The corresponding zero-frequency straight-arc version $\tilde{N}_0$ of the operator $\tilde{N}$, in turn, is given by

$$\tilde{N}_0[\tilde{\psi}](\theta) = \frac{1}{4\pi} \lim_{z\to 0} \frac{\partial^2}{\partial z^2} \int_0^\pi \ln|(\cos\theta - \cos\theta')^2 + z^2|\tilde{\psi}(\theta')\sin^2\theta' d\theta'. \tag{2.31}$$

Following [24, 39, 49], we express $\tilde{N}_0$ in the form

$$\tilde{N}_0 = \tilde{D}_0 \tilde{S}_0 \tilde{T}_0 \tag{2.32}$$

where

$$\tilde{D}_0[\tilde{\varphi}](\theta) = \frac{1}{\sin\theta} \frac{d\tilde{\varphi}(\theta)}{d\theta} \tag{2.33}$$

and

$$\tilde{T}_0[\tilde{\varphi}](\theta) = \frac{d}{d\theta} \left(\tilde{\varphi}(\theta)\sin\theta\right); \tag{2.34}$$

for the sake of completeness, a derivation of the general curved-arc arbitrary-frequency version of this relation is provided in Appendix 2.5.1.

Note that, in contrast with the closed-arc case [39, p. 117], the expressions (2.32) through (2.34) contain the vanishing factor $\sin\theta$ and the singular factor $1/\sin\theta$; in particular, it is not immediately clear that the operator $\tilde{N}_0$ maps $H_e^{s+1}(2\pi)$ into $H_e^s(2\pi)$. To establish this fact, and, further, to initiate our general study of the composite operator $\tilde{N}\tilde{S}$, we start by establishing the following result for the straight-arc zero-frequency version

$$\tilde{J}_0 = \tilde{N}_0 \tilde{S}_0 \tag{2.35}$$

of the operator $\tilde{N}\tilde{S}$.

Lemma 1. *The composition $\tilde{J}_0 = \tilde{N}_0\tilde{S}_0$ defines a bounded operator from $H_e^s(2\pi)$ into $H_e^s(2\pi)$ for all $s > 0$.*

Proof. We first evaluate the action of $\tilde{J}_0$ on the basis $\{e_n : n \geq 0\}$. The case $n = 0$ is straightforward: in view of (2.30) and (2.32) we have

$$\tilde{J}_0[e_0](\theta) = -\frac{\ln 2}{4}. \tag{2.36}$$

For $n \geq 0$, in turn, expanding (2.34) we obtain

$$\begin{aligned} \tilde{T}_0[e_n](\theta) &= \cos\theta\cos n\theta - n\sin n\theta\sin\theta \\ &= \frac{\cos(n+1)\theta + \cos(n-1)\theta}{2} + n\frac{\cos(n+1)\theta - \cos(n-1)\theta}{2} \end{aligned} \tag{2.37}$$

which, for $n \geq 2$, in view of (2.30) yields, upon application of $\tilde{S}_0$,

$$\tilde{S}_0\tilde{T}_0[e_n](\theta) = \frac{\cos(n+1)\theta}{4(n+1)} + \frac{\cos(n-1)\theta}{4(n-1)} + n\left(\frac{\cos(n+1)\theta}{4(n+1)} - \frac{\cos(n-1)\theta}{4(n-1)}\right) \quad , \quad (n \geq 2) \tag{2.38}$$

and, in view of (2.32)-(2.33),

$$\tilde{N}_0[e_n](\theta) = -\cos\theta\frac{\sin n\theta}{2\sin\theta} - \frac{n}{2}\cos n\theta, \quad n \geq 2, \tag{2.39}$$

which can easily be verified to also hold for $n = 1$. Using (2.30) and (2.36) we thus obtain

$$\tilde{J}_0[e_n](\theta) = \begin{cases} -\frac{\ln 2}{4}, & n = 0 \\ -\cos\theta\frac{\sin n\theta}{4n\sin\theta} - \frac{\cos n\theta}{4}, & n > 0 \end{cases} \tag{2.40}$$

and, therefore,

$$\tilde{J}_0[\tilde{\varphi}](\theta) = -\frac{\tilde{\varphi}(\theta)}{4} - \frac{\cos\theta}{4}\tilde{C}[\tilde{\varphi}](\theta) + \frac{1-\ln 2}{4\pi}\int_0^\pi \tilde{\varphi}(\theta)d\theta, \tag{2.41}$$

where the operator $\tilde{C}$ is defined by

$$\tilde{C}[e_n](\theta) = \begin{cases} 0 & \text{for } n = 0 \\ \frac{\sin n\theta}{n\sin\theta} & \text{for } n > 0, \end{cases} \tag{2.42}$$

and where the last term in equation (2.41) is obtained by collecting the zero-th-order terms, and explicitly expressing the zero-th- order coefficient of $\tilde{\varphi}$ as an integral.

It is not difficult to verify the integral expression

$$\tilde{C}[\tilde{\varphi}](\theta) = \frac{\theta(\pi-\theta)}{\pi\sin\theta}\left[\frac{1}{\theta}\int_0^\theta \tilde{\varphi}(u)du - \frac{1}{\pi-\theta}\int_\theta^\pi \tilde{\varphi}(y)du\right] \tag{2.43}$$

for $\tilde{C}$ which, in turn, can be expressed in terms of the Césaro operator

$$C[f](x) = \frac{1}{x}\int_0^x f(u)du = \int_0^1 f(xu)du. \tag{2.44}$$

As is known [12], C is a bounded operator from $L^2[0,b]$ into $L^2[0,b]$ (the space of square-integrable functions over $[0,b]$) for all $b > 0$. Further, for all $f \in C_0^\infty[0,b]$, all $m \in \mathbb{N}$, $m \geq 1$ and all $x \in [0,b]$ we have

$$\left|\frac{\partial^m C[f](x)}{\partial x^m}\right|^2 \leq \left(\int_0^1 \left|u^m f^{(m)}(xu)\right| du\right)^2 \leq \left(\int_0^1 \left|f^{(m)}(xu)\right| du\right)^2 = \left(C\left[g\right](x)\right)^2 \tag{2.45}$$

where, letting $g = \left|f^{(m)}\right|$, the first inequality follows from equation (2.44). Integrating this inequality with respect to x and taking into account the boundedness of the operator C in L^2 we obtain in particular

$$\int_0^{2\pi} \left|\frac{\partial^m C[f](x)}{\partial x^m}\right|^2 dx \leq M||f^{(m)}||^2_{L_2[0,2\pi]} \tag{2.46}$$

for some constant M. It follows easily from this inequality that $\tilde{C}$ is a continuous operator from $H_e^m(2\pi)$ into $H_e^m(2\pi)$ for all nonnegative integers m. Letting $H^m(2\pi)$ be the space of 2π periodic functions whose derivatives of order k are square integrable in any bounded set of the line for all integers $k \leq m$ (c.f. [39]) we see that $\tilde{C}$ equals the restriction of some continuous operator $\tilde{P} : H^m(2\pi) \to H^m(2\pi)$: simply define $\tilde{P}$ to equal $\tilde{C}$ on the subspace of even functions, and to equal 0 on the space of odd functions. In view of the Sobolev interpolation result (see, e.g., [39, Theorem 8.13]), $\tilde{P}$ defines a continuous operator from $H^s(2\pi)$ to $H^s(2\pi)$ for all $s \geq 0$, and thus, by restriction,

$$\tilde{C} \quad \text{maps continuously} \quad H_e^s(2\pi) \to H_e^s(2\pi) \quad \text{for all} \quad s > 0. \tag{2.47}$$

The proof is completed by noting that the last term in the decomposition (2.41) defines a continuous and compact operator from $H_e^s(2\pi)$ into itself. □

Remark 3. *The decomposition* (2.41) *resembles superficially the classical closed-surface Calderón formula* (1.29)*, as it expresses the composition* $\tilde{J}_0 = \tilde{N}_0\tilde{S}_0$ *as the sum of* $-I/4$ *and an additional operator. As shown in Section 2.2(2.2.3), however, the operator* $\tilde{C} : H_e^s(2\pi) \to H_e^s(2\pi)$ *which appears in* (2.41) *is not compact—and thus, formula* (2.41) *fails to*

enable treatment of the operator $\tilde{J}_0$ by means of the Fredholm theory. In Sections 2.2(2.2.2) through 2.2(2.2.4), however, we do show that the operator $\tilde{J}_0 = \tilde{N}_0\tilde{S}_0$ is bicontinuous, and, further, we provide a description of its spectrum: the eigenvalues of $\tilde{J}_0$ are tightly clustered around $-\frac{1}{4}$, in close analogy with the clustering implied by the identity term $-\frac{I}{4}$ in the Calderón formula (1.29).

This observation is not limited to the flat-arc zero-frequency case: in Section 2.4 we further show that a certain operator $\tilde{J}_0^{\tau}$ which is closely related to $\tilde{J}_0$ (and which shares its point spectrum) can be used as a substitute of the identity operator I in a generalization, valid for open surfaces, of the classical Calderón formula.

2.2.2 Invertibility of $\tilde{J}_0$

We proceed to show that the continuous operator $\tilde{J}_0$ admits an inverse which is also bounded from $H_e^s(2\pi)$ into $H_e^s(2\pi)$. Since the decomposition (2.32) is not directly invertible on a term-by-term basis ($\tilde{T}_0$ and $\tilde{D}_0$ are not invertible), we first give an explicit form of the inverse $\tilde{J}_0^{-1}$.

Lemma 2. *The operator $\tilde{J}_0 : H_e^s(2\pi) \to H_e^s(2\pi)$ which, according to equations* (2.32) *and* (2.35) *is given by*

$$\tilde{J}_0 = \tilde{D}_0\tilde{S}_0\tilde{T}_0\tilde{S}_0, \tag{2.48}$$

is bijective, with inverse

$$\tilde{J}_0^{-1} = -4\tilde{S}_0^{-1}\tilde{C}\tilde{S}_0\tilde{T}_0. \tag{2.49}$$

Proof. Since the rightmost factor $\tilde{S}_0$ in equation (2.48) is a diagonal operator, we consider the next operator from the right in this product, namely, $\tilde{T}_0$. In view of (2.34) and (2.42) we clearly have the useful identity

$$\tilde{T}_0\tilde{C}[e_n] = \begin{cases} 0, & n = 0 \\ e_n, & n > 0. \end{cases} \tag{2.50}$$

A corresponding identity for the composition $\tilde{C}\tilde{T}_0$ follows from equation (2.43); in this case we obtain

$$\tilde{C}\tilde{T}_0 = I. \tag{2.51}$$

Having obtained a partial inverse for the factor $\tilde{T}_0$ in (2.48) and since the next factor

$\tilde{S}_0$ from the right is, once again, a diagonal operator, we consider now the leftmost factor in equation (2.48): the operator $\tilde{D}_0$. In view of (2.33) we have

$$\tilde{D}_0[e_n](\theta) = \begin{cases} 0, & n = 0 \\ -n\frac{\sin n\theta}{\sin\theta}, & n \geq 1. \end{cases} \tag{2.52}$$

Clearly, this operator bears a simple relationship with the operator $\tilde{C}$ that gives the partial inverse of $\tilde{T}_0$: in view of (2.30) and (2.42) we have

$$\tilde{D}_0 = -\frac{1}{4}\tilde{C}\left(\tilde{S}_0^{-1}\right)^2. \tag{2.53}$$

In sum, to obtain the inverse of $\tilde{J}_0$ we proceed as follows: multiplying $\tilde{J}_0$ on the right by $\tilde{S}_0^{-1}\tilde{C}$ we obtain an operator that maps e_0 to 0 and e_n to $\tilde{D}_0\tilde{S}_0[e_n]$. Thus, considering (2.51) and (2.53), we further multiply on the right by $-4\tilde{S}_0\tilde{T}_0$ and we obtain the operator

$$-4\tilde{J}_0\tilde{S}_0^{-1}\tilde{C}\tilde{S}_0\tilde{T}_0 \tag{2.54}$$

which, in view of the fact that the image of $\tilde{S}_0\tilde{T}_0$ is orthogonal to e_0 (as it follows easily from equations (2.30) and (2.37)) maps e_n to $-4\tilde{D}_0\left(\tilde{S}_0\right)^2\tilde{T}_0[e_n]$ for all $n \geq 0$. But, in view of (2.53), this quantity equals $\tilde{C}\tilde{T}_0[e_n]$ which, according to (2.51), equals e_n. In other words, the operator (2.54) maps e_n to e_n for $n = 0, 1, 2\ldots$—and, thus,

$$\tilde{I}_0 = -4\tilde{S}_0^{-1}\tilde{C}\tilde{S}_0\tilde{T}_0 \tag{2.55}$$

is a right inverse of $\tilde{J}_0$.

Conversely, since in view of equations (2.48) and (2.53) $\tilde{J}_0$ can be expressed in the form

$$\tilde{J}_0 = -\frac{1}{4}\tilde{C}\tilde{S}_0^{-1}\tilde{T}_0\tilde{S}_0, \tag{2.56}$$

we have

$$\tilde{I}_0\tilde{J}_0 = \tilde{S}_0^{-1}\tilde{C}\tilde{S}_0\tilde{T}_0\tilde{C}\tilde{S}_0^{-1}\tilde{T}_0\tilde{S}_0. \tag{2.57}$$

As noted above, the image of $\tilde{T}_0$ is orthogonal to e_0, and thus, since $\tilde{S}_0$ is a diagonal operator, the same is true of the operator $\tilde{S}_0^{-1}\tilde{T}_0\tilde{S}_0$. Equation (2.50) can therefore be used

directly to obtain

$$\tilde{T}_0\tilde{C}\tilde{S}_0^{-1}\tilde{T}_0\tilde{S}_0[e_n] = \tilde{S}_0^{-1}\tilde{T}_0\tilde{S}_0[e_n], \quad \text{for all} \quad n \geq 0. \tag{2.58}$$

Clearly then, equation (2.57) can be reduced to

$$\tilde{I}_0\tilde{J}_0 = \tilde{S}_0^{-1}\tilde{C}\tilde{T}_0\tilde{S}_0, \tag{2.59}$$

and making use of (2.51), we finally obtain

$$\tilde{I}_0\tilde{J}_0 = I, \tag{2.60}$$

as desired. The proof is now complete. □

Lemma 3. *For all $s > 0$, the inverse $\tilde{J}_0^{-1}$ is a bounded mapping from $H_e^s(2\pi)$ into $H_e^s(2\pi)$.*

Proof. In view of equations (2.29), (2.37), (2.38) and (2.42) we obtain

$$\tilde{C}\tilde{S}_0\tilde{T}_0[e_n](\theta) = \begin{cases} \frac{1}{2}, & n = 0 \\ \frac{\cos\theta}{4}, & n = 1 \\ \frac{\sin(n+1)\theta}{4(n+1)^2\sin\theta} + \frac{\sin(n-1)\theta}{4(n-1)^2\sin\theta} + n\left(\frac{\sin(n+1)\theta}{4(n+1)^2\sin\theta} - \frac{\sin(n-1)\theta}{4(n-1)^2\sin\theta}\right), & n \geq 2, \end{cases} \tag{2.61}$$

which we re-express as

$$\tilde{C}\tilde{S}_0\tilde{T}_0[e_n] = \tilde{F}[e_n] + \tilde{G}[e_n], \tag{2.62}$$

where

$$\tilde{F}[e_n] = \begin{cases} \frac{1}{2}, & n = 0 \\ \frac{1}{4}\,e_1, & n = 1 \\ \tilde{C}\tilde{S}_0[\frac{e_{n+1}+e_{n-1}}{2}], & n \geq 2, \end{cases} \tag{2.63}$$

and where $\tilde{G} = \tilde{C}\tilde{S}_0\tilde{T}_0 - \tilde{F}$, or, expanding the sine terms in equation (2.61),

$$\tilde{G}[e_n](\theta) = \frac{1}{4}\begin{cases} 0, & n = 0, 1 \\ n\cos n\theta\left(\frac{1}{(n+1)^2} + \frac{1}{(n-1)^2}\right) + n\frac{\sin n\theta}{\sin\theta}\cos\theta\left(\frac{1}{(n+1)^2} - \frac{1}{(n-1)^2}\right), & n \geq 2. \end{cases} \tag{2.64}$$

Using (2.42), the linear operator $\tilde{G}$ can be re-expressed in the form

$$\tilde{G}[e_n](\theta) = \tilde{R}_0[e_n](\theta) + \cos\theta \tilde{C}\left[\tilde{R}_1[e_n]\right](\theta), \quad n \geq 2 \tag{2.65}$$

where the diagonal operators $\tilde{R}_0$ and $\tilde{R}_1$ are defined by

$$\tilde{R}_0[e_n] = \frac{1}{4}\left(\frac{n}{(n+1)^2} + \frac{n}{(n-1)^2}\right) e_n, \quad n \geq 2 \tag{2.66}$$

and

$$\tilde{R}_1[e_n] = \frac{-n^3}{(n+1)^2(n-1)^2} e_n, \quad n \geq 2, \tag{2.67}$$

respectively. Clearly both $\tilde{R}_0$ and $\tilde{R}_1$ are bounded operators from $H_e^s(2\pi)$ to $H_e^{s+1}(2\pi)$, and, thus, in view of (2.47) and (2.65), so is $\tilde{G}$. Invoking once again equation (2.47) we see from (2.63) that $\tilde{F}$ is a bounded operator from $H_e^s(2\pi)$ into $H_e^{s+1}(2\pi)$, and in view of (2.62), the same holds for the operator $\tilde{C}\tilde{S}_0\tilde{T}_0$. It follows from (2.49) and (2.30) that $\tilde{J}_0^{-1}$ is a bounded operator from $H_e^s(2\pi)$ into $H_e^s(2\pi)$, as claimed. □

Corollary 1. *For all $s > 0$, the operator $\tilde{N}_0$ defines a bicontinuous mapping from $H_e^{s+1}(2\pi)$ to $H_e^s(2\pi)$.*

Proof. This follows directly from Remark 2, equation (2.35), and Lemmas 1, 2 and 3. □

2.2.3 Point spectrum of $\tilde{J}_0$

Having established boundedness and invertibility, we conclude our study of the operator $\tilde{J}_0$ by computing its eigenvalues.

Lemma 4. *For any $s > 0$, the point spectrum σ_s of $\tilde{J}_0 : H_e^s(2\pi) \to H_e^s(2\pi)$ can be expressed as the union*

$$\sigma_s = \Lambda_s \cup \Lambda_\infty, \tag{2.68}$$

where Λ_∞ is the discrete set

$$\Lambda_\infty = \{\lambda_n : n = 0, 1, \ldots, \infty\}, \ \lambda_n = \begin{cases} -\frac{\ln 2}{4}, & n = 0 \\ -\frac{1}{4} - \frac{1}{4n}, & n > 0, \end{cases} \tag{2.69}$$

and where Λ_s is the open bounded set

$$\Lambda_s = \left\{ \lambda = (\lambda_x + i\lambda_y) \in \mathbb{C} \ : \ 4s + 2 < \frac{-\left(\lambda_x + \frac{1}{4}\right)}{(\lambda_x + \frac{1}{4})^2 + \lambda_y^2} \right\}. \tag{2.70}$$

Proof. We start by re-expressing equation (2.40) as

$$\tilde{J}_0[e_n](\theta) = \begin{cases} -\frac{\ln 2}{4} & n = 0 \\ -\frac{\sin(n+1)\theta}{4n\sin\theta} + \frac{\cos n\theta}{4n} - \frac{\cos n\theta}{4}, & n > 0. \end{cases} \tag{2.71}$$

Then, making use the well-known expansion

$$\frac{\sin(n+1)\theta}{\sin\theta} = \begin{cases} \sum\limits_{k=0}^{p} (2 - \delta_{0k}) \cos 2k\theta, & n = 2p \\ 2 \sum\limits_{k=0}^{p} \cos(2k+1)\theta, & n = 2p+1, \end{cases} \tag{2.72}$$

(which expressed in terms of Chebyshev polynomials of the first and second kind is given, e.g., in equation (40) [27, p. 187] and problem 3 in [44, p. 36]) we obtain

$$\tilde{J}_0[e_n] = \begin{cases} \lambda_n e_n - \frac{1}{2n} \sum\limits_{k=0}^{p-1} (1 - \frac{\delta_{0k}}{2}) e_{2k}, & n = 2p, \ p \geq 0 \\ \lambda_n e_n - \frac{1}{2n} \sum\limits_{k=0}^{p-1} e_{2k+1}, & n = 2p+1, \ p \geq 0 \end{cases}, \tag{2.73}$$

where the diagonal elements λ_n are defined in equation (2.69). Clearly, $\tilde{J}_0$ takes the form of an upper-triangular (infinite) matrix whose diagonal terms λ_n define eigenvalues associated with eigenvectors v_n, each one of which can be expressed in terms of a finite linear combination of the first n basis functions: $v_n = \sum_{k=0}^{n} c_k^n e_k$. In particular, for all $n \in \mathbb{N}$, $v_n \in H_e^s[0, 2\pi]$ for all $s > 0$. This shows that the set Λ_∞ of diagonal elements defined in equation (2.69) is indeed contained in σ_s for all $s > 0$.

As is well known, an upper triangular operator in an infinite-dimensional space can have eigenvalues beyond those represented by diagonal elements. As shown in [12, Th. 2], for instance, the point spectrum of the upper-triangular bounded operator

$$C^*[a](n) = \sum_{k=n}^{\infty} \frac{a_k}{k+1}, \tag{2.74}$$

(the adjoint of the discrete Cesàro operator C) is the open disc $|\lambda - 1| < 1$. As shown in

what follows, a similar situation arises for our operator $\tilde{J}_0$.

To obtain the full point-spectrum of the operator $\tilde{J}_0$ let $\lambda \in \mathbb{C}$ and $f = \sum_{k=0}^{\infty} f_n e_n$ be such that $\tilde{J}_0[f] = \lambda f$. It follows from (2.73) that the coefficients f_n satisfy the relation

$$(-\frac{1}{4} - \frac{1}{4n})f_n - \frac{1}{2}\sum_{k=1}^{\infty} \frac{f_{n+2k}}{n+2k} = \lambda f_n \quad , \quad n \geq 1, \tag{2.75}$$

along with

$$(-\frac{\ln 2}{4})f_0 - \frac{1}{4}\sum_{k=1}^{\infty} \frac{f_{2k}}{2k} = \lambda f_0 \quad , \quad n = 0. \tag{2.76}$$

Equation (2.75) is equivalent to

$$\frac{1}{2}\sum_{k=1}^{\infty} \frac{f_{n+2k}}{n+2k} = f_n(-\frac{1}{4n} - \frac{1}{4} - \lambda), \quad n \geq 1, \tag{2.77}$$

which, by subtraction, gives

$$\frac{1}{2}\frac{f_{n+2}}{n+2} = f_n(-\frac{1}{4n} - \frac{1}{4} - \lambda) - f_{n+2}(-\frac{1}{4(n+2)} - \frac{1}{4} - \lambda), \quad n \geq 1. \tag{2.78}$$

Therefore, the coefficients of f must satisfy

$$\begin{cases} f_{n+2} = & f_n\left(\frac{\frac{z}{2}+\frac{1}{n}}{\frac{z}{2}-\frac{1}{(n+2)}}\right), & n \geq 1 \\ \frac{1}{4}\sum\limits_{k=1}^{\infty} \frac{f_{2k}}{2k} = & f_0(-\frac{\ln 2}{4} - \lambda), & n = 0. \end{cases} \tag{2.79}$$

where, in order to simplify the notations, we write

$$z = 8\lambda + 2. \tag{2.80}$$

It is clear from equation (2.79) that the zero-th coefficient is determined by the coefficients of even positive orders, and that the sequence f_n for $n \geq 1$ is entirely determined by f_1 and f_2.

Clearly, there are no elements of the point-spectrum for which $Re(z) \geq 0$, since for such values of z the resulting sequence f_n is not square summable (that is, $\sum |f_n|^2 = \infty$). Note that the set of vectors $\{v_n\}$ associated with the discrete eigenvalues $\lambda_n = -\frac{1}{4} - \frac{1}{4n}$, in turn, are recovered by setting $z = -\frac{2}{n}$. To determine all of the elements of the point spectrum with $Re(z) < 0$ we study separately the odd and even terms in the sequence (2.79). We

start with the sequence $q_n = f_{2n}$, which satisfies the recurrence relationship

$$q_{n+1} = q_n \left(\frac{z + \frac{1}{n}}{z - \frac{1}{n+1}} \right), \quad n \geq 1. \tag{2.81}$$

Let $z = -x + iy$ with $x > 0$, and assume without loss of generality, that $q_1 = 1$. Then

$$q_n = \left(\frac{z-1}{z - \frac{1}{n}} \right) \prod_{k=1}^{n-1} \left(\frac{z + \frac{1}{k}}{z - \frac{1}{k}} \right), \quad n \geq 1, \tag{2.82}$$

and it follows that

$$\begin{aligned} \ln |q_n| &= \ln \left| \frac{z-1}{z - \frac{1}{n}} \right| + \frac{1}{2} \sum_{k=1}^{n-1} \ln \left(\frac{(x - \frac{1}{k})^2 + y^2}{(x + \frac{1}{k})^2 + y^2} \right) \\ &= \ln \left| \frac{z-1}{z - \frac{1}{n}} \right| + \frac{1}{2} \sum_{k=1}^{n-1} \ln \left(\frac{1 - r(x,y,k))}{1 + r(x,y,k)} \right) \end{aligned} \tag{2.83}$$

where

$$r(x,y,k) = \frac{2x}{k(x^2 + y^2 + \frac{1}{k^2})}. \tag{2.84}$$

For large k, we have

$$\ln \left(\frac{1 - r(x,y,k)}{1 + r(x,y,k)} \right) = -\frac{4x}{k(x^2+y^2)} + O(\frac{1}{k^3}), \ k \to \infty, \tag{2.85}$$

and thus

$$\ln |q_n| = -\frac{2x}{x^2+y^2} \ln n + M + O(\frac{1}{n}), \tag{2.86}$$

where M is a constant. The absolute value of q_n is thus asymptotically given by

$$|q_n| = O\left(\frac{1}{n^{\frac{2x}{x^2+y^2}}} \right) \tag{2.87}$$

as $n \to \infty$. It follows that, for any $s > 0$, the set of points (x, y) in the half-plane such that the sequence $\sum n^{2s} |q_n|^2 < \infty$ is exactly defined by the equation

$$2s - \frac{4x}{x^2+y^2} < -1. \tag{2.88}$$

The analysis for the odd-term sequence $p_n = f_{2n+1}$ can be carried out similarly, since

$$p_{n+1} = p_n \left(\frac{z + \frac{1}{n+\frac{1}{2}}}{z - \frac{1}{n+1+\frac{1}{2}}} \right), \tag{2.89}$$

which essentially amounts to replacing k by $k+\frac{1}{2}$ in equations (2.83) and (2.84). The convergence condition (2.88) thus applies to p_n as well, and it follows, in view of equation (2.80), that the set Λ_s defined by (2.70) contains all the eigenvalues of $\tilde{J}_0$ not contained in Λ_∞. □

Corollary 2. *The operator* $\tilde{C} : H_e^s(2\pi) \to H_e^s(2\pi)$ *is not compact.*

Proof. This follows from the decomposition (2.41) of $\tilde{J}_0$ and the fact that $\tilde{J}_0$ admits a spectrum that is not discrete. □

Remark 4. *Using polar coordinates* (r, θ) *around the point* $(-\frac{1}{4}, 0)$ *it is easy to check that*

$$\Lambda_s = \left\{ (\lambda_x + i\lambda_y) \in \mathbb{C} : \lambda_x + \frac{1}{4} = r\cos\theta,\ \lambda_y = r\sin\theta,\ 0 < r < -\frac{\cos\theta}{4s+2},\ \theta \in \left[\frac{\pi}{2}, \frac{3\pi}{2}\right] \right\}. \tag{2.90}$$

Clearly then, for $s > s'$, $\Lambda_s \subsetneq \Lambda_{s'}$, *and we have* $\bigcap_{s>0} \Lambda_s = \varnothing$, *while the intersection of the closures is given by* $\bigcap_{s>0} \bar{\Lambda}_s = \{-\frac{1}{4}\}$. *Also, for all* $s > 0$, $\mathrm{dist}(\sigma_s, 0) = -\frac{1}{4}$, *and* $\max_{\lambda\in\sigma_s} |\lambda| \leq \frac{3}{4}$. *It therefore follows that* σ_s *is bounded away from the zero and infinity. In view of Theorem 2 and Section 2.2.4, this is a fact of great significance in connection with the numerical solution of equations* (2.11) *and* (2.12) *by means of Krylov-subspace iterative linear-algebra techniques; see Chapter 3 for details.*

2.2.4 The operator $\tilde{J}_0^\tau$

In our proof of Theorem 2 we need to consider not $\tilde{J}_0$ but a closely related operator, namely

$$\tilde{J}_0^\tau = \tilde{N}_0^\tau \tilde{S}_0^\tau \tag{2.91}$$

where defining (in a manner consistent with equation (2.99) below) $\tilde{Z}_0[\gamma](\theta) = \gamma(\theta)\tau(\cos\theta)$, we have set

$$\tilde{S}_0^\tau[\gamma] = \tilde{S}_0 \tilde{Z}_0[\gamma], \tag{2.92}$$

and

$$\tilde{N}_0^\tau[\gamma] = \tilde{Z}_0^{-1} \tilde{N}_0[\gamma]. \tag{2.93}$$

It is easy to generalize Remark 2, Corollary 1 and Lemmas 1 through 4 to needed corresponding results for $\tilde{S}_0^\tau$, $\tilde{N}_0^\tau$ and $\tilde{J}_0^\tau$; these are given in the following Theorem.

Theorem 3. *Let $s > 0$. Then,*

(i) The operator $\tilde{S}_0^\tau \ : \ H_e^s(2\pi) \to H_e^{s+1}(2\pi)$ is bicontinuous,

(ii) The operator $\tilde{N}_0^\tau \ : \ H_e^{s+1}(2\pi) \to H_e^s(2\pi)$ is bicontinuous,

(iii) The operator $\tilde{J}_0^\tau \ : \ H_e^s(2\pi) \to H_e^s(2\pi)$ is bicontinuous,

(iv) The point spectrum of $\tilde{J}_0^\tau : \ H_e^s(2\pi) \to H_e^s(2\pi)$ is equal to the point spectrum σ_s of $\tilde{J}_0$.

Proof. In view of (2.92), (2.93), the ensuing relation

$$\tilde{J}_0^\tau = \tilde{Z}_0^{-1} \tilde{J}_0 \tilde{Z}_0, \tag{2.94}$$

and the fact that τ is smooth and nonvanishing, the proof of points *(i)*, *(ii)* and *(iii)* is immediate. Equation (2.94) also shows that (λ, v) is an eigenvalue-eigenvector pair for $\tilde{J}_0$ if and only if $(\lambda, \tilde{Z}_0^{-1}[v])$ is an eigenvalue-eigenvector pair for $\tilde{J}_0^\tau$, and point *(iv)* follows as well. □

2.3 General Properties of the Operators $\tilde{S}$ and $\tilde{N}$

The proof of Theorem 2 results from a perturbation argument involving Theorem 3 and the results established in this section on the regularity and invertibility of the operators $\tilde{S}$ and $\tilde{N}$ defined by equations (2.13) and (2.14).

2.3.1 Bicontinuity of $\tilde{S}$

We seek to show that for all $s > 0$ the operator $\tilde{S}$ defined in equation (2.13) is a bicontinuous mapping between $H_e^s(2\pi)$ into $H_e^{s+1}(2\pi)$. This is done in Lemmas 5 and 7 below.

Lemma 5. *Let $s > 0$. Then $\tilde{S}$ defines a bounded mapping from $H_e^s(2\pi)$ into $H_e^{s+1}(2\pi)$. Further, the difference $\tilde{S} - \tilde{S}_0^\tau$ (see equation (2.92)) defines a continuous mapping from $H_e^s(2\pi)$ into $H_e^{s+3}(2\pi)$.*

Proof. In view of equation (1.10) and the expression

$$H_0^1(z) = \frac{2i}{\pi} J_0(z) \ln(z) + R(z) \tag{2.95}$$

for the Hankel function in terms of the Bessel function $J_0(z)$, the logarithmic function and a certain entire function R, the kernel of the operator S_ω (equation (2.7)) can be cast in the form

$$G_k(\mathbf{r}(t), \mathbf{r}(t')) = A_1(t,t') \ln|t-t'| + A_2(t,t'), \tag{2.96}$$

where $A_1(t,t')$ and $A_2(t,t')$ are smooth functions. Further, since $J_0(z)$ is given by a series in powers of z^2, it follows that for all $m \in \mathbb{N}$, the function A_1 can be expressed in the form

$$A_1(t,t') = -\frac{1}{2\pi} + \sum_{n=2}^{m+3} a_n(t)(t'-t)^n + (t-t')^{m+4} \Lambda_{m+3}(t,t'),$$

where $\Lambda_{m+3}(t,t')$ is a smooth function of t and t'. The operator $\tilde{S}$ in equation (2.13) can thus be expressed in the form

$$\begin{aligned} \tilde{S}[\tilde{\varphi}](\theta) = \tilde{S}_0^\tau[\tilde{\varphi}](\theta) + \sum_{n=2}^{m+3} a_n(\cos\theta) \int_0^\pi (\cos\theta' - \cos\theta)^n \ln|\cos\theta - \cos\theta'| \tilde{\varphi}(\theta')\tau(\cos\theta')d\theta' \\ + \int_0^\pi A_3(\cos\theta, \cos\theta')\tilde{\varphi}(\theta')\tau(\cos\theta')d\theta', \end{aligned} \tag{2.97}$$

where $A_3(\cos\theta, \cos\theta')$, which contains a logarithmic factor, belongs to $C^{m+3}([0,2\pi] \times [0,2\pi])$.

Clearly, for $n \geq 2$, the second derivative $d^2/d\theta^2$ of the product $(\cos\theta' - \cos\theta)^n \ln|\cos\theta - \cos\theta'|$ can be expressed as a product $P_1(\cos\theta, \cos\theta') \ln|\cos\theta - \cos\theta'| + P_2(\cos\theta, \cos\theta')$ where $P_1(t,t')$ and $P_2(t,t')$ are polynomials. Collecting terms with the common factor $\cos^\ell\theta'$ we then obtain

$$\frac{d^2}{d\theta^2}\left(\tilde{S} - \tilde{S}_0^\tau\right)[\tilde{\varphi}](\theta) = \sum_{\ell=0}^{m+1} b_\ell(\cos\theta)\tilde{S}_0\tilde{Z}_\ell[\tilde{\varphi}](\theta) + \int_0^\pi A_4(\cos\theta, \cos\theta')\tilde{\varphi}(\theta')\tau(\cos\theta')d\theta', \tag{2.98}$$

where $b_\ell(\cos\theta)$ is an even smooth function, where the operator $\tilde{Z}_\ell : H_e^s(2\pi) \to H_e^s(2\pi)$

($s \in \mathbb{R}$) is given by

$$\tilde{Z}_\ell[\gamma](\theta') = \cos^\ell \theta' \; \tau(\cos\theta') \; \gamma(\theta'), \tag{2.99}$$

and where $A_4(\cos\theta, \cos\theta') \in C^{m+1}([0, 2\pi] \times [0, 2\pi])$. Now, in view of Remark 2, the first term on the right-hand side of equation (2.98) defines a bounded operator from $H_e^s(2\pi)$ into $H_e^{s+1}(2\pi)$. On the other hand, the derivatives of orders $k \leq (m+1)$ of the second term on the right-hand side of (2.98), all reduce to integral operators with bounded kernels, and thus map $L^2[0, 2\pi]$ continuously into $L^2[0, 2\pi]$. It follows that the second term itself maps continuously $H_e^0(2\pi)$ (and hence $H_e^m(2\pi)$) into $H_e^{m+1}(2\pi)$, and the lemma follows for integer values $s = m$. The extension for real values $s > 0$ follows directly by interpolation [39, Theorem 8.13]. □

The following lemma and its corollary provide a direct link between the spaces $H_e^s(2\pi)$ under consideration here, and the original space $\tilde{H}^{-\frac{1}{2}}(\Gamma)$ appearing in equations (1.38).

Lemma 6. *Let $s > 0$, and assume $\tilde{\varphi} \in H_e^s(2\pi)$. Then the function*

$$w(\xi) = \frac{1}{\pi} \int_0^\pi \tilde{\varphi}(\theta) e^{-i\xi\cos\theta} d\theta. \tag{2.100}$$

satisfies

$$\int_{\mathbb{R}} \frac{|w(\xi)|^2}{(1+|\xi|^2)^{\frac{1}{2}}} d\xi < \infty. \tag{2.101}$$

Proof. Using the $L^2[0, \pi]$-convergent cosine expansion

$$\tilde{\varphi}(\theta) = \sum_{n=0}^{\infty} a_n \cos\theta \tag{2.102}$$

we obtain

$$w(\xi) = \sum_{n=0}^{\infty} \frac{a_n}{\pi} \int_0^\pi \cos n\theta e^{-i\xi\cos\theta} d\theta. \tag{2.103}$$

Since

$$\int_0^\pi \cos n\theta e^{-i\xi\cos\theta} d\theta = \frac{1}{2}\int_{-\pi}^{\pi} e^{in\theta} e^{-i\xi\cos\theta} d\theta = \frac{1}{2} e^{\frac{in\pi}{2}} \int_{-\pi}^{\pi} e^{-in\theta} e^{-i\xi\sin\theta} d\theta = \pi i^n J_n(-\xi), \tag{2.104}$$

(where, denoting by $J_n(\xi)$ the Bessel function of order n, the last identity follows from [28,

8.411 p. 902]), we see that equation (2.103) can be re-expressed in the form

$$w(\xi) = \sum_{n=0}^{\infty} i^n a_n J_n(-\xi) = \sum_{n=0}^{\infty} \left(\sqrt{1+n^{2s}}\, i^n a_n\right) \left(\frac{J_n(-\xi)}{\sqrt{1+n^{2s}}}\right). \tag{2.105}$$

In view of the Cauchy-Schwartz inequality we thus obtain

$$|w(\xi)|^2 \leq \left(\sum_{n=0}^{\infty}(1+n^{2s})|a_n|^2\right)\left(\sum_{n=0}^{\infty}\frac{|J_n(\xi)|^2}{1+n^{2s}}\right) \leq \left(\sum_{n=1}^{\infty}\frac{|J_n(\xi)|^2}{n^{2s}} + |J_0(\xi)|^2\right)\|\tilde{\varphi}\|_s^2. \tag{2.106}$$

Since $0 \leq |\xi|/(1+|\xi|^2)^{1/2} \leq 1$, it follows that

$$\begin{aligned}\int_{\mathbb{R}} \frac{|w(\xi)|^2}{(1+|\xi|^2)^{\frac{1}{2}}} d\xi &\leq \left(\sum_{n=1}^{\infty}\left(\frac{1}{n^{2s}}\int_{\mathbb{R}}\frac{|J_n(\xi)|^2}{(1+|\xi|^2)^{\frac{1}{2}}}d\xi\right) + \int_{\mathbb{R}}\frac{|J_0(\xi)|^2}{(1+|\xi|^2)^{\frac{1}{2}}}d\xi\right)\|\tilde{\varphi}\|_s^2 \\ &\leq \left(\sum_{n=1}^{\infty}\left(\frac{1}{n^{2s}}\int_{\mathbb{R}}\frac{|J_n(\xi)|^2}{|\xi|}d\xi\right) + \int_{\mathbb{R}}\frac{|J_0(\xi)|^2}{(1+|\xi|^2)^{\frac{1}{2}}}d\xi\right)\|\tilde{\varphi}\|_s^2.\end{aligned} \tag{2.107}$$

Further, in view of [28, 6.574, eq 2.], the integral involving J_n can be computed exactly for $n \geq 1$:

$$\int_{\mathbb{R}} \frac{|J_n(\xi)|^2}{|\xi|} d\xi = \frac{1}{n}. \tag{2.108}$$

It thus follows that

$$\int_{\mathbb{R}} \frac{|w(\xi)|^2}{(1+|\xi|^2)^{\frac{1}{2}}} d\xi \leq C_s \|\tilde{\varphi}\|_s^2 < \infty \tag{2.109}$$

where

$$C_s = \sum_{n=1}^{\infty}\frac{1}{n^{1+2s}} + \int_{\mathbb{R}}\frac{|J_0(\xi)|^2}{(1+|\xi|^2)^{\frac{1}{2}}}d\xi. \tag{2.110}$$

□

Corollary 3. *Let $s > 0$, $\tilde{\varphi} \in H_e^s(2\pi)$, $\varphi(t) = \tilde{\varphi}(\arccos(t))$, $\varphi : [-1,1] \to \mathbb{C}$, $\alpha(\mathbf{p}) = \varphi(\mathbf{r^{-1}}(\mathbf{p}))$ and $W(\mathbf{p}) = \omega(\mathbf{r^{-1}}(\mathbf{p}))$. Then, the function $F = \frac{\alpha}{W}$ is an element of $\tilde{H}^{-\frac{1}{2}}(\Gamma)$.*

Proof. It suffices to take show that $f = \varphi/\omega \in \tilde{H}^{-\frac{1}{2}}[-1,1]$ for the case $\Gamma = [-1,1]$. Extending f by 0 outside the interval $[-1,1]$, the Fourier transform of f is given by

$$\hat{f}(\xi) = \int_{-\infty}^{\infty} f(t)e^{-i\xi t}dt = \int_{-1}^{1}\frac{\varphi(t)e^{-i\xi t}}{\omega(t)}dt = \int_0^{\pi}\tilde{\varphi}(\theta)e^{-i\xi\cos\theta}d\theta, \tag{2.111}$$

since $\omega(t) = \sqrt{1-t^2}$ in the present case. The Corollary now follows from Lemma 6. □

Lemma 7. *For all $s > 0$ the operator $\tilde{S} : H_e^s(2\pi) \to H_e^{s+1}(2\pi)$ is invertible, and the inverse $\tilde{S}^{-1} : H_e^{s+1}(2\pi) \to H_e^s(2\pi)$ is a bounded operator.*

Proof. Let $s > 0$ be given. From equation (2.30) it follows that $\tilde{S}_0 : H_e^s(2\pi) \to H_e^{s+1}(2\pi)$ is a continuously invertible operator. The same clearly holds for $\tilde{S}_0^\tau$ as well, and we may write

$$\tilde{S} = \tilde{S}_0^\tau \left(I + \left(\tilde{S}_0^\tau \right)^{-1} (\tilde{S} - \tilde{S}_0^\tau) \right). \tag{2.112}$$

It follows from Lemma 5 that the operator $(\tilde{S}_0^\tau)^{-1}(\tilde{S} - \tilde{S}_0^\tau)$ is bounded from $H_e^s(2\pi)$ into $H_e^{s+1}(2\pi)$, and therefore, in view of the Sobolev embedding theorem it defines a compact mapping from $H_e^s(2\pi)$ into itself. Further, in view of Corollary 3 and the injectivity of the mapping (1.38) it follows that the operator $\tilde{S} : H_e^s(2\pi) \to H_e^{s+1}(2\pi)$ is injective, and therefore, so is

$$\left(\tilde{S}_0^\tau \right)^{-1} \tilde{S} = I + \left(\tilde{S}_0^\tau \right)^{-1} (\tilde{S} - \tilde{S}_0^\tau) : H_e^s(2\pi) \to H_e^s(2\pi). \tag{2.113}$$

A direct application of the Fredholm theory thus shows that the operator (2.113) is continuously invertible, and the lemma follows. □

2.3.2 Bicontinuity of $\tilde{N}$

To study the mapping properties of the operator $\tilde{N}$ we rely on Lemma 8 below where, as in [49], the operator $\tilde{N}$ is recast in terms of an expression which involves tangential differential operators (cf. also [24, Th. 2.23] for the corresponding result for closed surfaces). The needed relationships between normal vectors, tangent vectors and parameterizations used are laid down in the following definition.

Definition 5. *For a given (continuous) selection of the normal vector $\boldsymbol{n} = \boldsymbol{n}(\boldsymbol{r})$ on Γ, the tangent vector $\boldsymbol{t}(\boldsymbol{r})$ is the unit vector that results from a 90° clockwise rotation of $\boldsymbol{n}(\boldsymbol{r})$. Throughout this chapter it is further assumed that the parameterization $\boldsymbol{r} = \boldsymbol{r}(t)$ of the curve Γ has been selected in such a way that*

$$\frac{d\boldsymbol{r}}{dt}(t) = \left| \frac{d\boldsymbol{r}}{dt} \right| \boldsymbol{t}(\boldsymbol{r}(t)). \tag{2.114}$$

Lemma 8. *For $\varphi \in C^\infty(\Gamma)$, and for $t \in (-1,1)$, the quantity $N_\omega[\varphi](t)$ defined by equation* (2.8) *can be expressed in the form*

$$N_\omega[\varphi](t) = N_\omega^g[\varphi](t) + N_\omega^{pv}[\varphi](t) \tag{2.115}$$

where

$$N_\omega^g[\varphi](t) = k^2 \int_{-1}^{1} G_k(\mathbf{r}(t), \mathbf{r}(t'))\ \varphi(t')\ \tau(t')\ \sqrt{1-t'^2}\ \mathbf{n}_t \cdot \mathbf{n}_{t'}\ dt', \tag{2.116}$$

and where

$$N_\omega^{pv}[\varphi](t) = \frac{1}{\tau(t)} \frac{d}{dt} \left(\int_{-1}^{1} G_k(\mathbf{r}(t), \mathbf{r}(t'))\ \frac{d}{dt'} \left(\varphi(t')\ \sqrt{1-t'^2} \right) dt' \right). \tag{2.117}$$

Proof. See Appendix 2.5.1. □

In order to continue with our treatment of the operator $\tilde{N}$ we note that, using the changes of variables $t = \cos\theta$ and $t' = \cos\theta'$ in equations (2.116) and (2.117) together with the notation (2.16), for $\varphi \in C^\infty(\Gamma)$ and for $\theta \in (0,\pi)$ we obtain

$$\tilde{N}[\tilde{\varphi}] = \tilde{N}^g[\tilde{\varphi}] + \tilde{N}^{pv}[\tilde{\varphi}], \tag{2.118}$$

where

$$\tilde{N}^g[\tilde{\varphi}](\theta) = k^2 \int_0^{\pi} G_k(\mathbf{r}(\cos\theta), \mathbf{r}(\cos\theta'))\ \tilde{\varphi}(\theta')\ \tau(\cos\theta')\ \sin^2\theta'\ \mathbf{n}_\theta \cdot \mathbf{n}_{\theta'}\ d\theta', \tag{2.119}$$

and where, taking into account equations (2.33) and (2.34),

$$\tilde{N}^{pv}[\tilde{\varphi}](\theta) = \frac{1}{\tau(\cos\theta)} \left(\tilde{D}_0 \tilde{S} \tilde{T}_0^\tau \right) [\tilde{\varphi}](\theta), \tag{2.120}$$

with

$$\tilde{T}_0^\tau[\tilde{\varphi}](\theta) = \frac{1}{\tau(\cos\theta)} T_0[\tilde{\varphi}](\theta). \tag{2.121}$$

Lemma 9. *Let $s > 0$. The operator $\tilde{N}^{pv}$ defines a bounded mapping from $H_e^{s+1}(2\pi)$ to $H_e^s(2\pi)$. Further, the difference $(\tilde{N}^{pv} - \tilde{N}_0^\tau)$ (see equation* (2.93)*) defines a bounded mapping from $H_e^{s+1}(2\pi)$ into $H_e^{s+1}(2\pi)$.*

Proof. Using (2.32) (2.93) and (4.20) we obtain

$$\tilde{N}^{pv}[\tilde{\varphi}] = \tilde{N}_0^{\tau}[\tilde{\varphi}] + \frac{1}{\tau(\cos\theta)}\tilde{D}_0(\tilde{S} - \tilde{S}_0^{\tau})\tilde{T}_0^{\tau}[\tilde{\varphi}]. \tag{2.122}$$

As shown in Theorem 3 the operator $\tilde{N}_0^{\tau} : H_e^{s+1}(2\pi) \to H_e^s(2\pi)$ on the right-hand side of this equation is bounded. To establish the continuity of the second term on the right-hand side of equation (2.122) we first note that, in view of equation (2.34), the operator $\tilde{T}_0 : H_e^{s+1}(2\pi) \to H_e^s(2\pi)$ is bounded, and therefore, so is $\tilde{T}_0^{\tau}$. Further, as shown in Lemma 5, the operator $(\tilde{S} - \tilde{S}_0^{\tau})$ maps continuously $H_e^s(2\pi)$ into $H_e^{s+3}(2\pi)$ so that, to complete the proof, it suffices to show that the operator $\tilde{D}_0$ maps continuously $H_e^{s+3}(2\pi)$ into $H_e^{s+1}(2\pi)$. But, for $\tilde{\psi} \in H_e^{s+3}(2\pi)$ $(s > 0)$ we can write

$$\tilde{D}_0[\tilde{\psi}](\theta) = \frac{1}{\sin\theta}\int_0^{\theta} \frac{d^2}{d\theta^2}\tilde{\psi}(u)du,$$

and since the zero-th-order term in the cosine expansion of $\frac{d^2}{d\theta^2}\tilde{\psi}$ vanishes, in view of (2.42) we have

$$\tilde{D}_0[\tilde{\psi}] = \tilde{C}\left[\frac{d^2\tilde{\psi}}{d\theta^2}\right].$$

It therefore follows from (2.47) that the second term in (2.122) is a continuous map from $H_e^{s+1}(2\pi)$ into $H_e^s(2\pi)$, that is, $(\tilde{N}^{pv} - \tilde{N}_0^{\tau})$, as claimed. □

Corollary 4. *For all $s > 0$ the operator $\tilde{N}$ can be extended as a continuous linear map from $H_e^{s+1}(2\pi)$ to $H_e^s(2\pi)$. Further, the difference $\tilde{N} - \tilde{N}_0^{\tau}$ defines a continuous operator from $H_e^{s+1}(2\pi)$ to $H_e^{s+1}(2\pi)$.*

Proof. From equation (2.119) we see that $\tilde{N}^g$ has the same mapping properties as $\tilde{S}$ (Lemma 5), namely

$$\tilde{N}^g : H_e^s(2\pi) \to H_e^{s+1}(2\pi) \quad \text{is continuous.} \tag{2.123}$$

In view of Lemma 9 it therefore follows that the right-hand side of equation (2.118),

$$\tilde{N}^g + \tilde{N}^{pv} : H_e^{s+1}(2\pi) \to H_e^s(2\pi), \tag{2.124}$$

is a bounded operator for all $s > 0$. Equation (2.118) was established for functions $\tilde{\varphi}$ of the

form (2.16) with $\varphi \in C^\infty(\Gamma)$. But the set of such functions $\tilde{\varphi}$ is dense in $H_e^{s+1}(2\pi)$ for all $s > 0$—as can be seen by considering, e.g., that the Chebyshev polynomials span a dense set in $H^{s+1}[-1,1]$. It follows that $\tilde{N}$ can be uniquely extended to a continuous operator from $H_e^{s+1}(2\pi)$ to $H_e^s(2\pi)$, as claimed. Finally, $\tilde{N} - \tilde{N}_0^\tau = \tilde{N}^g + (\tilde{N}^{pv} - \tilde{N}_0^\tau)$ is continuous from $H_e^{s+1}(2\pi)$ into $H_e^{s+1}(2\pi)$, in view of equation (2.123) and Lemma 9.

□

The following lemma establishes a link between the domain of the unweighted hypersingular operator $\mathbf{N}$ considered in [59] (equation (1.39) above) and the corresponding possible domains of the weighted operator $\tilde{N}$ (equation (2.21)); cf. also Corollary 3 where the corresponding result for the domains of the operators $\mathbf{S}$ and $\tilde{S}$ is given.

Lemma 10. *Let $\tilde{\psi}$ belong to $H_e^{s+1}(2\pi)$ for $s > 0$, $\psi(t) = \tilde{\psi}(\arccos t)$, $\psi : [-1,1] \to \mathbb{C}$, $\beta(\mathbf{p}) = \psi\left(\mathbf{r}^{-1}(\mathbf{p})\right)$, $W(\mathbf{p}) = \omega\left(\boldsymbol{r}^{-1}(\mathbf{p})\right)$. Then the function $G = W\beta$ is an element of $\tilde{H}^{\frac{1}{2}}(\Gamma)$.*

Proof. It suffices to show that $g = \omega\psi \in \tilde{H}^{\frac{1}{2}}[-1,1]$ for the case $\Gamma = [-1,1]$. Extending g by 0 outside the interval $[-1,1]$, the Fourier transform of g is given by

$$\hat{g}(\xi) = \int_{-1}^{1} \psi(t) e^{-i\xi t} \omega(t) dt = \int_0^\pi \psi(\cos\theta) e^{-i\xi\cos\theta} \sin^2\theta d\theta, \tag{2.125}$$

since $\omega(t) = \sqrt{1-t^2}$ in the present case. Integrating by parts we obtain

$$\hat{g}(\xi) = \frac{1}{i\xi} \int_0^\pi \frac{\partial}{\partial\theta} \left\{\psi(\cos\theta)\sin\theta\right\} e^{-i\xi\cos\theta} d\theta. \tag{2.126}$$

It is easy to check that $\frac{\partial}{\partial\theta}\{\psi(\cos\theta)\sin\theta\} = \frac{\partial}{\partial\theta}\{\tilde{\psi}(\theta)\sin\theta\}$ is an element of $H_e^s(2\pi)$ and, thus, in view of equation (2.126) together with Lemma 6 we obtain

$$\int_{\mathbb{R}} \frac{|\hat{g}(\xi)|^2 \xi^2}{(1+\xi^2)^{\frac{1}{2}}} d\xi < \infty \tag{2.127}$$

It thus follows that the second term on the right-hand side of the identity

$$\int_{\mathbb{R}} |\hat{g}(\xi)|^2 (1+|\xi|^2)^{\frac{1}{2}} d\xi = \int_{\mathbb{R}} \frac{|\hat{g}(\xi)|^2}{(1+\xi^2)^{\frac{1}{2}}} d\xi + \int_{\mathbb{R}} \frac{|\hat{g}(\xi)|^2 \xi^2}{(1+\xi^2)^{\frac{1}{2}}} d\xi \tag{2.128}$$

is finite. The first term is also finite, as can be seen by applying Lemma 6 directly to

equation (2.125). The function g thus belongs to $\tilde{H}^{\frac{1}{2}}[-1,1]$, and the proof is complete. □

Lemma 11. *For all $s > 0$ the operator $\tilde{N} : H_e^{s+1}(2\pi) \to H_e^s(2\pi)$ is invertible, and the inverse $\tilde{N}^{-1} : H_e^s(2\pi) \to H_e^{s+1}(2\pi)$ is a bounded operator.*

Proof. In view of Theorem 3, the operator $\tilde{N}_0^\tau : H_e^{s+1}(2\pi) \to H_e^s(2\pi)$ is bicontinuous, and we may thus write

$$\tilde{N} = \tilde{N}_0^\tau \left(I + \left(\tilde{N}_0^\tau \right)^{-1} (\tilde{N} - \tilde{N}_0^\tau) \right). \tag{2.129}$$

Since, by Corollary 4, the difference $\tilde{N} - \tilde{N}_0^\tau$ defines a bounded mapping from $H_e^{s+1}(2\pi)$ into $H_e^{s+1}(2\pi)$, it follows that the operator $\left(\tilde{N}_0^\tau \right)^{-1} (\tilde{N} - \tilde{N}_0^\tau)$ is bounded from $H_e^{s+1}(2\pi)$ into $H_e^{s+2}(2\pi)$ and, in view of the Sobolev embedding theorem, it is also compact from $H_e^{s+1}(2\pi)$ into $H_e^{s+1}(2\pi)$. The Fredholm theory can thus be applied to the operator

$$I + \left(\tilde{N}_0^\tau \right)^{-1} (\tilde{N} - \tilde{N}_0^\tau). \tag{2.130}$$

This operator is also injective, in view of Lemma 10 and the bicontinuity of the map $\mathbf{N}$ in equation (1.39), and it is therefore invertible. The Lemma then follows from the bicontinuity of the operator of $\tilde{N}_0^\tau$. □

2.4 Generalized Calderón Formula: Conclusion of the Proof of Theorem 2

Collecting results presented in previous sections we can now present a proof of Theorem 2.

Proof. The bicontinuity of the operators $\tilde{S}$, $\tilde{N}$ and $\tilde{N}\tilde{S}$ follow directly from Lemmas 5, 7, 11 and Corollary 4. To establish equation (2.19), on the other hand, we write

$$\tilde{N}\tilde{S} = \tilde{N}_0^\tau \tilde{S}_0^\tau + \tilde{K} = \tilde{J}_0^\tau + \tilde{K} \tag{2.131}$$

where as shown in Theorem 3, $\tilde{J}_0^\tau$ is bicontinuous, and where

$$\tilde{K} = \tilde{N}(\tilde{S} - \tilde{S}_0^\tau) + (\tilde{N} - \tilde{N}_0^\tau)\tilde{S}_0^\tau. \tag{2.132}$$

In view of Lemma 5, Corollary 4 and Theorem 3, the operator $\tilde{K}$ maps $H_e^s(2\pi)$ into $H_e^{s+1}(2\pi)$ and is therefore compact from $H_e^s(2\pi)$ into $H_e^s(2\pi)$. The proof is now complete. □

2.5 Appendix to Chapter 2

2.5.1 Proof of Lemma 8

Proof. Assuming $\varphi \in C^\infty(\Gamma)$, we define the weighted double layer potential by

$$\mathbf{D}_\omega[\alpha](\mathbf{r}) = \int_\Gamma \frac{\partial G(\mathbf{r},\mathbf{r}')}{\partial \mathbf{n}_{\mathbf{r}'}} \alpha(\mathbf{r}')\omega(\mathbf{r}')d\ell', \quad \mathbf{r} \text{ outside } \Gamma, \tag{2.133}$$

which, following the related closed-surface calculation presented in [24, Theorem 2.23], we rewrite as

$$\mathbf{D}_\omega[\alpha](\mathbf{r}) = -\mathrm{div}_{\mathbf{r}}\mathbf{E}[\alpha](\mathbf{r}) \tag{2.134}$$

where

$$\mathbf{E}[\alpha](\mathbf{r}) = \int_\Gamma G_k(\mathbf{r},\mathbf{r}')\alpha(\mathbf{r}')\omega(\mathbf{r}')\mathbf{n}(\mathbf{r}')d\ell'. \tag{2.135}$$

Since $\mathbf{E}[\alpha] = \mathbf{E} = (E_x, E_y)$ satisfies $\Delta\mathbf{E} + k^2\mathbf{E} = 0$, the two-dimensional gradient of its divergence can be expressed in the form

$$\text{grad div}\mathbf{E} = -k^2\mathbf{E} + \left(\frac{\partial}{\partial y}\text{curl } \mathbf{E}, -\frac{\partial}{\partial x}\text{curl } \mathbf{E}\right), \tag{2.136}$$

where the *scalar rotational* of a two-dimensional vector field $\mathbf{A} = (A_x, A_y)$ is defined by curl $\mathbf{A} = (\frac{\partial A_y}{\partial x} - \frac{\partial A_x}{\partial y})$. Since $\mathrm{curl}_{\mathbf{r}}\,(\mathbf{n}(\mathbf{r}')G(\mathbf{r},\mathbf{r}'))$ equals $-\mathbf{t}(\mathbf{r}')\cdot\nabla_{\mathbf{r}'}G(\mathbf{r},\mathbf{r}')$ (see definition 5), we obtain

$$\mathrm{curl}_{\mathbf{r}}\mathbf{E}[\alpha](\mathbf{r}) = -\int_{-1}^{1} \frac{dG_k(\mathbf{r},\mathbf{r}(t'))}{dt'}\alpha(\mathbf{r}(t'))\omega(\mathbf{r}(t'))dt'. \tag{2.137}$$

Therefore, taking the gradient of (2.134), letting $\varphi(t') = \alpha(\mathbf{r}(t'))$, using (2.6), integrating (2.137) by parts, and noting that the boundary terms vanish identically (since $\sqrt{1-t'^2} = 0$ for $t' = \pm 1$), we see that

$$\text{grad } \mathbf{D}_\omega[\alpha](\mathbf{r}) = k^2\int_\Gamma G(\mathbf{r},\mathbf{r}')\alpha(\mathbf{r}')\mathbf{n}(\mathbf{r}')\omega(\mathbf{r}')d\ell' - \left(\frac{\partial A}{\partial y}, -\frac{\partial A}{\partial x}\right), \tag{2.138}$$

where

$$A(\mathbf{r}) = \int_{-1}^{1} G(\mathbf{r}, \mathbf{r}(t')) \frac{d}{dt'} \big(\varphi(t') \sqrt{1 - t'^2}\big) dt'. \tag{2.139}$$

In view of the continuity of the tangential derivatives of single layer potentials across the integration surface (e.g., [24, Theorem 2.17]), in the limit as $\mathbf{r} \to \mathbf{r}(t) \in \Gamma$ we obtain

$$\left(\frac{\partial A(\mathbf{r}(t))}{\partial y}, -\frac{\partial A(\mathbf{r}(t))}{\partial x} \right) \cdot \mathbf{n}(\mathbf{r}(t)) = -\frac{1}{\tau(t)} \frac{dA(\mathbf{r}(t))}{dt}, \tag{2.140}$$

and the decomposition (2.115) results. □

2.5.2 Asymptotic behavior of NS[1]

In this section we demonstrate the poor quality of the composition **NS** of the unweighted hypersingular and single-layer operators by means of an example: we consider the flat arc $[-1, 1]$ at zero frequency ($\mathbf{NS} = \mathbf{N}_0\mathbf{S}_0$). In detail, in Section 2.5.3 we show that the image of **S** is not contained in the domain of **N** (and, thus, the formulation **NS** cannot be placed in the functional framework [59, 61, 65]), and in Section 2.5.4 we study the edge asymptotics of the function **NS**[1] which show, in particular, that the function 1, (which itself lies in $H^s[-1, 1]$ for arbitrarily large values of s) is mapped by the operator **NS** into a function which does not belong to the Sobolev space $H^{-\frac{1}{2}}[-1, 1]$, and, thus, to any space $H^s[-1, 1]$ with $s \geq -1/2$.

We thus consider the *unweighted* single-layer and hypersingular operators which, in the present flat-arc, zero-frequency case take particularly simple forms. In view of (1.34), the *parameter-space form* of the unweighted single-layer operator (which is defined in a manner analogous to that inherent in equation (2.7) and related text) is given by

$$S_0[\varphi](x) = -\frac{1}{2\pi} \int_{-1}^{1} \ln|x - s| \varphi(s) ds. \tag{2.141}$$

With regards to the parameter-space form N_0 of the hypersingular operator (1.35) we note, with reference to that equation, that in the present zero-frequency flat-arc case we have $\mathbf{r} = (x, 0)$, $z\mathbf{n}_{\mathbf{r}} = (0, z)$ and $-d/d\mathbf{n}_{\mathbf{r}'} = d/dz$. Since, additionally, the single-layer potential yields a solution of the Laplace equation in the variables (x, z), we have

$$4\pi N_0[\varphi](x) = -\lim_{z \to 0} \frac{d^2}{dx^2} \int_{-1}^{1} \varphi(s) \ln((x - s)^2 + z^2) ds, \tag{2.142}$$

or equivalently,

$$N_0[\varphi](x) = \frac{1}{4\pi} \lim_{z\to 0} \frac{d}{dx} \int_{-1}^{1} \varphi(s) \frac{d}{ds} \ln((x-s)^2 + z^2) ds. \tag{2.143}$$

Note that, in view of the classical regularity theory for the Laplace equation, letting z tend to zero for $-1 < x < 1$ in equation of (2.142) we also obtain, for smooth φ,

$$N_0[\varphi](x) = \frac{d^2}{dx^2} S_0[\varphi](x), \quad -1 < x < 1. \tag{2.144}$$

2.5.3 The operator S_0

Integrating (2.141) by parts we obtain

$$-2\pi S_0[1](x) = \int_{-1}^{1} \frac{d(s-x)}{ds} \ln|s-x| ds = (1-x)\ln(1-x) + (1+x)\ln(1+x) - 2, \tag{2.145}$$

and therefore

$$S_0[1](x) = \frac{1}{2\pi}\big(2 - (1-x)\ln(1-x) - (1+x)\ln(1+x)\big). \tag{2.146}$$

Incidentally, this expression shows that the unweighted single-layer operator does not map C^∞ functions into C^∞ functions up to the edge; a more general version of this result is given in [64, p. 182].

The following two lemmas provide details on certain mapping properties of the operator S_0 .

Lemma 12. *The image $S_0[1]$ of the constant function 1 by the operator (2.141) is an element of $H^{\frac{1}{2}}[-1,1]$.*

Proof. Let Γ_1 be a closed, smooth curve which includes the segment $[-1,1]$. Clearly, the function

$$f_1(s) = \begin{cases} 1, & s \in [-1,1] \\ 0, & s \in \Gamma_1 \backslash [-1,1] \end{cases} \tag{2.147}$$

belongs to $L^2(\Gamma_1)$ and therefore to $H^{-\frac{1}{2}}(\Gamma_1)$, so that, according to Definition 3, the constant 1 is in the space $\tilde{H}^{-\frac{1}{2}}[-1,1]$. In view of equation (1.38), it follows that $S_0[1] \in H^{\frac{1}{2}}[-1,1]$.

□

Lemma 13. *The image* $S_0[1]$ *of the constant function* 1 *by the operator* (2.141) *is not an element of* $\tilde{H}^{\frac{1}{2}}[-1,1]$.

Proof. In view of (2.146) and the fact that $S_0[1](x)$ is an even function of x, integration by parts yields

$$\int_{-1}^{1} e^{-i\xi x} S_0[1](x)dx = \frac{2\sin\xi}{\xi} S_0[1](1) + \frac{1}{2\pi i\xi}\int_{-1}^{1} e^{-i\xi x}\ln\frac{1-x}{1+x}dx. \tag{2.148}$$

Taking into account the identities [28, eq. 4.381, p 577]

$$\begin{cases} \int_0^1 \ln x\cos\xi x\,dx &= -\frac{1}{\xi}\left[\mathrm{si}(\xi)+\frac{\pi}{2}\right], \\ \int_0^1 \ln x\sin\xi x\,dx &= -\frac{1}{\xi}\left[\mathbf{C}+\ln\xi-\mathrm{ci}(\xi)\right], \end{cases} \qquad \xi>0 \tag{2.149}$$

where $\mathbf{C}$ is the Euler constant, and where $\mathrm{si}(\xi)$ and $\mathrm{ci}(\xi)$ are the sine and cosine integrals, respectively, (both of which are bounded functions of ξ as $|\xi|$ tends to infinity), it is easily verified that the second term in (2.148) behaves asymptotically as $\frac{\ln(\xi)}{\xi^2}$ as ξ tends to infinity. Clearly, the first term of (2.148) decays as $O(\frac{1}{\xi})$, and therefore

$$\left|\int_{-1}^{1} e^{-i\xi x}\left(S_0[1](x)\right)dx\right|^2 = O\left(\frac{1}{\xi^2}\right), \quad \xi\to\infty. \tag{2.150}$$

Equation (2.150) tells us that the function $\varphi:\mathbb{R}\to\mathbb{R}$ which equals $S_0[1](x)$ for x in the interval $[-1,1]$ and equals zero in the complement of this interval, does not belong to $H^{\frac{1}{2}}(\mathbb{R})$, and, thus, $S_0[1]\notin\tilde{H}^{\frac{1}{2}}[-1,1]$, as claimed. □

Remark 5. *Lemmas 12 and 13 demonstrate that, as pointed out in Section 1, the formulation* **NS** *of the open-curve boundary-value problems under consideration cannot be placed in the functional framework put forth in [59, 61, 65] and embodied by equations* (1.38), (1.39) *and definition 3: the image of the operator* **S** *is not contained in the domain of definition of the operator* **N***; see equations* (1.38) *and* (1.39).

2.5.4 The combination N_0S_0

While, as pointed out in the previous section, $S_0[1]$ does not belong to the domain of definition of N_0 (as set up by the formulation (1.38), (1.39)), the quantity $N_0S_0[1](x)$ can be evaluated point-wise for $|x|<1$, and it is instructive to study its asymptotics as $x\to\pm1$.

Lemma 14. *$N_0S_0[1]$ can be expressed in the form*

$$N_0S_0[1](x) = \frac{\ln 2 - 1}{\pi^2(1-x^2)} + \mathcal{L}(x), \tag{2.151}$$

where $\mathcal{L} \in L^2[-1,1]$.

Proof. In view of (2.146) we have

$$N_0S_0[1](x) = \frac{1}{\pi}N_0[1](x) - \frac{1}{2\pi}N_0[g](x), \tag{2.152}$$

where

$$g(x) = (1-x)\ln(1-x) + (1+x)\ln(1+x). \tag{2.153}$$

For the first term on the right-hand side of this equation we obtain from (2.144) and (2.146)

$$N_0[1](x) = -\frac{1}{\pi(1-x^2)}\,. \tag{2.154}$$

To evaluate the second term $N_0[g]$ in equation (2.152), in turn, we first integrate by parts equation (2.143) and take limit as $z \to 0$ and thus obtain

$$\begin{aligned} N_0[g](x) &= \frac{1}{2\pi}\left(\frac{d}{dx}\left(\left[\ln|x-s|g(s)\right]_{-1}^{1}\right) - \frac{d}{dx}\int_{-1}^{1}\ln|x-s|\frac{d}{ds}g(s)ds\right) \\ &= \frac{\ln 2}{\pi}\frac{d}{dx}\left(\ln\left(\frac{1-x}{1+x}\right)\right) + \frac{1}{2\pi}\frac{d}{dx}\int_{-1}^{1}\ln|x-s|\ln\left(\frac{1-s}{1+s}\right)ds, \end{aligned} \tag{2.155}$$

or

$$N_0[g](x) = \frac{-2\ln 2}{\pi(1-x^2)} - \frac{1}{2\pi}p.v.\int_{-1}^{1}\ln\left(\frac{1-s}{1+s}\right)\frac{1}{s-x}ds. \tag{2.156}$$

Clearly, to complete the proof it suffices to establish that the functions

$$\mathcal{L}^+(x) = p.v.\int_{-1}^{1}\frac{\ln(1-s)}{s-x}ds \quad \text{and} \quad \mathcal{L}^-(x) = p.v.\int_{-1}^{1}\frac{\ln(1+s)}{s-x}ds \tag{2.157}$$

are elements of $L^2[-1,1]$.

Let us consider the function $\mathcal{L}^+$ for $x \geq 0$ first. Re-expressing $\mathcal{L}^+(x)$ as the sum of the integrals over the interval $[x-(1-x), x+(1-x)] = [2x-1, 1]$ (which is symmetric respect

to x plus the integral over $[-1, 2x-1]$ and using a simple change of variables we obtain

$$\mathcal{L}^+(x) = \int_0^{1-x} \frac{\ln(1-x-u) - \ln(1-x+u)}{u} du + \int_{1-x}^{1+x} \frac{\ln(1-x+u)}{u} du. \tag{2.158}$$

Letting $z = 1-x$ and $v = \frac{u}{z}$, we see that the first integral in (2.158) is a constant function of x:

$$\int_0^z \frac{\ln(z-u) - \ln(z+u)}{u} du = \int_0^1 \frac{\ln(1-v) - \ln(1+v)}{v} dv = \text{const.} \tag{2.159}$$

For the second integral in (2.158), on the other hand, we write

$$\begin{aligned}
\int_{1-x}^{1+x} \frac{\ln(1+u-x)}{u} du &= \int_{1-x}^{1+x} \frac{\ln(1+\frac{u}{1-x})}{u} du + \ln(1-x) \int_{1-x}^{1+x} \frac{du}{u} \\
&= \int_1^{\frac{1+x}{1-x}} \frac{\ln(1+v)}{v} dv + \ln(1-x) \ln\left(\frac{1+x}{1-x}\right) \\
&= \int_1^{\frac{1+x}{1-x}} \frac{\ln(1+v)}{1+v} dv + \int_1^{\frac{1+x}{1-x}} \frac{\ln(1+v)}{v(1+v)} dv + \ln(1-x) \ln\left(\frac{1+x}{1-x}\right) \\
= \frac{1}{2}\left(\ln^2\left(\frac{2}{1-x}\right) - \ln^2 2\right) &+ \int_1^{\frac{1+x}{1-x}} \frac{\ln(1+v)}{v(1+v)} dv + \ln(1-x) \ln\left(\frac{1+x}{1-x}\right).
\end{aligned} \tag{2.160}$$

Since the second term on the last line of equation (2.160) is bounded for $0 \le x < 1$, it follows that, in this interval, the function $\mathcal{L}^+(x)$ equals a bounded function plus a sum of logarithmic terms and is thus an element of $L^2[0,1]$. Using a similar calculation it is easily shown that $\mathcal{L}^+(x)$ is bounded for $-1 \le x < 0$, and it thus follows that $\mathcal{L}^+ \in L^2[-1,1]$, as desired. Analogously, we have $\mathcal{L}^- \in L^2[-1,1]$, and the lemma follows. □

Corollary 5. *Let* $\Gamma = [-1,1]$. *Then* $\mathbf{NS}[1]$ *does not belong to the codomain* $H^{-\frac{1}{2}}[-1,1]$ *of the operator* $\mathbf{N}$ *in equation* (1.39).

Proof. In view of Lemma 14 it suffices to show that the function $h(x) = \frac{1}{1-x^2}$ does not belong to $H^{-\frac{1}{2}}[-1,1]$, or, equivalently, that the primitive $k(x) = -\frac{1}{2}\ln\frac{1-x}{1+x}$ of h does not belong to $H^{\frac{1}{2}}[-1,1]$. Clearly, to establish that $k \notin H^{\frac{1}{2}}[-1,1]$ it suffices to show that the function $\ell(x) = p(x)\ln(x)$ is not an element of $H^{\frac{1}{2}}[0,\infty[$, where p is a smooth auxiliary function defined for $x \ge 0$ which equals 1 in the interval $[0,1]$ and which vanishes outside the interval $[0,2]$.

To do this we appeal to the criterion [41, p. 54]

$$\ell \in H^{\frac{1}{2}}(0,\infty) \iff \ell \in L^2(0,\infty) \quad \text{and} \int_0^\infty t^{-2}dt \int_0^\infty |\ell(x+t)-\ell(x)|^2\,dx < \infty.$$

To complete the proof of the lemma it thus suffices to show that the integral

$$I = \int_0^\infty t^{-2}dt \int_0^1 |\ln(x+t)-\ln(x)|^2\,dx$$

is infinite. But, using the change of variables $u = \frac{t}{x}$ we obtain

$$I = \int_0^\infty \frac{1}{t}dt \left(\int_t^\infty \frac{|\ln(1+u)|^2}{u^2}du \right) = \infty, \tag{2.161}$$

and the lemma follows. □

Chapter 3

High-Order Solver for the Two-Dimensional TE and TM Open-Arc Problems

We present high-order quadrature rules for evaluation of the operators $\mathbf{N}_\omega$ and $\mathbf{S}_\omega$ in the two-dimensional case, which give rise to fast and highly accurate numerical solvers for the open-arc problems (1.31). This chapter is organized as follows: the new high-order rules are presented in Section 3.1; Section 3.2 then provides a numerical study of the eigenvalue distributions associated with the various operators under consideration, including an extension to the nonzero frequency case of the second-kind operator introduced in [2]. Section 3.3 finally presents numerical results obtained across a variety of geometries, including highly resonant cavities. The results confirm the spectral convergence of our algorithm, and a significant reduction in the number of GMRES iterations is observed when the combined operator $\tilde{N}\tilde{S}$ is used. In practice, we report that use of the combined equation (2.23) for the solution of the TM (Neumann) problem provides orders-of-magnitude improvements in computational time over those required by the hypersingular equation (2.12). In the case of the TE (Dirichlet) problem, on the other hand, the reduction in the number of iterations is out-weighted by the increased computational complexity associated with the evaluation of the combined operator in equation (2.22): the first-kind weighted integral equation (2.11) suffices in practice to provide highly accurate results in fast computational times for the TE problem.

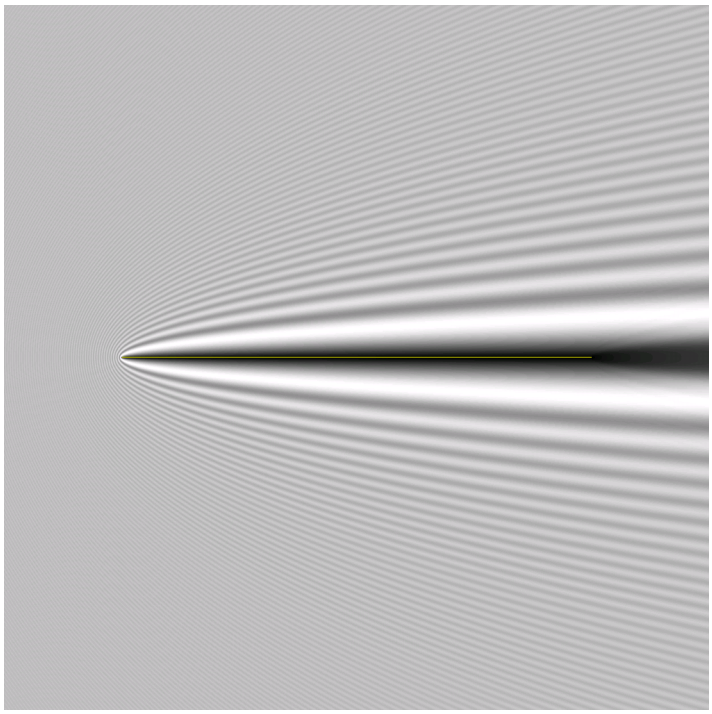

Figure 3.1: TE scattering (total field) by an infinitely thin strip of size $L = 200\lambda$ for horizontal left-to-right incidence. (The TM total field at this incidence equals the incident field.) Note the trailing shadow in the wake of the strip.

3.1 High-Order Numerical Methods

3.1.1 Spectral discretization for $\tilde{S}$

Use of the nodes $\left\{\theta_n = \frac{\pi(2n+1)}{2N}\right\}$, $n = 0, \cdots, N-1$, gives rise [54, eq. (5.8.7),(5.8.8)] to a spectrally convergent cosine representation for smooth, π-periodic and even functions $\tilde{\varphi}$:

$$\tilde{\varphi}(\theta) = \sum_{n=0}^{N-1} a_n \cos(n\theta), \quad \text{where} \quad a_n = \frac{(2-\delta_{0n})}{N} \sum_{j=0}^{N-1} \tilde{\varphi}(\theta_j)\cos(n\theta_j). \tag{3.1}$$

Thus, applying equation (2.30) to each term of expansion (3.1), we obtain the well-known *spectral* quadrature rule for the logarithmic kernel

$$\int_0^\pi \ln|\cos\theta - \cos\theta'|\tilde{\varphi}(\theta')d\theta' \sim \frac{\pi}{N}\sum_{j=0}^{N-1} \tilde{\varphi}(\theta_j)R_j^{(N)}(\theta), \tag{3.2}$$

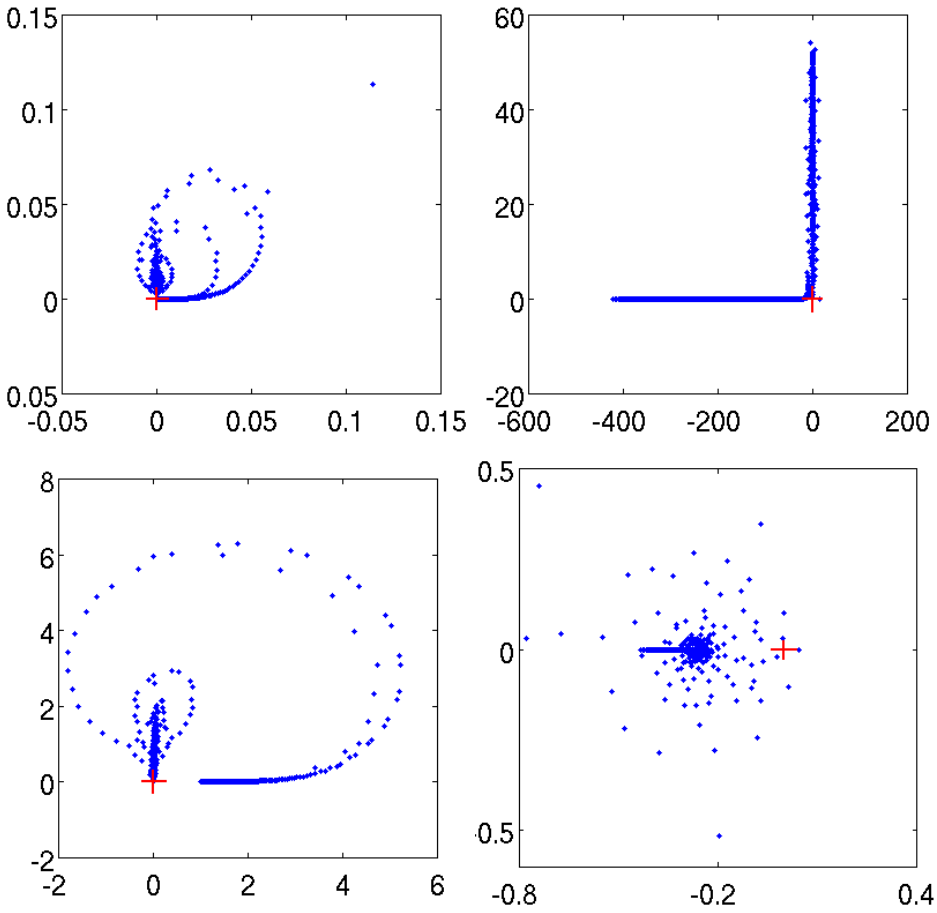

Figure 3.2: Eigenvalue distribution for the spiral-shaped arc displayed in Figure 3.5, with frequency $\frac{L}{\lambda} = 100$, for the various operators under consideration. Top left $\tilde{S}$. Top right $\tilde{N}$. Bottom left $\tilde{S}_0^{-1}\tilde{S}$. Bottom right $\tilde{N}\tilde{S}$. Note the important difference of scale between the four plots.

where

$$R_j^{(N)}(\theta) = -2\sum_{m=0}^{N-1}(2-\delta_m)\lambda_m \cos(m\theta_j)\cos(m\theta). \tag{3.3}$$

Following [25, 40, 43] we then devise a high-order integration rule for the operator $\tilde{S}$, noting first from (1.10) and (2.95) that

$$G_k(\mathbf{r}(\theta),\mathbf{r}(\theta')) = A_1(k,\cos\theta,\cos\theta')\ln|\cos\theta-\cos\theta'| + A_2(k,\cos\theta,\cos\theta'), \tag{3.4}$$

where, letting $R = |\mathbf{r}(\cos\theta) - \mathbf{r}(\cos\theta')|$ we have

$$A_1(k,\cos\theta,\cos\theta') = -\frac{1}{2\pi}J_0(kR), \tag{3.5}$$

and

$$A_2(k,\cos\theta,\cos\theta') = \frac{i}{4}H_0^1(kR) + \frac{1}{2\pi}J_0(kR)\ln|\cos\theta-\cos\theta'|. \tag{3.6}$$

In view of (2.95) and the smoothness of the ratio $\frac{R}{|\cos\theta-\cos\theta'|}$, the functions A_1 and A_2 are even, smooth (analytic for analytic arcs) and 2π-periodic functions of θ and θ'—and, thus, in view of (3.2), the expression

$$\int_0^\pi \tilde{\varphi}(\theta')A_1(k,\cos\theta,\cos\theta')\ln|\cos\theta-\cos\theta'|\tau(\cos\theta')d\theta' \sim \frac{\pi}{N}\sum_{j=0}^{N-1}\tilde{\varphi}(\theta_j)\tau(\cos\theta_j)A_1(k,\cos\theta,\cos\theta_j)R_j^{(N)}(\theta)$$

provides a spectrally accurate quadrature rule. By making use of trapezoidal integration for the second term in the right-hand side of (3.4) we therefore obtain the spectrally accurate quadrature approximation of the operator $\tilde{S}$:

$$\tilde{S}[\varphi](\theta) \sim \frac{\pi}{N}\sum_{j=0}^{N-1}\tilde{\varphi}(\theta_j)\tau(\cos\theta_j)\big(A_1(k,\cos\theta,\cos\theta_j)R_j^{(N)}(\theta) + A_2(k,\cos\theta,\cos\theta_j)\big). \tag{3.7}$$

3.1.2 Efficient implementation

The right-hand side of (3.7) can be evaluated directly for all θ in the set of quadrature points $\{\theta_n, n = 0,\ldots,N-1\}$ by means of a matrix-vector multiplication involving the matrix $S^{(N)}$

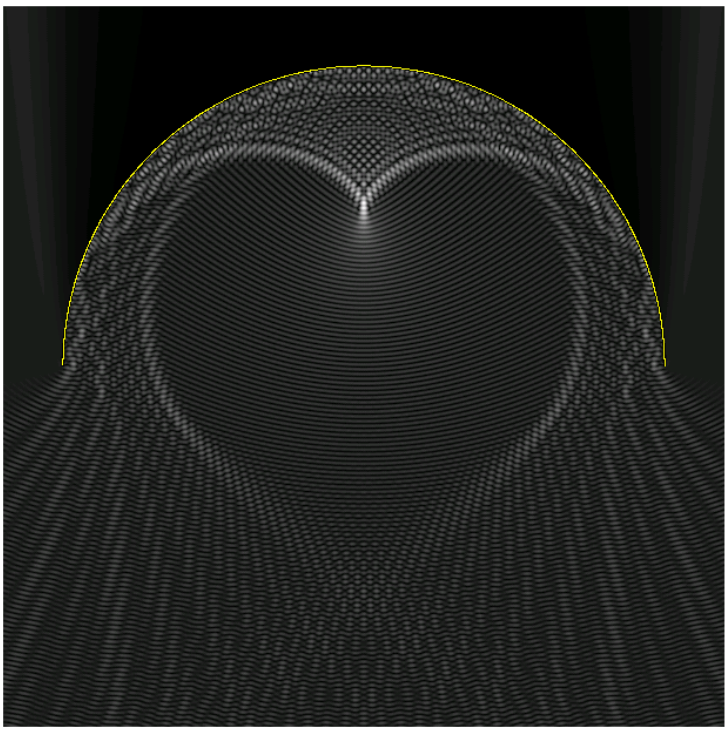

Figure 3.3: TM solution for a half-circle of size $L = 200\lambda$ under normal incidence from below. Note the caustics inside the circular reflector.

whose elements are defined by

$$S_{nj}^{(N)} = \frac{\pi}{N}\tau(\cos\theta_j)\left(A_1(k,\cos\theta_n,\cos\theta_j)R_j^{(N)}(\theta_n) + A_2(k,\cos\theta_n,\cos\theta_j)\right). \tag{3.8}$$

A direct evaluation of the matrix $S^{(N)}$ on the basis of (3.3) requires $O(N^3)$ operations; as shown in what follows, however, the matrix $S^{(N)}$ can be produced at significantly lower computational cost. Indeed, expressing the product of cosines in (3.3) as a sum of cosines of added and subtracted angles, the quantities

$$R_j^{(N)}(\theta_n) = -\sum_{m=0}^{N-1}(2-\delta_m)\lambda_m\big(\cos(\frac{m\pi}{N}|n-j|) + \cos(\frac{m\pi}{N}(n+j+1))\big) \tag{3.9}$$

can be expressed in the form

$$R_j^N(\theta_n) = R^{(N)}(|n-j|) + R^{(N)}(n+j+1), \tag{3.10}$$

N	TE case, $\tilde{S}$	TE case, $\tilde{N}\tilde{S}$	TM case, $\tilde{N}$	TM case, $\tilde{N}\tilde{S}$
3000	5.4×10^{-6}	8.2×10^{-6}	1.5×10^{-3}	2.8×10^{-4}
3100	4.5×10^{-8}	4.9×10^{-8}	1.0×10^{-5}	5.5×10^{-6}
3350	8.4×10^{-12}	8.5×10^{-12}	3.7×10^{-10}	3.7×10^{-11}

Table 3.1: Scattering by a spiral-shaped arc of size $\frac{L}{\lambda} = 400$: far-field errors

where the vector $R^{(N)}$ is given by

$$R^{(N)}(\ell) = -\sum_{m=0}^{N-1}(2-\delta_m)\lambda_m \cos(\frac{m\pi}{N}\ell),\ \ \ell \in [0, 2N-1]. \tag{3.11}$$

Our algorithm evaluates this vector efficiently by means of an FFT, and produces as a result the matrix $S^{(N)}$ at an overall computational cost of $O(N^2 \ln N)$ operations. This fast spectrally accurate algorithm could be further accelerated, if necessary, by means of techniques such as those presented in References [5, 17, 55].

3.1.3 Spectral discretization for $\tilde{N}$

In order to evaluate $\tilde{N}$ we use (2.118), the first term of which is a single-layer operator which can be evaluated by means of a rule analogous to (3.7) and a rapidly computable matrix $N^{g,(N)}$ (similar to $S^{(N)}$) with elements

$$N^{g,(N)}_{nj} = \frac{k^2\pi}{N}\tau(\cos\theta_j)\sin^2\theta_j(\mathbf{n}_{\theta_j}\cdot\mathbf{n}_{\theta_n})\left(A_1(k,\cos\theta_n,\cos\theta_j)R^{(N)}_j(\theta_n) + A_2(k,\cos\theta_n,\cos\theta_j)\right). \tag{3.12}$$

To evaluate the second term in (2.118), in turn, we make use of the decomposition (4.20), and we approximate the quantity $\tilde{T}^{\tau}_0[\tilde{\varphi}]$ by means of term per term differentiation of the sine expansion of the function $\tilde{\varphi}(\theta)\sin(\theta)$ (which can itself be produced efficiently by means of an FFT). Since $\tilde{D}_0$ is essentially the differentiation operator in the x variable,

$$\frac{1}{\sin\theta}\frac{d}{d\theta}\left(\varphi(\cos\theta)\right) = -\frac{d}{dx}\left(\varphi(x)\right),$$

our solver evaluates the quantity $\tilde{D}_0[\tilde{\varphi}]$ by invoking classical FFT-based Chebyshev differentiation rules [54, p. 195].

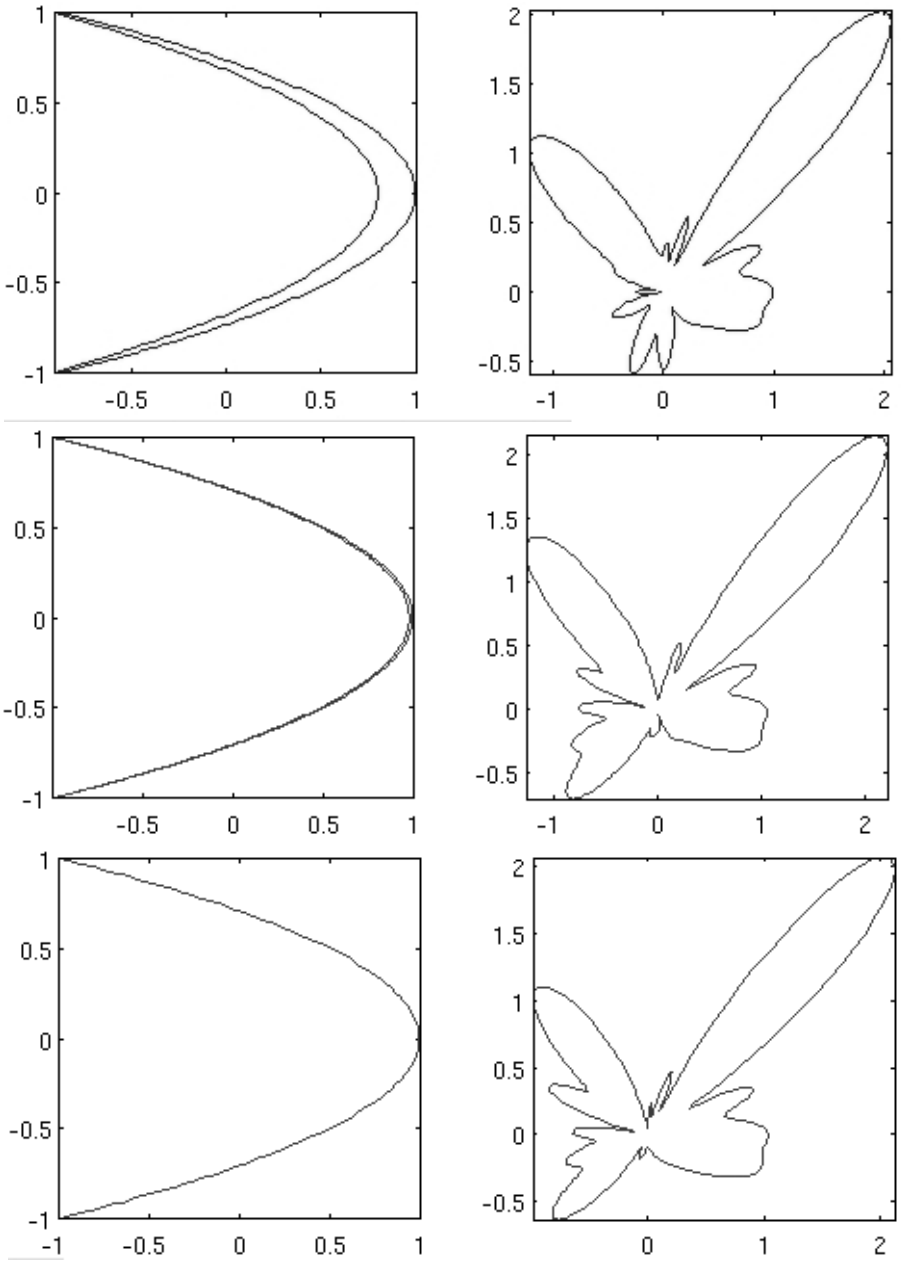

Figure 3.4: A sequence of increasingly thin closed curves converging to the open parabolic scatterer $x = 1 - 2y^2$ and corresponding far-field patterns. From top to bottom: closed curve with a=0.9, corresponding far field, closed curve with a=0.99, corresponding far field, parabolic (open) arc and corresponding far field. Note the convergence of the far-field patterns as the closed scatterers approach the open parabolic scatterer.

				TE($\tilde{S}$)		TE($\tilde{N}\tilde{S}$)	
$\frac{L}{\lambda}$	N	ϵ_r	Mat.	It.	Time	It.	Time
50	400	$< 10^{-5}$	$< 1s$	24	$< 1s$	8	$< 1s$
200	1600	$< 10^{-5}$	$4s$	33	$1s$	8	$2s$
800	6400	$< 10^{-5}$	$54s$	45	$18s$	8	$15s$

Table 3.2: Iteration numbers and computing times for the TE (Dirichlet) problem on the flat strip

				TE($\tilde{S}$)		TE($\tilde{N}\tilde{S}$)	
$\frac{L}{\lambda}$	N	ϵ_r	Mat.	It.	Time	It.	Time
50	400	$< 10^{-5}$	$< 1s$	64	$< 1s$	46	$< 1s$
200	1600	$< 10^{-5}$	$4s$	93	$3s$	62	$8s$
800	6400	$< 10^{-5}$	$55s$	136	$58s$	79	$158s$

Table 3.3: Iteration numbers and computing times for the TE (Dirichlet) problem on the spiral-shaped arc

3.2 Eigenvalue Distributions

In order to gain additional insights on the character of the various $k \neq 0$ open-arc operators under consideration (namely, $\tilde{S}$, $\tilde{N}$, $\tilde{N}\tilde{S}$ as well as a generalization to nonzero frequencies of the operator introduced in reference [2]), we consider their corresponding eigenvalue distributions. In Figure 3.2 we thus display the eigenvalues associated with these operators, for the spiral-shaped arc displayed in Figure 3.5 and described in Section 3.3, as they were produced by means of the quadrature rules presented in Section 3.1 and subsequent evaluation of matrix eigenvalues. The frequency was chosen to ensure a size to wavelength ratio $\frac{L}{\lambda} = 100$, where L is the length of the arc and λ the wavelength of the incident wave. As expected, the eigenvalues of $\tilde{S}$ tend slowly to zero, the eigenvalues of $\tilde{N}$ are large, while the eigenvalues of $\tilde{N}\tilde{S}$ are bounded away from zero and infinity, and they accumulate at $-\frac{1}{4}$.

The $k > 0$ generalization of the equation [2], whose operator eigenvalues are displayed in the center-right portion of Figure 3.2, is obtained from right-multiplication of the single-layer operator in equation (2.11) by the inverse of the flat-arc zero-frequency single-layer operator $\tilde{S}_0^\tau$ (defined in equation (2.92) below); the resulting equation is given by

$$\tilde{S}(\tilde{S}_0^\tau)^{-1}[\tilde{\varphi}] = \tilde{f}. \tag{3.13}$$

This equation, which can be re-expressed in the form

$$\left(I + (\tilde{S} - \tilde{S}_0^\tau)(\tilde{S}_0^\tau)^{-1}\right)[\tilde{\varphi}] = \tilde{f}, \tag{3.14}$$

is a second-kind Fredholm integral equation: the operator

$$\left(\tilde{S} - \tilde{S}_0^\tau\right)(\tilde{S}_0^\tau)^{-1} : H_e^s(2\pi) \to H_e^s(2\pi) \tag{3.15}$$

is compact. Unfortunately, the spectrum of the operator in equation (3.13) is highly unfavorable at high frequencies, as illustrated in the center-right image in Figure 3.2. Such poor spectral distributions translate into dramatic increases, demonstrated in Table 3.6, in the number of iterations required to solve (3.13) by means of Krylov subspace solvers as the frequency grows. In fact, a direct comparison with Table 3.3 shows that the second-kind integral equation (3.13) may require many more iterations at nonzero frequencies than the original first-kind equation (2.11).

3.3 Numerical Results

The numerical results presented in what follows were obtained by means of a C++ implementation of the quadrature rules introduced in Section 3.1 for numerical evaluation of the operators $\tilde{S}$ and $\tilde{N}$ (and thus, through composition, $\tilde{N}\tilde{S}$), in conjunction with the iterative linear algebra solver GMRES [56]. In all cases the errors reported were evaluated by comparisons with highly resolved numerical solutions. All runs were performed in a single 2.2 GHz Intel processor.

3.3.1 Spectral convergence

To demonstrate the high-order character of the algorithm described in previous sections we consider the problems of TE and TM scattering by the exponential spiral

$$\begin{cases} x(s) = e^s \cos(5s) \\ y(s) = e^s \sin(5s) \end{cases} \tag{3.16}$$

of size $\frac{L}{\lambda} = 800$, where L and λ denote the perimeter of the curve and the electromagnetic wavelength, respectively. Table 3.1 demonstrates the spectral (exponentially fast) conver-

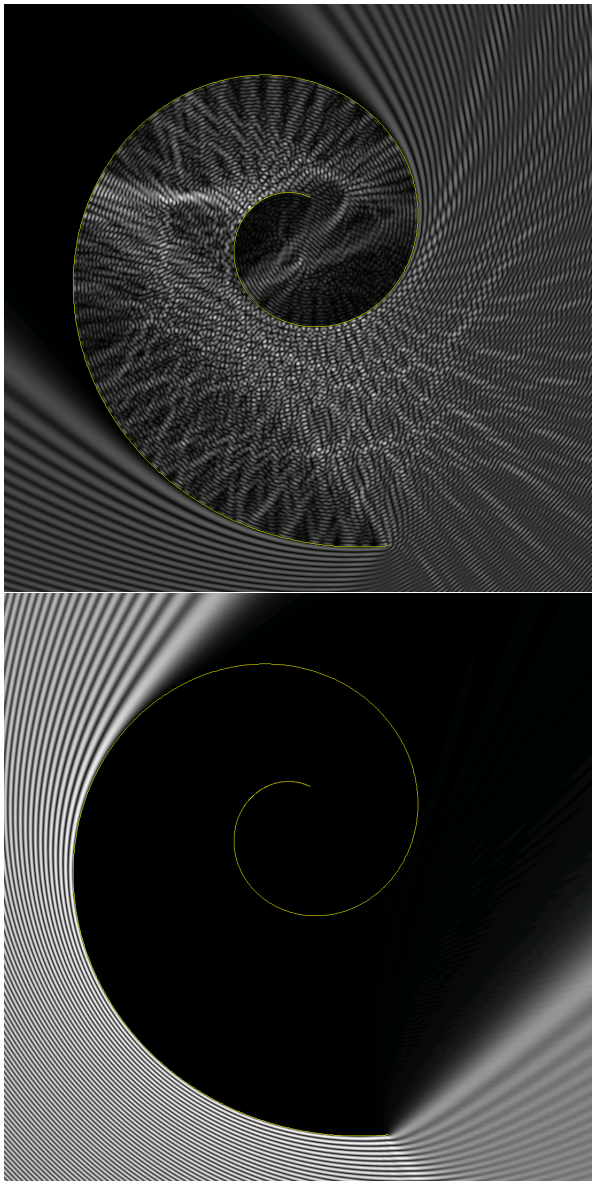

Figure 3.5: TE-diffraction by a spiral-shaped arc of size $L = 200\lambda$, for incidence angles of 135° (top) and 45° (bottom) from the positive x-axis. The top figure shows internal reflections that enable the field to penetrate to the center of the spiral, giving rise to an interesting array of caustics. The relative error ϵ_r in both numerical solutions is no larger than 10^{-5}.

				TM($\tilde{N}$)		TM($\tilde{N}\tilde{S}$)	
$\frac{L}{\lambda}$	N	ϵ_r	Mat.	It.	Time	It.	Time
50	400	$< 10^{-5}$	$< 1s$	67	$< 1s$	9	$< 1s$
200	1600	$< 10^{-5}$	$4s$	160	$16s$	9	$1s$
800	6400	$< 10^{-5}$	$55s$	298	$415s$	9	$17s$

Table 3.4: Iteration numbers and computing times for the TM (Neumann) problem on the strip

				TM($\tilde{N}$)		TM($\tilde{N}\tilde{S}$)	
$\frac{L}{\lambda}$	N	ϵ_r	Mat.	It.	Time	It.	Time
50	400	$< 10^{-5}$	$< 1s$	202	$< 1s$	48	$< 1s$
200	1600	$< 10^{-5}$	$3s$	432	$65s$	63	$8s$
800	6400	$< 10^{-5}$	$55s$	849	$1692s$	83	$160s$

Table 3.5: Iteration numbers and computing times for the TM (Neumann) problem on the spiral-shaped arc

gence of the TE and TM numerical solutions produced by means of the operators $\tilde{S}$, $\tilde{N}$ and $\tilde{N}\tilde{S}$ for this problem (cf. equations (2.11)–(2.12) and (2.22) and (2.23)); note from Figure 3.5 the manifold caustics and multiple reflections associated with this solution.

3.3.2 Limit of closed curves

In order to obtain an indication of the manner in which an open arc problem can be viewed as a limit of closed-curve problems (and, in addition, to provide an independent verification of the validity of our solvers) we consider a test case in which the open arc parabolic scatterer $x = 1 - 2y^2$ is viewed as the limit as $a \to 1$ of the family of closed curves

$$\begin{cases} x(s) = (1-a)\cos s + a\cos(2s) \\ y(s) = \sin s \end{cases} . \tag{3.17}$$

Using the closed-curve Nyström algorithms [25] we evaluate the TE fields scattered by these closed curves at $k = 10$ for values of a approaching $a = 1$. Figure 3.4 displays the $k = 10$ far fields corresponding to $a = 0.9$ and $a = 0.99$ side-by-side the corresponding far-field pattern for the limiting open parabolic arc as produced by the $\tilde{S}$-based open-arc solver. Clearly the closed-curve and open-arc solutions are quite close to each other. As might be expected, as a approaches 1 an increasingly dense discretization is needed to maintain accuracy in the closed-curve solution: for $a = 0.9$, 256 points where needed to reach a far-field error of 10^{-4},

$\frac{L}{\lambda}$	N	ϵ_r	It.	Mat. Time	Sol. Time
50	400	1.2×10^{-5}	124	$< 1s$	$1s$
200	1600	6.3×10^{-6}	293	$3s$	$15s$
800	6400	2.2×10^{-5}	672	$56s$	$411s$

Table 3.6: Conditioning and times for the solution of the Dirichlet problem using the generalization of the method [2, 37]: $(\tilde{S}_0^\tau)^{-1}$ as a preconditioner for the spiral-shaped arc.

while for $a = 0.99$ as many 1024 points were needed to reach the same accuracy—even for the low frequency under consideration. The corresponding open-arc solution, in contrast, was produced with 10^{-4} accuracy by means of a much coarser, 64 point discretization.

3.3.3 Solver performance

The TE (Dirichlet) problem can be solved by means of either the left-hand equation in (2.11) or equation (2.22), which in what follows are called equations TE($\tilde{S}$) and TE($\tilde{N}\tilde{S}$), respectively. The TM (Neumann) problem, similarly, can be tackled by means of either the right-hand equation in (2.12) or equation (2.23); we call these equations TM($\tilde{N}$) and TM($\tilde{N}\tilde{S}$), respectively. Results for TE and TM problems obtained by the various relevant equations for two representative geometries, a strip $[-1, 1]$ and the exponential spiral mentioned above in this section, are presented in Figures 3.1 and 3.5 and Tables 3.2 through 3.5. In the tables the abbreviation "It." denotes the number of iterations required to achieve an ϵ_r relative maximum error in the far-field (calculated as the quotient of the maximum absolute error in the far-field by the maximum absolute value of the far-field), "Mat." is the time needed to build the $\tilde{S}$ matrix given by equation (3.8), as well as (when required) the corresponding matrix for $\tilde{N}^g$ which can be constructed in $O(N^2)$ operations from the $\tilde{S}$ matrix (see Section 3.1), and "Time" is the total time required by the solver to find the solution once the matrix is stored.

As can be seen from these tables, the TM equation TM($\tilde{N}$) requires very large number of iterations as the frequency grows and, thus, the computing times required by the low-iteration second-kind equation TM($\tilde{N}\tilde{S}$) are significantly lower than those required by TM($\tilde{N}$). The situation is reversed for the TE problem: although, the corresponding second-kind equation TE($\tilde{N}\tilde{S}$) requires fewer iterations than TE($\tilde{S}$), the total computational cost of the second-kind equation is generally higher in this case—since the application of the operator in TE($\tilde{S}$) is significantly less expensive than the application of operator in TE($\tilde{N}\tilde{S}$).

3.3.4 Resonant cavities.

We have found that interesting resonant electromagnetic behavior arises from diffractive elements constructed as almost-closed open-arcs. As can be seen first in Figures 3.6 and 3.7, circular and rocket-shaped cavities with small openings (a few wavelengths in size), can give rise to interesting and highly energetic field patterns within the open cavity. The number of iterations required for each of these configurations is of course much larger than for simpler geometries, such as the strip. Yet, overall reduction in number of iterations and computing times is observed when the equation TM($\tilde{N}\tilde{S}$) is used in lieu of TM($\tilde{N}$). For the TE problem, once again TE($\tilde{S}$) gives rise to faster overall numerics than TE($\tilde{N}\tilde{S}$), although the latter equation still requires fewer GMRES iterations. Finally, Figure 3.8 is provided as an example of the kind of systematic studies that can be undertaken now that a high-order solver is at hand: for slowly decreasing aperture sizes, the maximum intensity inside a circular cavity of size $\frac{L}{\lambda} = 80$ is displayed. A strong peak in energy is reached as the aperture size reduces, until the aperture sizes decreases below the wavelength, at which point the energy rapidly drops.

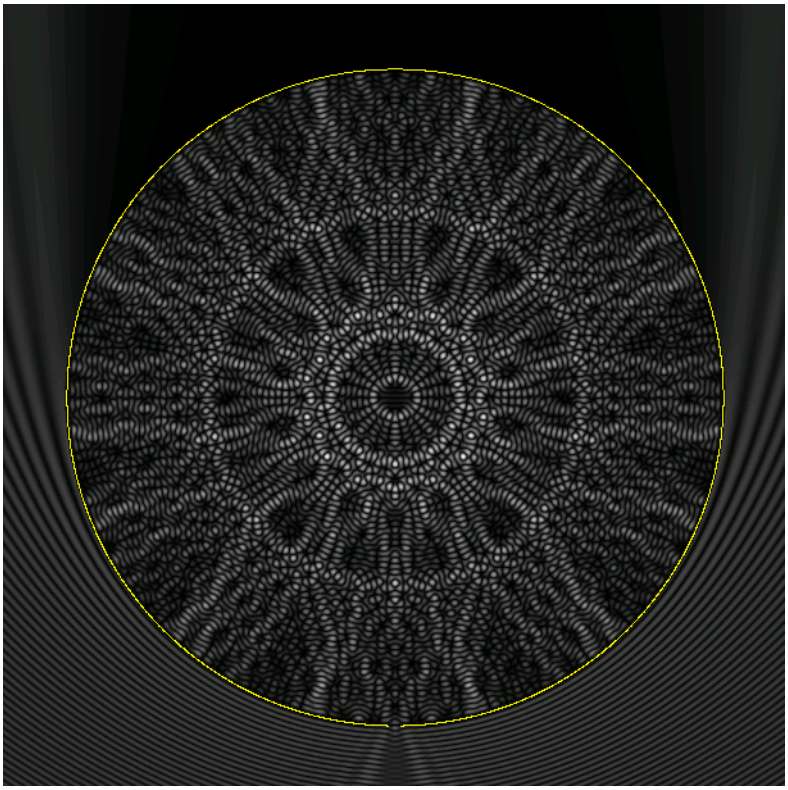

Figure 3.6: TM polarization, for a circular cavity of size $\frac{L}{\lambda} = 200$, with a bottom aperture of size equal to the wavelength λ.

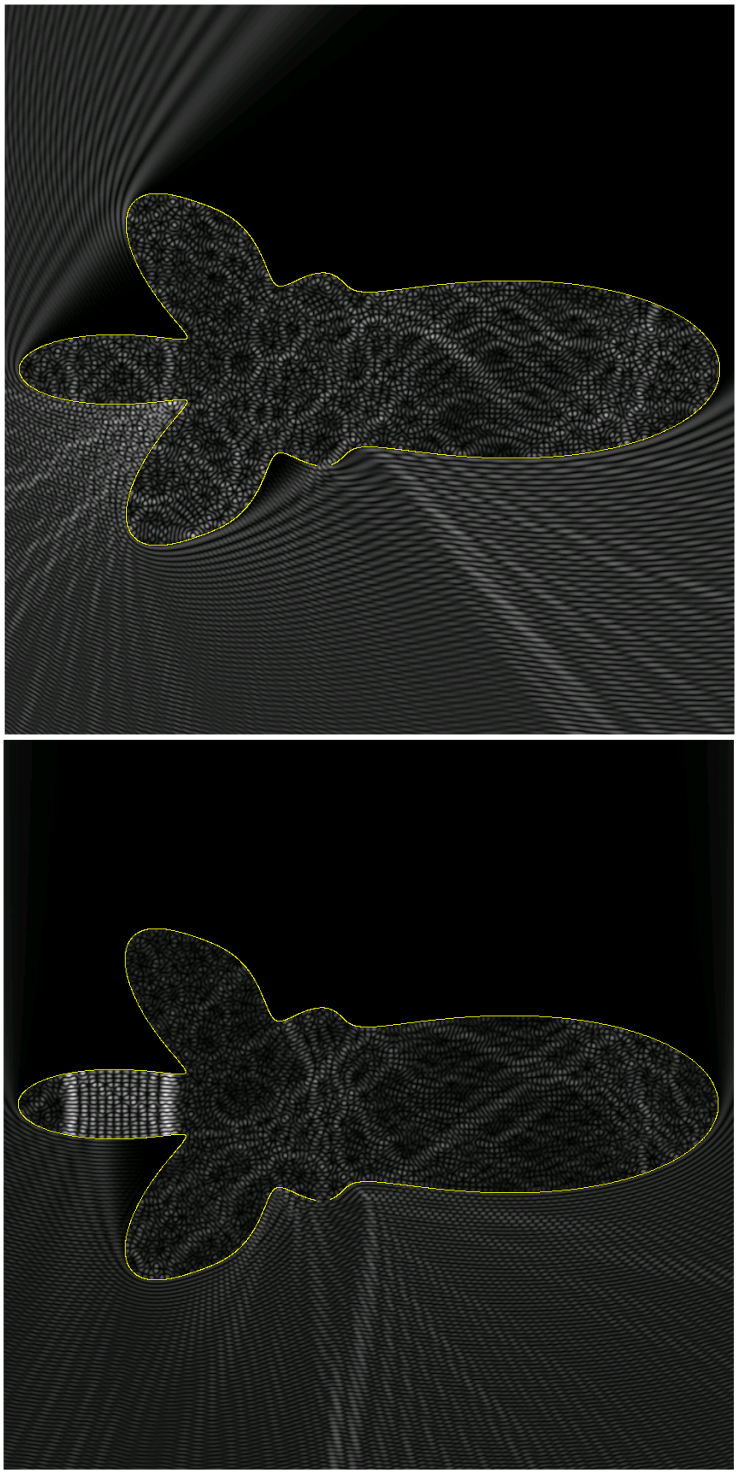

Figure 3.7: Top: TE problem for a rocket-shaped cavity with perimeter $L = 200\lambda$, and a bottom aperture equal to 6λ. Bottom: same under normal incidence—for which a strong resonance develops in the tail of the rocket.

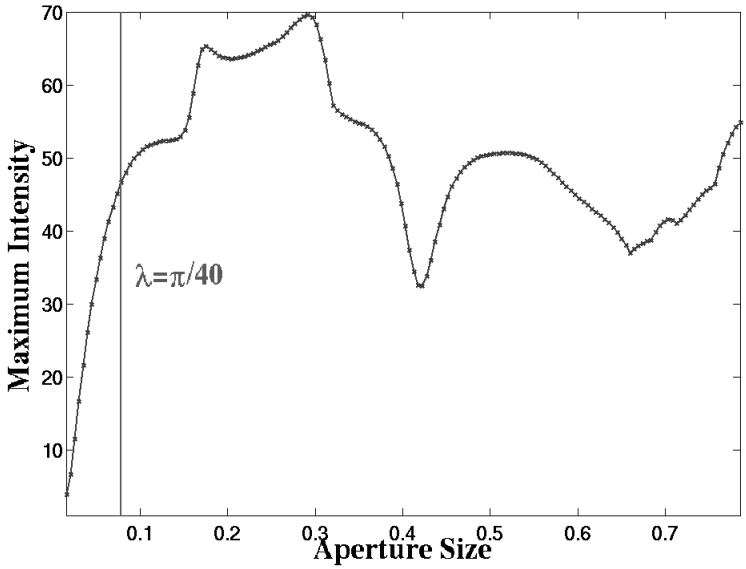

Figure 3.8: Maximum energy inside a circular cavity of size $\frac{L}{\lambda} = 80$, as a function of the aperture size. The vertical line marks the point at which the aperture is exactly equal to the wavelength.

Chapter 4

High-Order Solver for Scalar Three-Dimensional Screen Problems

This chapter presents high-order Nyström algorithms for the three-dimensional screen diffraction problem. The solvers rely on solution of the first and second-kind equations (2.4), (2.5), (2.26) and (2.27) by means of high-order quadrature rules which accurately capture the edge singularities as well as the Green's function singularities. The chapter is organized as follows: Section 4.1 provides an outline of the Nyström-based numerical framework on which the solvers are based. The next five sections describe the construction of the high-order numerical approximations we use for weighted operators: Sections 4.2 through 4.4 decompose the operators into six *canonical integral types*, while Sections 4.5 and 4.6 provide high-order integration rules for each one of the canonical operators. The selection of certain parameters required by our solvers are detailed in Section 4.7. Finally, numerical results are presented in Section 4.8 which demonstrate the properties of the integral formulations and solvers introduced in this chapter across a range of frequencies and geometries—including simulation of classical diffraction experiments such as the diffraction by a circular disc (and the observation of the Poisson spot), interference fringes resulting from diffraction across two nearby circular apertures, as well as more complex geometries consisting of multiple scatterers and cavities.

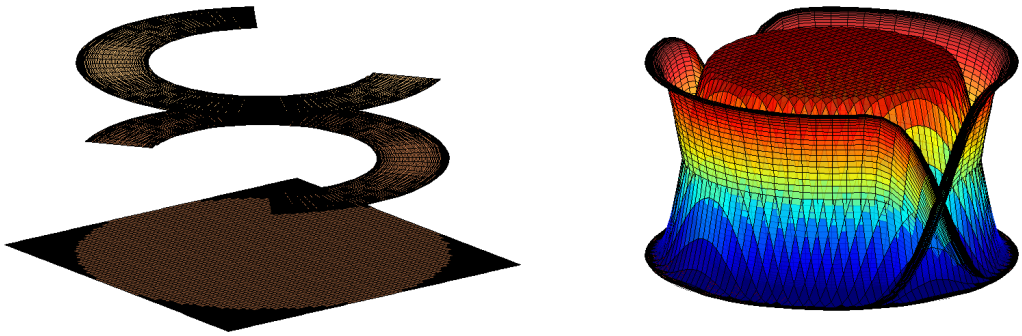

Figure 4.1: Patches, partition of unity and discretization for a disc. Left: the disc is covered by an interior patch and two edge patches. Right: partition of unity functions W_i^q supported on the patches. Notice the quadratic refinement along the edges.

4.1 Outline of the Proposed Nyström Solver

4.1.1 Basic algorithmic structure

In order to obtain numerical solutions of the surface integral equations (2.4)–(2.27) we introduce an open-surface version of the closed-surface Nyström solver put forth in [17]. This algorithm relies on

1. A discrete set of nodes $\mathcal{N} = \{\mathbf{r}_i, i = 1, \ldots, N\}$ on the surface Γ, which are used for both *integration* and *collocation*;

2. High-order integration rules which, using a given discrete set of accurate approximate values (φ_i) (respectively (ψ_i)) of a smooth surface density φ, $\varphi_i \sim \varphi(\mathbf{r}_i)$ (respectively ψ, $\psi_i \sim \psi(\mathbf{r}_i)$), produce accurate approximations of the quantities $\mathbf{S}_\omega[\varphi](\mathbf{r}_i)$ (resp. $\mathbf{N}_\omega[\psi](\mathbf{r}_i)$), see Sections 4.1.2 through 4.1.4; and

3. The iterative linear algebra solver GMRES [56], for solution of the discrete versions of equations (2.4)–(2.27) induced by the approximations mentioned in point 2.

The fact that the same set of Nyström nodes is used for integration and collocation facilitates evaluation of the composite operator $\mathbf{N}_\omega\mathbf{S}_\omega$ through simple subsequent application of the discrete versions of the operators $\mathbf{S}_\omega$ and $\mathbf{N}_\omega$.

4.1.2 Partition of unity and Nyström nodes

The integration rules mentioned in point 2 in Section 4.1.1 rely on a decomposition of a given open surface (screen) Γ as a union

$$\left(\bigcup_{q=1}^{Q_1} \mathcal{P}_1^q\right) \bigcup \left(\bigcup_{q=1}^{Q_2} \mathcal{P}_2^q\right) \tag{4.1}$$

of overlapping patches, including interior patches $\mathcal{P}_1^q$, $q = 1, \ldots, Q_1$, and edge patches $\mathcal{P}_2^q$, $q = 1, \ldots, Q_2$. For each q, the interior patch $\mathcal{P}_1^q$ (resp. edge patch $\mathcal{P}_2^q$) is assumed to be parametrized by an invertible smooth mapping $\mathbf{r}_1^q = \mathbf{r}_1^q(u, v)$, $\mathbf{r}_1^q : \quad \mathcal{H}_1^q \to \mathcal{P}_1^q$ (resp. $\mathbf{r}_2^q = \mathbf{r}_2^q(u, v)$, $\mathbf{r}_2^q : \quad \mathcal{H}_2^q \to \mathcal{P}_2^q$) defined over an open domain $\mathcal{H}_1^q \subset \mathbb{R}^2$ (resp. $\mathcal{H}_2^q \subset \mathbb{R}^2 \bigcap \{v \geq 0\}$). Note that, for the q-th edge patch, the restriction of the mapping $\mathbf{r}_2^q$ to the set $\mathcal{H}_2^q \cap \{v = 0\}$ (which we assume is non-empty for $q = 1, \ldots, Q_2$) provides a parameterization of a portion of the edge of Γ; see Figure (4.1). Following [17], further, we introduce a partition of unity (POU) subordinated to the set of overlapping patches mentioned above. In detail, the POU we use is a set of nonnegative functions W_1^q and W_2^q defined on Γ, $q = 1, \ldots, Q_1$ and $q = 1, \ldots, Q_2$, such that, for all q, W_1^q vanishes outside $\mathcal{P}_1^q$, W_2^q vanishes outside $\mathcal{P}_2^q$, and the relation

$$\sum_{q=1}^{Q_1} W_1^q + \sum_{q=1}^{Q_2} W_2^q = 1$$

holds throughout Γ. The POU can be used to decompose the integral of any function over the surface into a patch-wise sum of the form

$$\int_\Gamma f(\mathbf{r}')dS' = \sum_{j=1}^{2} \sum_{q=1}^{Q_j} \int_{\mathcal{H}_j^q} f\left(\mathbf{r}_j^q(u, v)\right) W_j^q\left(\mathbf{r}_j^q(u, v)\right) J_j^q(u, v)dudv, \tag{4.2}$$

where $J_j^q(u, v)$ denote the Jacobian associated with the parameterization $\mathbf{r}_j^q$. At this stage we define the set of Nyström nodes: introducing, for each q, a tensor-product mesh $\{(u_\ell^{q,j}, v_m^{q,j})\}$ within $\mathcal{H}_j^q$ (for $j = 1, 2$), we obtain points $\mathbf{r}_{l,m}^{q,j} = \mathbf{r}_j^q(u_\ell^{q,j}, v_m^{q,j})$ on the surface Γ. For every $j = 1, 2$ and every $q = 1, \ldots, Q_j$, the set of nodes $\mathbf{r}_{l,m}^{q,j}$ for which the POU function W_j^q associated with the patch $\mathcal{P}_j^q$ does not vanish

$$\mathcal{N}^{q,j} = \left\{\mathbf{r}_{l,m}^{q,j} \,:\, W_j^q(\mathbf{r}_{l,m}^{q,j}) > 0\right\} \tag{4.3}$$

defines the set of *Nyström nodes* on the the patch $\mathcal{P}_j^q$. The overall set $\mathcal{N}$ of Nyström nodes on the surface Γ mentioned in Section 4.1.1, is given by

$$\mathcal{N} = \bigcup_{j=1}^{2} \bigcup_{q=1}^{Q_j} \mathcal{N}^{q,j}. \tag{4.4}$$

Remark 6. *For later reference we introduce the classes of functions*

$$\mathcal{D}_1^q = \{\phi_1^q \in C^\infty(\mathcal{H}_1^q) \ : \ \mathrm{supp}(\phi_1^q) \Subset \mathcal{H}_1^q\} \ , \ q = 1, \ldots, Q_1 \ , \tag{4.5}$$

$$\mathcal{D}_2^q = \{\phi_2^q \in C^\infty(\mathcal{H}_2^q) \ : \ \mathrm{supp}(\phi_2^q) \Subset \mathcal{H}_2^q\} \ , \ q = 1, \ldots, Q_2 \ , \tag{4.6}$$

where $C^\infty(\mathcal{H}_1^q)$ denotes the set of infinitely differentiable functions defined on the open set $\mathcal{H}_1^q$, $C^\infty(\mathcal{H}_2^q)$ denotes the set of functions defined on the set $\mathcal{H}_2^q$ that are infinitely smooth on $\mathcal{H}_2^q$ up to and including the edge $\mathcal{H}_2^q \cap \{v = 0\}$, and where, for sets A and $B \subseteq \mathbb{R}^n$ the notation $A \Subset B$ indicates that the closure of A in $\mathbb{R}^n$ is a compact subset of $\mathbb{R}^n$ that is contained in B.

4.1.3 Canonical decomposition and high-order quadrature rules

The high-order numerical quadratures required by step 2. in Section 4.1.1 are obtained by applying the patch-wise decomposition (4.2) to the weighted integral operators $\mathbf{S}_\omega$ and $\mathbf{N}_\omega$ and reducing each one of them to a sum of patch-integrals which, as shown in Sections 4.2 through 4.4, can be classified into six distinct *canonical types*. For each of these canonical types we construct, in Sections 4.5 and 4.6, spectrally convergent quadrature rules on the basis of the Nyström points $\mathcal{N}^{q,j}$. Suggestions concerning selection of sizes of the edge and interior patches, which are dictated on the basis of efficiency and accuracy considerations, are put forth in Section 4.7.

4.1.4 Computational implementation and efficiency

The high-order methods presented in the following sections enable accurate and fast computation of each one of the six canonical integral types mentioned in Section 4.1.3. For added efficiency, however, our solver exploits common elements that exist between the various canonical integration algorithms, to avoid recomputation of quantities such as the trigonometric functions associated with the Green's function, partition of unity functions, integral

weights, etc. Additional efficiency could be gained by incorporating an acceleration method (see, e.g., [17] and references therein) and code parallelization.

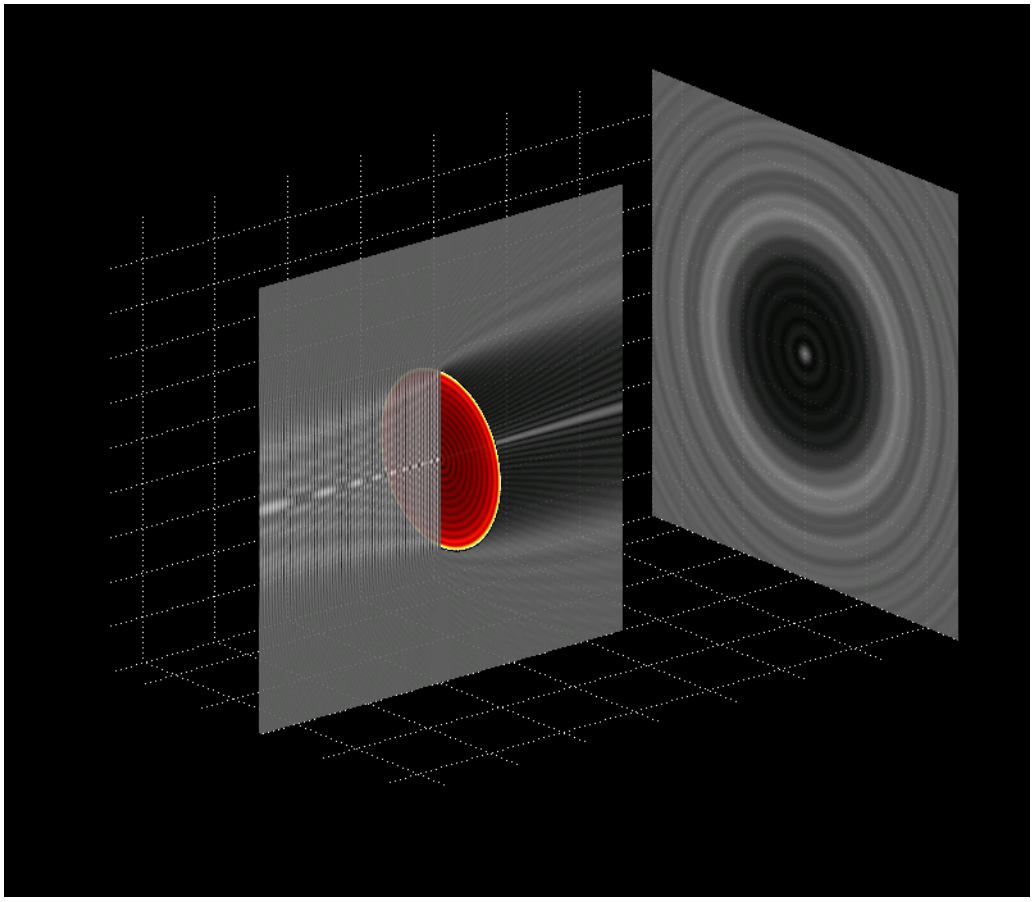

Figure 4.2: Diffraction by an infinitely thin disc: solution to the Neumann problem for a disc of diameter 24λ under normal incidence. The famous Poisson spot is clearly visible at the center of the shadow area; see also Figure 4.12. The coloring on the disc represents the values of the surface unknown ψ.

4.2 Canonical Singular-Integral Decomposition of the Operator $\mathbf{S}_\omega$

In view of equation (4.2), we express the weighted single-layer operator $\mathbf{S}_\omega$,

$$\mathbf{S}_\omega[\varphi](\mathbf{r}) = \int_\Gamma G_k(\mathbf{r},\mathbf{r}')\frac{\varphi(\mathbf{r}')}{\omega(\mathbf{r}')}dS', \tag{4.7}$$

in the form

$$\mathbf{S}_\omega = \sum_{q=1}^{Q_1} \mathcal{S}_1^q + \sum_{q=1}^{Q_2} \mathcal{S}_2^q, \tag{4.8}$$

where

$$\mathcal{S}_j^q[\varphi](\mathbf{r}) = \int_{\mathcal{H}_j^q} G_k(\mathbf{r}_j^q(u,v), \mathbf{r}) \frac{\varphi\left(\mathbf{r}_j^q(u,v)\right)}{\omega\left(\mathbf{r}_j^q(u,v)\right)} J_j^q(u,v) W_j^q(\mathbf{r}_j^q(u,v)) du dv, \quad j = 1, 2. \tag{4.9}$$

In Sections 4.2.1 and 4.2.2 the integrals (4.9) are expressed in terms of canonical integrals of various types.

4.2.1 Interior patch decomposition

For an interior patch $\mathcal{P}_1^q$ and for a point $\mathbf{r} \in \Gamma \setminus \mathcal{P}_1^q$, the integrand in (4.9) is smooth and compactly supported within the domain of integration $\mathcal{H}_1^q$—since the weight $\omega(\mathbf{r})$ is smooth and nonzero away from the edge, and since the POU function W_1^q vanishes outside $\mathcal{H}_1^q$—and, thus, the integral (4.9) gives rise to our first canonical integral type:

$$\text{Canonical Integral of Type I}$$
$$\mathcal{I}_1^{q,reg}[\phi_1] = \int_{\mathcal{H}_1^q} \phi_1(u,v) du dv \quad , \quad \phi_1 \in \mathcal{D}_1^q \,, \tag{4.10}$$

see Remark 6. For a point $\mathbf{r} \in \mathcal{P}_1^q$, $\mathbf{r} = \mathbf{r}_1^q(u_0, v_0)$ for some $(u_0, v_0) \in \mathcal{H}_1^q$, on the other hand, the integrand of (4.9) with $j = 1$ has an integrable singularity at the point (u_0, v_0) (cf. equation (1.10)). Following [17] we express the kernel as a sum of a localized singular part, and a smooth remainder, $G_k = G_k^{sing} + G_k^{reg}$, where

$$G_k^{sing} = \eta_{\mathbf{r}} G_k^{re}, \quad G_k^{reg} = (1 - \eta_{\mathbf{r}}) G_k^{re} + i G_k^{im}. \tag{4.11}$$

Here, $G_k^{re}(\mathbf{r}, \mathbf{r}') = \frac{\cos(k|\mathbf{r}-\mathbf{r}'|)}{|\mathbf{r}-\mathbf{r}'|}$ and $G_k^{im}(\mathbf{r}, \mathbf{r}') = \frac{\sin(k|\mathbf{r}-\mathbf{r}'|)}{|\mathbf{r}-\mathbf{r}'|}$ denote the real and imaginary parts of the kernel $G_k(\mathbf{r}, \mathbf{r}')$, respectively, and $\eta_{\mathbf{r}}$ is a smooth function which vanishes outside a neighborhood of the point $\mathbf{r}$. As in the previous reference, the collection of all pairs $(\eta_{\mathbf{r}}, 1 - \eta_{\mathbf{r}})$ for $\mathbf{r} \in \Gamma$ is called a *floating partition of unity*. The integral that arises as G_k is replaced in (4.9) by G_k^{reg}, has a smooth integrand which is compactly supported within $\mathcal{H}_1^q$; clearly, this is an integral of canonical type I. The integral obtained by substituting G_k

by G_k^{sing}, on the other hand, gives rise to our second canonical type

$$\text{Canonical Integral of Type II}$$
$$\mathcal{I}_1^{q,sing}[\phi_1](u_0,v_0) = \int_{\mathcal{H}_1^q} \frac{\phi_1(u,v)}{|\mathbf{R}|} dudv, \quad \phi_1 \in \mathcal{D}_1^q \tag{4.12}$$

where for the sake of conciseness, we have set $\mathbf{R} = \mathbf{r}_1^q(u_0,v_0) - \mathbf{r}_1^q(u,v)$ and where the point (u_0,v_0) belongs to $\mathcal{H}_1^q$,

4.2.2 Edge-patch decomposition

The edge singularity on an edge patch $\mathcal{P}_2^q$ is characterized in terms of asymptotic form (2.1). In what follows we assume, as we may, that on each edge patch,the weight ω is given by an expression of the form

$$\omega(\mathbf{r}_2^q(u,v)) = \omega_2^q(u,v)\sqrt{v}, \tag{4.13}$$

where the function $\omega_2^q(u,v)$ is *smooth up to the edge and it does not vanish anywhere along the edge*. It follows that for an edge patch $\mathcal{P}_2^q$ and for a point $\mathbf{r} \in \Gamma \setminus \mathcal{P}_2^q$, the operator $\mathcal{S}_2^q$ defined in equation (4.9) for $j = 2$ takes the form of an integral of our third canonical type:

$$\text{Canonical Integral of Type III}$$
$$\mathcal{I}_2^{q,reg}[\phi_2](u_0,v_0) = \int_{\mathcal{H}_2^q} \phi_2(u,v) \frac{dudv}{\sqrt{v}}, \quad \phi_2 \in \mathcal{D}_2^q. \tag{4.14}$$

Finally, for an edge patch $\mathcal{P}_2^q$ and for a point $\mathbf{r} \in \mathcal{P}_2^q$ we once again use the floating partition of unity to decompose the Green function as a sum of a singular and a regular term. The regular term results in a canonical integral of Type III, and the singular term gives rise to our fourth canonical type:

$$\text{Canonical Integral of Type IV}$$
$$\mathcal{I}_2^{q,sing}[\phi_2] = \int_{\mathcal{H}_2^q} \frac{\phi_2(u,v)}{|\mathbf{R}|} \frac{dudv}{\sqrt{v}}, \quad \phi_2 \in \mathcal{D}_2^q \tag{4.15}$$

where $\mathbf{R} = \mathbf{r}_2^q(u_0,v_0) - \mathbf{r}_2^q(u,v)$.

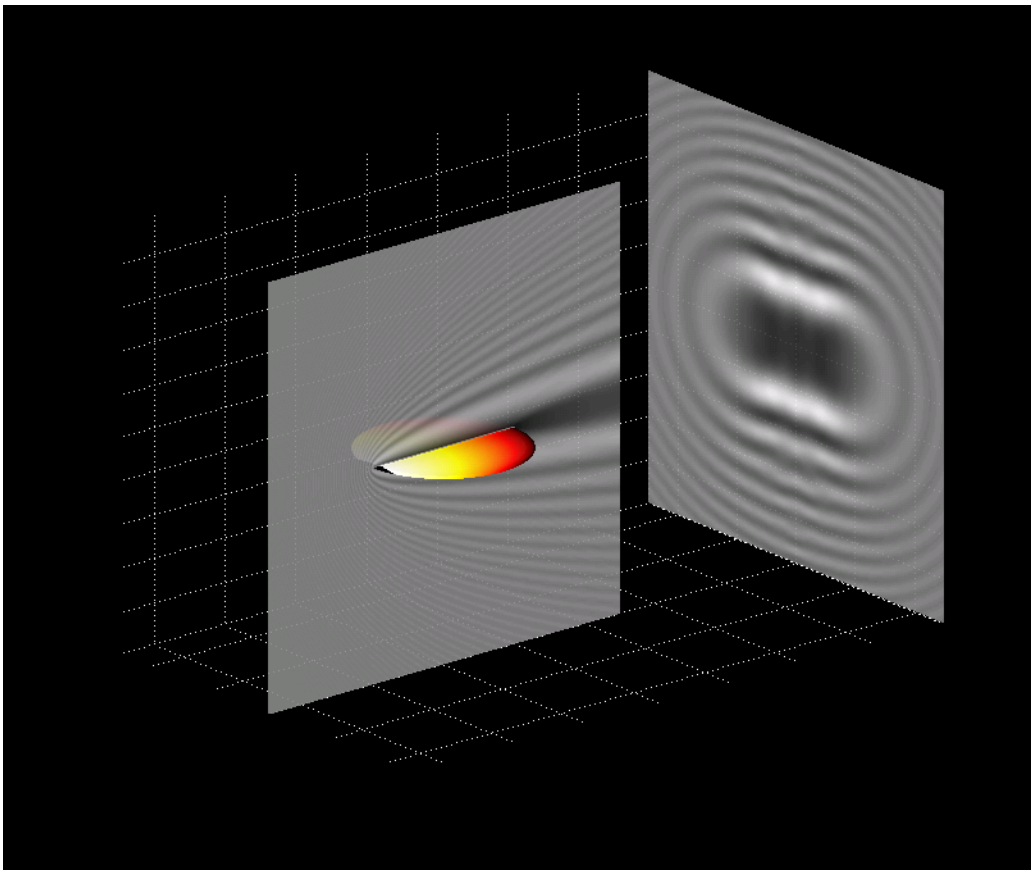

Figure 4.3: Diffraction by an infinitely thin disc: solution to the Dirichlet problem for a disc of diameter 24λ under incidence parallel to the disc. The coloring on the disc represents the values of the surface unknown φ.

4.3 Canonical Decomposition of the Operator $\mathbf{N}_\omega$

In view of equations (1.35) and (2.2) the operator $\mathbf{N}_\omega$ is given by the point-wise limit

$$\mathbf{N}_\omega[\psi](\mathbf{r}) \equiv \lim_{z\to 0} \frac{\partial}{\partial \mathbf{n}_\mathbf{r}} \int_\Gamma \frac{\partial G_k(\mathbf{r}, \mathbf{r}' + z\mathbf{n}_{\mathbf{r}'})}{\partial \mathbf{n}'_\mathbf{r}} \psi(\mathbf{r}')\omega(\mathbf{r}')dS', \qquad \mathbf{r} \in \Gamma. \tag{4.16}$$

Following the open-arc derivation [24, 49] (see also Chapter 3) we obtain an adequate expression for this "hypersingular operator" by taking advantage of the following lemma.

Lemma 15. *The operator* $\mathbf{N}_\omega$ *can be expressed in the form*

$$\mathbf{N}_\omega = \mathbf{N}^g_\omega + \mathbf{N}^{pv}_\omega \mathcal{T}_\omega \tag{4.17}$$

where, denoting the surface gradient with respect to $\mathbf{r}'$ *by* $\nabla^s_{\mathbf{r}'}$ *and letting* $[\,\cdot\,,\cdot\,]$ *denote the*

vector product, the operators $\mathbf{N}_\omega^g$, $\mathbf{N}_\omega^{pv}$ *and* $\mathcal{T}_\omega$ *are given by*

$$\mathbf{N}_\omega^g[\psi](\mathbf{r}) = k^2 \int_\Gamma G_k(\mathbf{r},\mathbf{r}')\psi(\mathbf{r}')\omega(\mathbf{r}')\boldsymbol{n}_{\mathbf{r}'}.\boldsymbol{n}_{\mathbf{r}} dS', \tag{4.18}$$

$$\mathcal{T}_\omega[\psi](\mathbf{r}') = \omega^2(\mathbf{r}')\nabla_{\mathbf{r}'}^s[\psi](\mathbf{r}') + \frac{\psi(\mathbf{r}')}{2}\nabla_{\mathbf{r}'}^s[\omega^2](\mathbf{r}'), \quad \textit{and} \tag{4.19}$$

$$\mathbf{N}_\omega^{pv}[\mathbf{T}](\mathbf{r}) = p.v. \int_\Gamma \left[\nabla_{\mathbf{r}} G_k(\mathbf{r},\mathbf{r}'), \left[\boldsymbol{n}_{\mathbf{r}'}, \mathbf{T}(\mathbf{r}')\right]\right] \cdot \boldsymbol{n}_{\mathbf{r}} \frac{dS'}{\omega(\mathbf{r}')}. \tag{4.20}$$

Proof. See Appendix 4.9.1. □

As shown in Sections 4.3.1 through 4.3.3, we may evaluate $\mathbf{N}_\omega$ by relying on Lemma 15 and using quadratures for various types of canonical integrals.

4.3.1 Canonical decomposition of the operator $\mathbf{N}_\omega^g$ (equation (4.18))

Calling $\psi_2 = \psi\omega^2$ we re-express (4.18) in the form

$$\mathbf{N}_\omega^g[\psi](\mathbf{r}) = k^2 \int_\Gamma G_k(\mathbf{r},\mathbf{r}') \frac{(\psi_2(\mathbf{r}')\mathbf{n}_{\mathbf{r}'}.\mathbf{n}_{\mathbf{r}})}{\omega(\mathbf{r}')} dS'. \tag{4.21}$$

Since $\omega^2(\mathbf{r})$ is a smooth function of $\mathbf{r}$ throughout Γ, a construction similar to the one used for (4.7) yields a decomposition of the operator $\mathbf{N}_\omega^s$ in terms of canonical integrals of types I-IV; see Section 4.2.

4.3.2 Canonical decomposition of the operator $\mathcal{T}_\omega$ (equation (4.19))

Making use once again of the POU introduced in Section 4.1.2, we obtain the decomposition

$$\nabla_{\mathbf{r}}^s[\psi](\mathbf{r}) = \sum_{q=1}^{Q_1} \nabla_{\mathbf{r}}^s[\psi W_1^q](\mathbf{r}) + \sum_{q=1}^{Q_2} \nabla_{\mathbf{r}}^s[\psi W_2^q](\mathbf{r}),$$

of the surface gradient. The evaluation of the q-th term in each one of these sums requires the calculation of partial derivatives of the form

$$\frac{\partial \phi_1(u,v)}{\partial u} \quad , \quad \frac{\partial \phi_1(u,v)}{\partial v} \ , \tag{4.22}$$

$$\frac{\partial \phi_2(u,v)}{\partial u} \quad \text{and} \quad \frac{\partial \phi_2(u,v)}{\partial v} \tag{4.23}$$

for functions $\phi_1 \in \mathcal{D}_1^q$ and $\phi_2 \in \mathcal{D}_2^q$. These partial derivatives can be evaluated efficiently and with high-order accuracy by means of the differentiation methods introduced in Sections 4.5 and 4.6 below. In view of equation (4.19), use of such high-order rules enables high-order evaluation of the operator $\mathcal{T}_\omega[\psi](\mathbf{r})$.

4.3.3 Canonical decomposition of the operator $\mathbf{N}_\omega^{pv}$ (equation (4.20))

It is easy to check that, for smooth $\mathbf{T}$, $\mathbf{N}_\omega^{pv}[\mathbf{T}]$ can be evaluated as a linear combination of functions of the form $\mathbf{D}_\omega^{\mathbf{V}_\ell}[\phi_\ell]$, where $\mathbf{V}_\ell$ is a vector quantity that varies with $\mathbf{r}$ but is independent of $\mathbf{r}'$, where the operator $\mathbf{D}_\omega^{\mathbf{V}}$ is defined by

$$\mathbf{D}_\omega^{\mathbf{V}}[\psi](\mathbf{r}) = \text{p.v.} \int_\Gamma \left\{ \nabla_{\mathbf{r}} G_k(\mathbf{r}, \mathbf{r}') \cdot \mathbf{V} \right\} \frac{\psi(\mathbf{r}')}{\omega(\mathbf{r}')} dS', \tag{4.24}$$

and where ϕ_ℓ are smooth functions. Applying the decomposition (4.2) to the operator defined in equation (4.24) yields

$$\mathbf{D}_\omega^{\mathbf{V}}[\psi] = \sum_{q=1}^{Q_1} \mathbf{D}_1^{\mathbf{V},q}[\psi](\mathbf{r}) + \sum_{q=1}^{Q_2} \mathbf{D}_2^{\mathbf{V},q}[\psi](\mathbf{r}), \tag{4.25}$$

where

$$\mathbf{D}_j^{\mathbf{V},q}[\psi](\mathbf{r}) = \text{p.v.} \int_{\mathcal{H}_j^q} \left\{ \nabla_{\mathbf{r}} G_k(\mathbf{r}, \mathbf{r}_j^q(u,v)) \cdot \mathbf{V} \right\} \frac{\psi(\mathbf{r}_j^q(u,v))}{\omega(\mathbf{r}_j^q(u,v))} W_j^q(\mathbf{r}_j^q(u,v)) J_j^q(u,v) du dv. \tag{4.26}$$

We can express the operator $\mathbf{D}_j^{\mathbf{V},q}$ as the sum of a hypersingular operator and a weakly singular operator whose respective kernels are defined by the split

$$\nabla_{\mathbf{r}} G_k(\mathbf{r}, \mathbf{r}') \cdot \mathbf{V} = G_k^{pv} + G_k^{ws}, \quad G_k^{pv} = -\frac{(\mathbf{r} - \mathbf{r}') \cdot \mathbf{V}}{|\mathbf{r} - \mathbf{r}'|^3}, \tag{4.27}$$

where the residual kernel G_k^{ws} equals a sum of functions which are either smooth or weakly singular with singularity $\frac{1}{|\mathbf{r}-\mathbf{r}'|}$. Using the partition-of-unity split embodied in equation (4.2), the operator with kernel G_k^{ws} can be expressed in terms of integrals of canonical types I-IV. The hypersingular operator with kernel G_k^{pv} on the other hand gives rise to our fifth and

sixth canonical types:

$$\text{Canonical Integral of Type V}$$
$$\mathcal{I}_1^{q,pv}[\phi_1](u_0,v_0) = \text{p.v.} \int_{\mathcal{H}_1^q} \frac{\mathbf{R}\cdot\mathbf{V}}{|\mathbf{R}|^3}\phi_1(u,v)dudv. \tag{4.28}$$

$$\text{Canonical Integral of Type VI}$$
$$\mathcal{I}_2^{q,pv}[\phi_2](u_0,v_0) = \text{p.v.} \int_{\mathcal{H}_2^q} \frac{\mathbf{R}\cdot\mathbf{V}}{|\mathbf{R}|^3}\phi_2(u,v)\frac{dudv}{\sqrt{v}}. \tag{4.29}$$

4.4 Canonical Decomposition of the Composite Operator $\mathbf{N}_\omega\mathbf{S}_\omega$

While the action of the composite operator $\mathbf{N}_\omega\mathbf{S}_\omega$ on a function ϕ can be evaluated by producing first $\psi = \mathbf{S}_\omega[\phi]$ and then evaluating $\mathbf{N}_\omega[\psi]$, both of which can be obtained by the methods described in the previous sections, we have found it advantageous in practice to proceed differently, on the basis of the expression (4.17); see Remark 10 for more details. Using the decomposition (4.17), we first evaluate the term $\mathbf{N}_\omega^g\mathbf{S}_\omega[\phi]$ by means of a direct composition: we compute $\mathbf{S}_\omega[\phi]$ and then apply $\mathbf{N}_\omega^g$ to the result using the decompositions put forth in Sections 4.2 and 4.3.1, respectively. To evaluate the second term $\mathbf{N}_\omega^{pv}\mathbf{S}_\omega[\phi]$, on the other hand, we first evaluate the quantity $\mathcal{T}_\omega\mathbf{S}_\omega[\phi]$ by expressing the surface gradient of $\mathbf{S}_\omega[\phi]$ required by equation (4.19) as

$$\nabla_{\mathbf{r}}^s S_\omega[\phi](\mathbf{r}) = p.v. \int_\Gamma \nabla_{\mathbf{r}}^s G_k(\mathbf{r},\mathbf{r}')\frac{\phi(\mathbf{r}')}{\omega(\mathbf{r}')}dS' = \sum_{\ell=1,2} \mathbf{D}_\omega^{\tau_\ell(\mathbf{r})}[\phi](\mathbf{r}), \tag{4.30}$$

where $\tau_1(\mathbf{r})$ and $\tau_2(\mathbf{r})$ denote two orthogonal tangent vectors to Γ at the point $\mathbf{r}$ which vary smoothly with $\mathbf{r}$; the corresponding surface gradient of ω^2 can be obtained by direct differentiation of a closed-form expression, if available, or by means of the differentiation methods put forth in this chapter. The terms in the sum on the right-hand side of (4.30) are of the form given in equation (4.24) with $\mathbf{V} = \tau_\ell(\mathbf{r})$ ($\ell = 1, 2$), and thus can be expressed in terms of the canonical integrals of type I-VI, as outlined in Section 4.3.3.

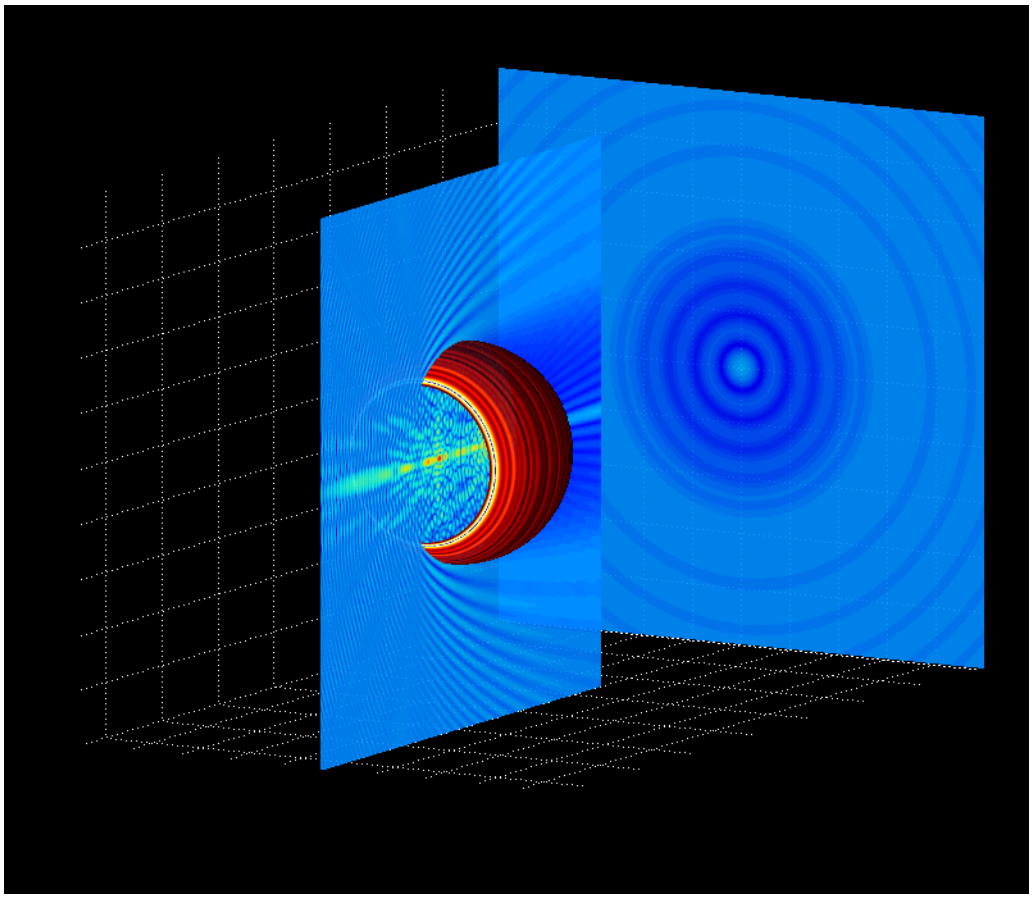

Figure 4.4: Neumann problem on a spherical cavity of diameter 18λ. The coloring on the spherical wall represents the values of the surface unknown ψ.

.

4.5 High-Order Evaluation of Interior-Patch Operators

In this section we describe our algorithms for evaluation of the interior-patch operators introduced in the previous sections, namely the integral operators of type I, II and V and the differentiation operator (4.22). To do this, and in accordance with Section 4.1.2, we assume the nodes $(u_\ell^{q,1}, v_m^{q,1})$ $(u_\ell^{q,1} = u_0^{q,1} + \ell h_u^{q,1},\ v_m^{q,1} = v_0^{q,1} + m h_v^{q,1},\ \ell = 1, \dots L_q^1,$ $m = 1 \dots M_q^1)$, discretize a rectangle that contains $\mathcal{H}_1^q$.

4.5.1 Type I integral (regular)

We evaluate the canonical Type I integral defined in equation (4.10) by means of a simple trapezoidal sum over the grid: as noted in [17] the periodicity (ϕ_1 is compactly supported) and smoothness of the integrand gives rise to super-algebraic convergence in this case.

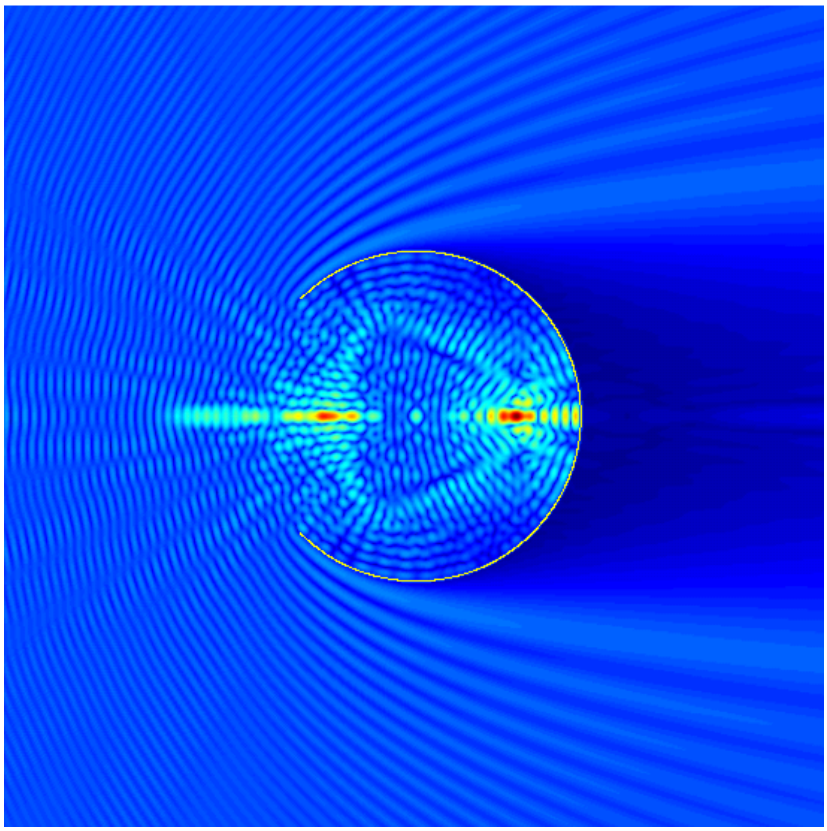

Figure 4.5: Total field inside a spherical cavity of diameter 18λ, Dirichlet problem.

.

4.5.2 Partial derivatives

In view of the smoothness and periodicity of the function ϕ_1, a standard two-dimensional FFT-based interpolation scheme based on the evenly spaced grid values $\phi_1^{\ell,m}$ yields spectrally convergent approximations of the function $\phi_1(u,v)$ and its derivatives; our algorithm thus evaluates the derivatives required in equation (4.22) by performing a direct term-by-term differentiation of the resulting Fourier representation.

4.5.3 Type II integral (singular)

In order to resolve the singular integrand in equation (4.12) we utilize the polar change of variables introduced in [17]. Defining $u(\rho,\theta) = u_0 + \rho\cos\theta$ and $v(\rho,\theta) = v_0 + \rho\sin\theta$, we obtain

$$\mathcal{I}_1^{q,sing}[\phi_1](u_0,v_0) = \int_0^{\pi} I_{\rho,1}^{q}[\phi_1](u_0,v_0,\theta)d\theta \tag{4.31}$$

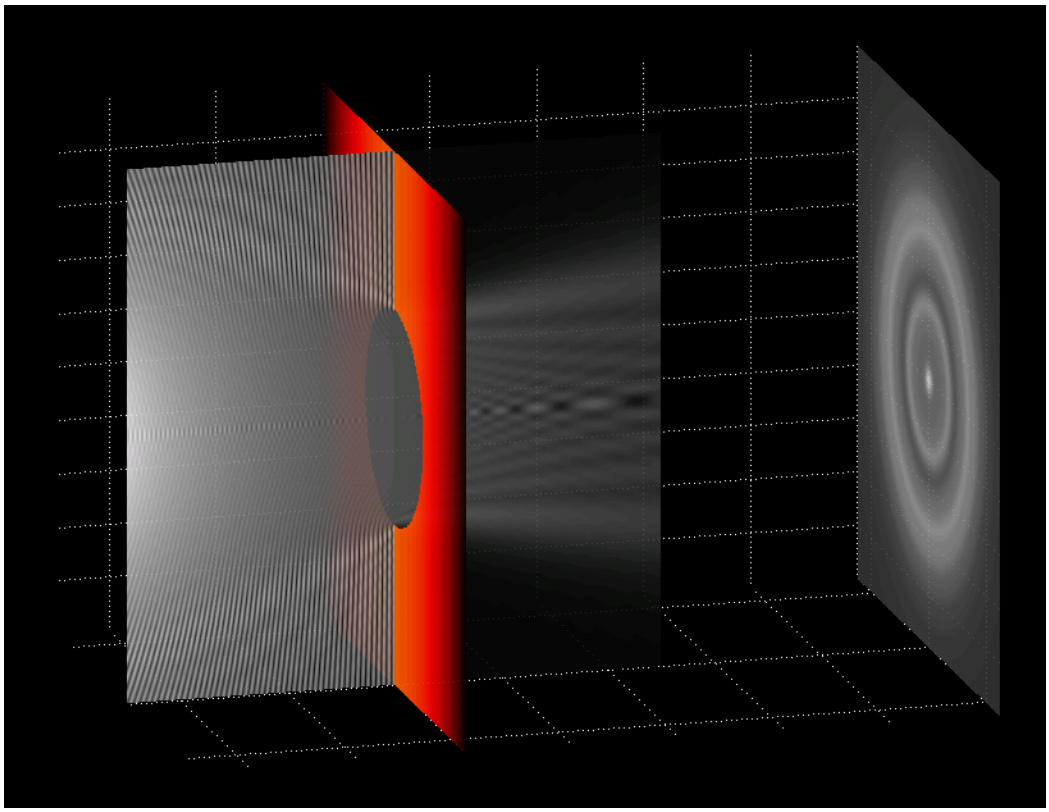

Figure 4.6: Diffraction by a circular aperture: solution to the Neumann problem for an aperture of diameter 24λ under point source illumination. The source, which is not visible here, is located to the left of the displayed area. The coloring on the plane is introduced for visual quality, and it does not represent any physical quantity.

with

$$I^q_{\rho,1}[\phi_1](u_0, v_0, \theta) = \int_{-\infty}^{\infty} \phi_1^\rho(\rho, \theta) |\frac{|\rho|}{R} d\rho, \tag{4.32}$$

where

$$R = |\mathbf{r}_1^q(u_0, v_0) - \mathbf{r}_1^q\left(u(\rho, \theta), v(\rho, \theta)\right)|, \tag{4.33}$$

and where

$$\phi_1^\rho(\rho, \theta) = \phi_1(u_0 + \rho\cos\theta, v_0 + \rho\sin\theta) \tag{4.34}$$

is a smooth function of ρ and θ which vanishes for sufficiently large values of ρ. Since, as noted in [17], the ratio $\frac{|\rho|}{R}$ is a smooth function of ρ, the integral $I^q_{\rho,1}[\phi_1](\theta, u_0, v_0)$ defined in (4.32) can be computed accurately via the trapezoidal rule with respect to ρ for any value of θ. Similarly, applying the trapezoidal rule in the θ variable gives rise to high-order convergence of the integral (4.31), in view of the π-periodicity of the integrand.

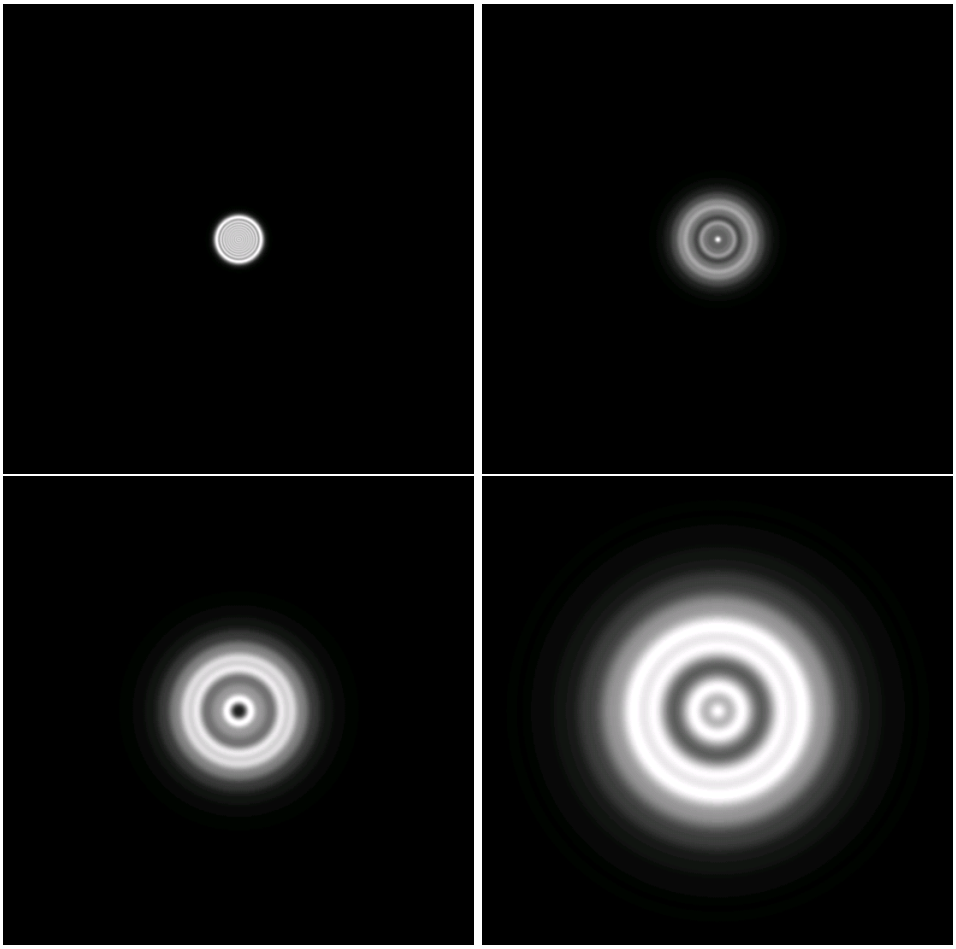

Figure 4.7: Field diffracted by the circular aperture configuration depicted in Figure 4.6. From top left to bottom right, depiction of the diffracted field at observation screens located at distances of 6λ, 60λ, 120λ and 240λ behind the punctured plane. A dark-spot (the Poisson shadow) can be observed at the center of the illuminated area in the bottom-left image.

.

Remark 7. *Our application of the trapezoidal rule for evaluation of* $I^q_{\rho,1}(\theta, u_0, v_0)$ *requires use of equidistant samples in the* ρ *variable, which for most values of* θ*, do not correspond to any of the original grid nodes* $(u^{q,1}_\ell, v^{q,1}_m)$*. To address this issue our solver relies on the FFT/cubic-spline interpolation technique presented in [17, Section 3], which allows for fast and efficient evaluation of the required equidistant* ρ *samples.*

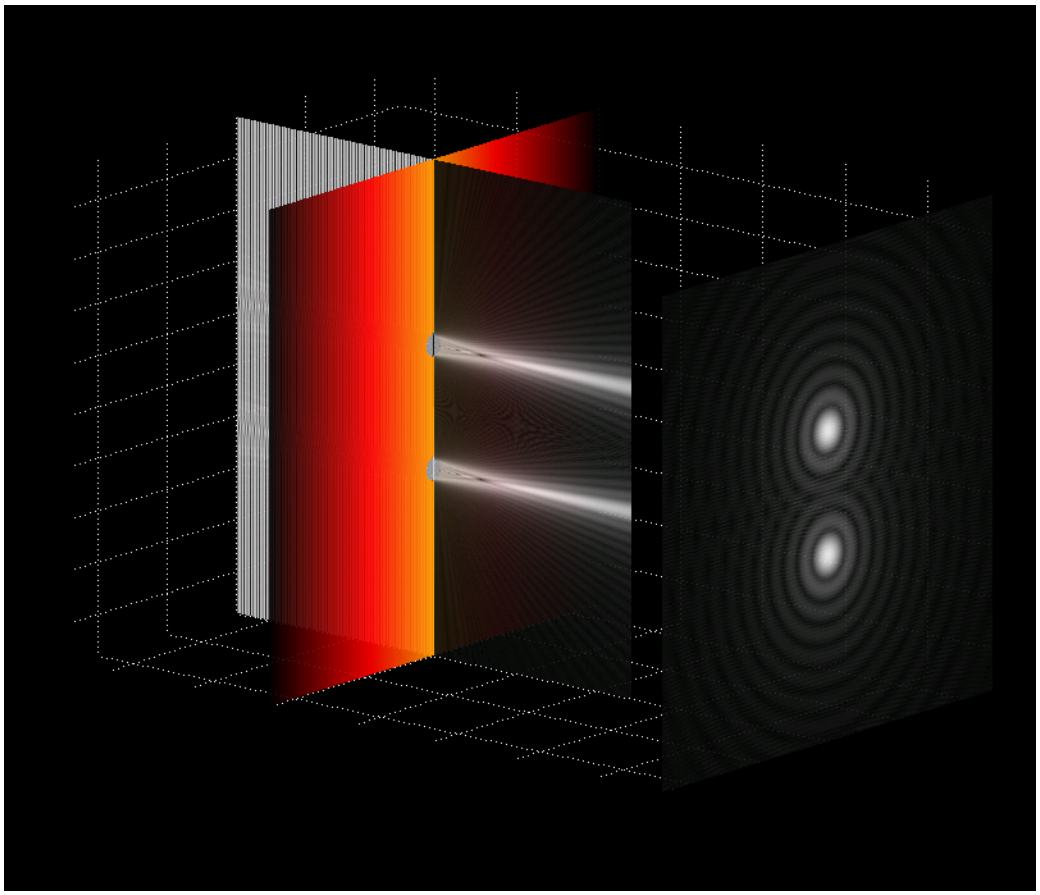

Figure 4.8: Simulation of Young's experiment: diffraction by two circular apertures in a sound-hard plane (Neumann boundary conditions); the apertures are 24 wavelengths in diameter. The coloring on the plane is introduced for visual quality, and does not represent any physical quantity.

4.5.4 Type V integral (principal value)

An application of the polar change of variables mentioned in Section 4.5.3 to the principal-value Type V integral (4.28) results in the expression

$$\mathcal{I}_1^{q,pv}[\phi_1](u_0, v_0) = \int_0^\pi I_{\rho,1}^{q,pv}[\phi_1](u_0, v_0, \theta)d\theta, \tag{4.35}$$

where $I_{\rho,1}^{q,pv}[\phi_1](u_0, v_0, \theta)$ is given by the principal value integral

$$I_{\rho,1}^{q,pv}[\phi_1](u_0, v_0, \theta) = p.v. \int_{-\infty}^{\infty} \frac{|\rho|\mathbf{R}\cdot\mathbf{V}}{R^3}\phi_1^\rho(\rho, \theta)d\rho. \tag{4.36}$$

Here the function $\phi_1^\rho(\rho, \theta)$ is defined by equation (4.34) and we have set $\mathbf{R} = \mathbf{r}_1^q(u_0, v_0) - \mathbf{r}_1^q(u(\rho, \theta), v(\rho, \theta))$. Equations (4.35) and (4.36) form the basis of our algorithm for evalua-

tion of Type V integrals.

Since both $\frac{|\rho|^3}{R^3}$ and $\frac{\mathbf{R}\cdot\mathbf{V}}{\rho}$ are smooth functions of ρ and θ, it is useful to consider the expression

$$I^{q,pv}_{\rho,1}(u^q_0, v^q_0, \theta) = p.v. \int_{-\infty}^{\infty} \frac{|\rho|^3}{R^3} \frac{\mathbf{R}\cdot\mathbf{V}}{\rho} \frac{\phi^\rho_1(\rho,\theta)}{\rho} d\rho, \tag{4.37}$$

for the integral (4.36). This is a one-dimensional principal value integral of the form

$$I = \text{p.v.} \int_{-\infty}^{\infty} \frac{v(x)}{x} dx, \tag{4.38}$$

where v is a compactly supported smooth function. Our algorithm proceeds by evaluating this principal value integral by means of a trapezoidal rule algorithm with integration nodes centered symmetrically around $x = 0$—which, as shown in [67], yields spectral accuracy for smooth and periodic functions. In detail, letting $x_i = (i + \frac{1}{2})/M$, after appropriate scaling into the interval $[-1, 1]$, our quadrature for the integral (4.38) is given by

$$\text{p.v.} \int_{-1}^{1} \frac{v(x)}{x} dx \sim \frac{1}{M} \sum_{i=-M}^{M-1} \frac{v(x_i)}{x_i}. \tag{4.39}$$

This expression provides spectrally accuracy as long as v is a smooth function of periodicity 2. Our Type-V integration algorithm is completed by trapezoidal integration in the θ variable to produce the integral (4.35) with spectral accuracy.

Remark 8. *Application of the trapezoidal rule* (4.39) *to compute the integral* (4.37) *requires evenly spaced samples in the ρ variable, which, in addition, must also be symmetrically centered around $\rho = 0$. To obtain such samples our algorithm proceeds in two steps: 1) It uses the one-dimensional FFT/spline interpolation method presented in [17, Section 3] to produce evenly spaced samples of the integrand in the ρ variable, and 2) It applies an FFT-based shift (see Remark 9) to produce interpolated samples centered around $\rho = 0$. In view of the periodicity and smoothness of the function v, this procedure is highly accurate, and, it is, in fact significantly faster and less memory intensive than the full two-dimensional spline-table construction presented in [67]—since it only requires storage of one-dimensional tables.*

Remark 9. *Given point values $v(x_i)$ of a smooth and periodic function v on an equispaced grid $x_i = x_0 + ih$, samples of v on a new shifted grid $x^*_i = x_i + \delta$ can be obtained*

efficiently and with spectral accuracy through use of FFTs. The algorithm proceeds as follows: 1) Evaluation of the FFT of the data set $v(x_i)$ to produce Fourier coefficients of $v(x)$, 2) Multiplication of each Fourier coefficient by an appropriate exponential, to produce the Fourier coefficients of the shifted function $v(x + \delta)$, and 3) Evaluation of the inverse FFT of the coefficients produced per point 2).

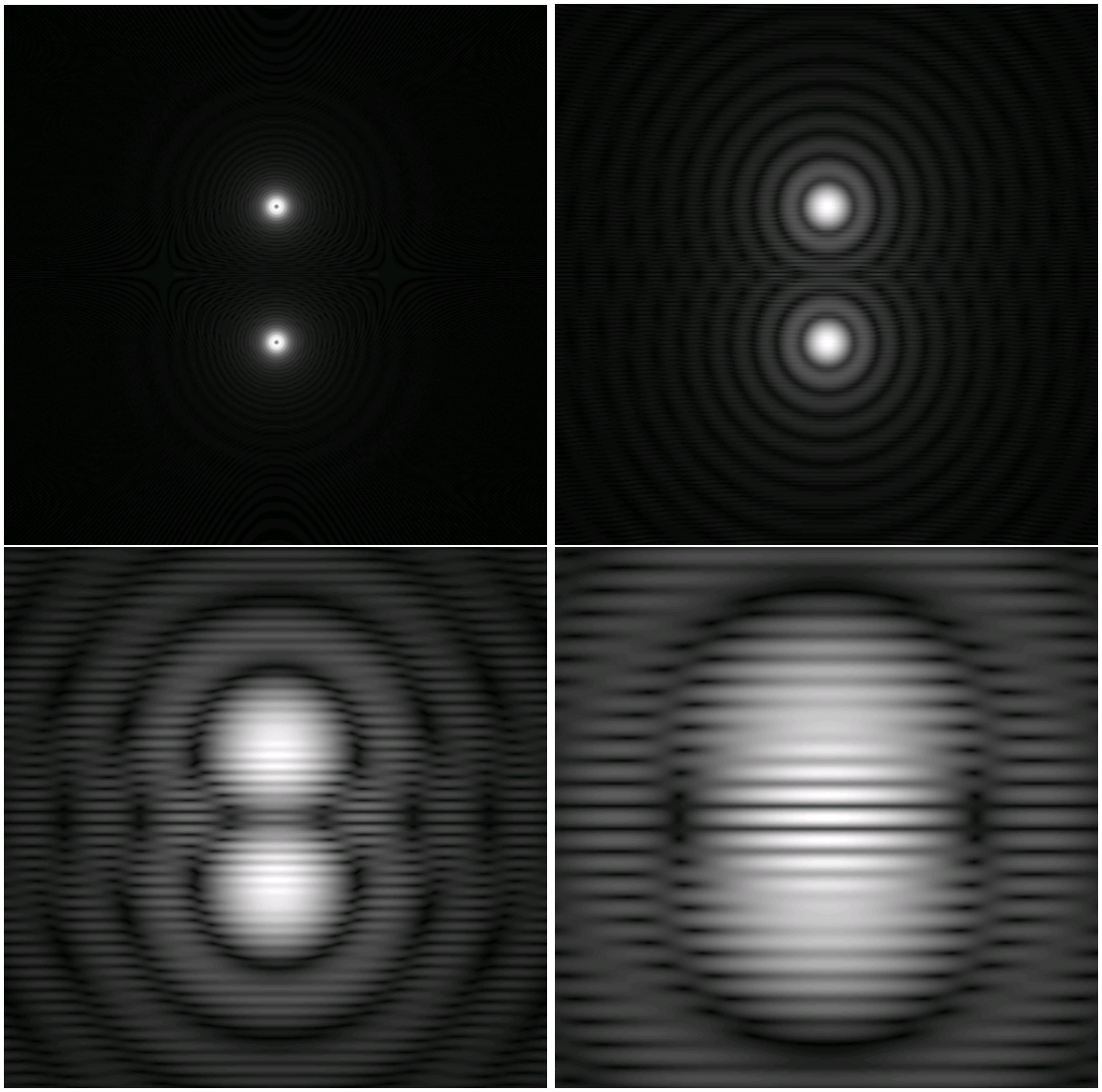

Figure 4.9: Field diffracted by the two-hole configuration depicted in Figure 4.8. From left to right, depiction of the diffracted field at observation screens located at distances of 72λ, 576λ, 1728λ and 3456λ behind the punctured plane. As in Figure 4.7, a dark spot can be viewed at the center of the illuminated circles in the upper-left image.

.

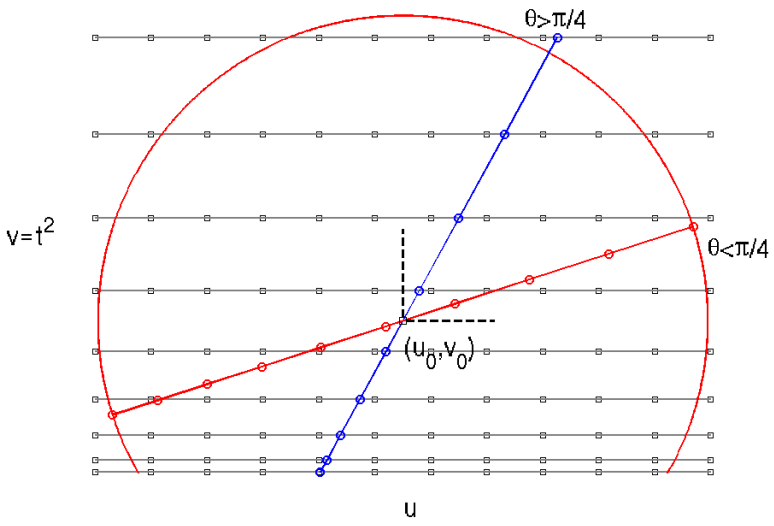

Figure 4.10: Polar changes of variables around a point close to the edge: quadratic sampling in the v variable, requiring off-grid interpolations for grazing angles.

4.6 High-Order Evaluation of Edge-Patch Operators

In this section we describe our algorithms for evaluation of the edge-patch operators, namely the integral operators of type III, IV and VI and the differentiation operator (4.23). To do this, and in accordance with Section 4.1.2, we select a tensor product grid $(u_\ell^{q,2}, v_m^{q,2})$ quadratically refined in v, which, using spatial mesh-sizes $h_u^{q,2}$ and $h_t^{q,2}$ in the u and t variables, is given by

$$\begin{cases} u_\ell^{q,2} = u_0^{q,2} + \ell h_u^{q,2}, & \ell = 1, \dots L_q^2 \\ v_m^{q,2} = \left((\frac{1}{2} + m) h_t^{q,2}\right)^2, & m = 1 \dots M_q^2. \end{cases} \tag{4.40}$$

This grid is assumed to discretize a rectangle that contains $\mathcal{H}_2^q$; in view of the assumptions made on this set (Section 4.1.2) and the form of the discretization $(u_\ell^{q,2}, v_m^{q,2})$ we see that, while the edge $v = 0$ is not itself sampled by this discretization, a parallel line to it, at a distance of $(h_t^{q,2}/2)^2$ in (u, v) space, is.

4.6.1 Type III integral (regular)

For any smooth function g defined over the interval $[0, 1]$ which vanishes identically with all its derivatives at $x = 1$, the function $g(t^2)$ can clearly be extended as a smooth and periodic

function of period 2. It follows immediately from the identity

$$\int_0^1 \frac{g(x)}{\sqrt{x}}dx = \int_{-1}^1 g(t^2)dt = 2\int_0^1 g(t^2)dt \tag{4.41}$$

that the trapezoidal rule approximation

$$\int_0^1 \frac{g(x)}{\sqrt{x}}dx \sim \frac{2}{M}\sum_{m=1}^{M} g\left(t_m^2\right), \quad t_m = \frac{2m+1}{2M}, i = 0, \ldots, M-1 \tag{4.42}$$

gives rise to super-algebraic convergence. Since the patch discretization $(u_\ell^{q,2}, v_m^{q,2})$ can be expressed in the form $v_m^{q,2} = (t_m^{q,2})^2$, where $t_m^{q,2} = (\frac{1}{2}+m)h_t^{q,2}$, a two-dimensional trapezoidal rule using this mesh in the set $\mathcal{H}_2^q$ is super-algebraically convergent.

4.6.2 Partial derivatives

In view of the smoothness and periodicity of the function $\phi_2(u, t^2)$, a two-dimensional interpolation scheme based on use of FFTs along the u variable and FCTs (Fast Cosine Transform) along the t variable yields spectrally convergent approximations of the function $\phi_2(u, t^2)$ and its derivatives. Our algorithm thus evaluates the derivatives required in equation (4.23) by performing a direct term by term differentiation of the resulting Fourier representations together with the expression

$$\frac{\partial\phi_2(u,t^2)}{\partial v} = \frac{1}{2t}\frac{\partial}{\partial t}\left[\phi_2(u,t^2)\right]. \tag{4.43}$$

Remark 10. *In view of the presence of the $t = \sqrt{v}$ denominator on the right-hand side of equation* (4.43)*, evaluation of partial derivatives of the function $\phi_2(u, v)$ with respect to v on the basis of a term by term differentiation of cosine expansion of the function $\phi_2(u, t^2)$, while yielding spectrally accurate results, is less accurate near the edge than away from the edge—in close analogy with the well-known relative loss of accuracy around end points in Chebyshev-based numerical differentiation. This is why our algorithm was designed to evaluate the composite operator $\mathbf{N}_\omega\mathbf{S}_\omega$ by first producing the combination $\mathcal{T}_\omega\mathbf{S}_\omega$ via the rules derived for $D_\omega^{\mathbf{T}}$ as explained in Section 4.4, thus avoiding numerical differentiation. Unfortunately, in the evaluation of the operator $\mathbf{N}_\omega$ (which is necessary, e.g., for solution of equation* (2.5)*), direct computation of derivatives and associated accuracy loss does not seem to be avoidable.*

4.6.3 Type IV integral (singular)

As in Section 4.5.3, we utilize a polar change of variables to resolve the Green's function singularity in the canonical type defined in equation (4.15), thus obtaining the expression

$$\mathcal{I}_2^{q,sing}[\phi_2](u_0,v_0) = \int_0^{\pi} \left(\int_{-\frac{v_0}{\sin\theta}}^{\infty} H(u_0,v_0,\rho,\theta) \frac{d\rho}{\sqrt{v_0+\rho\sin\theta}} \right) d\theta, \tag{4.44}$$

where the integrand $H(u_0,v_0,\rho,\theta) = \phi_2(u_0+\rho\cos\theta, v_0+\rho\sin\theta)\frac{|\rho|}{R}$ is a smooth function of ρ and θ, which vanishes for ρ larger than a certain constant ρ_0. While the square-root singularity in the inner-integral can clearly be resolved to high-order by applying an appropriate quadratic change of variable, the outer integrand in θ is not a uniformly smooth function: as detailed in Appendix 4.9.2, it develops a boundary layer as v_0 approaches 0. The analysis presented in Appendix 4.9.2 suggests a simple and efficient method for high-order resolution of this boundary layer—thus leading to accurate evaluation of the integral (4.44). This methodology, which is an integral part of our solver, is described in what follows.

The aforementioned boundary layer integration method is based on use of the change of variables $t = \sqrt{v_0+\rho\sin\theta}$. With this change of variables equation (4.44) becomes

$$\mathcal{I}_2^{q,sing}[\phi_2](u_0,v_0) = \int_0^{\pi} I_{\rho,2}^q[\phi_2](u_0,v_0,\theta)d\theta, \tag{4.45}$$

$$I_{\rho,2}^q[\phi_2](u_0,v_0,\theta) = \int_0^{\infty} H(u_0,v_0,\frac{t^2-v_0}{\sin\theta},\theta)dt. \tag{4.46}$$

The integral (4.46) is evaluated with high-order accuracy by means of a trapezoidal rule in the t variable, for any $0<\theta<\pi$. In order to capture the boundary layer in the outer-integral in (4.45), our algorithm relies on an additional changes of variables $\theta=\alpha^2$ and $\theta=\pi-\alpha^2$, which lead to the expression

$$\int_0^{\pi} I_{\rho,2}^q[\phi_2](u_0,v_0,\theta)d\theta = \int_0^{\sqrt{\frac{\pi}{2}}} \left(I_{\rho,2}^q[\phi_2](u_0,v_0,\alpha^2) - I_{\rho,2}^q[\phi_2](u_0,v_0,\pi-\alpha^2) \right) \alpha d\alpha. \tag{4.47}$$

In view of the analysis presented in Appendix 4.9.2, the boundary layer is confined to the interval $[0,\alpha^*(v_0)]$, where $\alpha^*(v_0) = (\frac{v_0}{d})^{\frac{1}{3}}$, and we therefore decompose the α-integral in the form

$$\int_0^{\sqrt{\frac{\pi}{2}}} \ldots d\alpha = \int_0^{\alpha^*(v_0)} \ldots d\alpha + \int_{\alpha^*(v_0)}^{\sqrt{\frac{\pi}{2}}} \ldots d\alpha. \tag{4.48}$$

For a given error tolerance, our algorithm proceeds by applying Chebyshev integration rules to both integrals in (4.48), using for the second integral a number of integration points that does not depend on v_0, and using for the first integral a number of integration points that grows slowly as v_0 tends to zero. In practice, we have found that a mild logarithmic growth in the number of integration points suffices to give consistently accurate results. In view of such slow required growth, and for the sake of simplicity, the number of integration points used for evaluation of the first integral in (4.48) was taken to be independent of v_0 and sufficiently large to meet prescribed error tolerances; we estimate that a minimal additional computing time results from this practice in all of the examples considered here.

Remark 11. *In order to apply the trapezoidal rule* (4.42) *for evaluation the integral of* (4.46) *we distinguish two cases, as illustrated in Figure 4.10. For* $\frac{\pi}{4} \leq \theta \leq \frac{3\pi}{4}$ *we use the sampling in* t *provided by intersections with the original grid underlying* $\mathcal{P}_2^q$*: the one-dimensional cubic-spline interpolation method introduced in section 4.5.3 can be used to efficiently interpolate the function* $H(\frac{t^2-v_0}{\sin\theta}, \theta)$ *at the needed integration points. For* $0 \leq \theta \leq \frac{\pi}{4}$ *and* $\frac{3\pi}{4} \leq \theta \leq \pi$*, on the other hand, the* t*-sampling provided by the intersections with the original grid is too coarse. In this case, we resort to a full two-dimensional interpolation of the density* ϕ_2 *(see Remark 12) to interpolate to a mesh in the* t *variable which, away from* $t = 0$ *has roughly the same sampling density as that in the overall patch discretization. In practice a fixed number of discretization points is used to discretize all of the* t *integrals considered in the present remark.*

Remark 12. *The two-dimensional interpolation method for smooth functions* $\phi_2(u, v)$*, which is mentioned in Remark 11, proceeds by first performing a two-dimensional Fourier expansion of the function* $\phi_2(u, t^2)$*, by means of FFTs along the* u *variable and FCTs along the* $t = \sqrt{v}$ *variable, followed zero-padding by a factor* P *(in practice we use* $P = 6$*). This procedure results in a spectral approximation of* ϕ_2 *(and, by term-by-term differentiation, of its derivatives as well) on a highly resolved two-dimensional grid. The final interpolation scheme is obtained by building bicubic spline interpolations based on function values and derivatives on each square of the refined grid. [54, p. 195].*

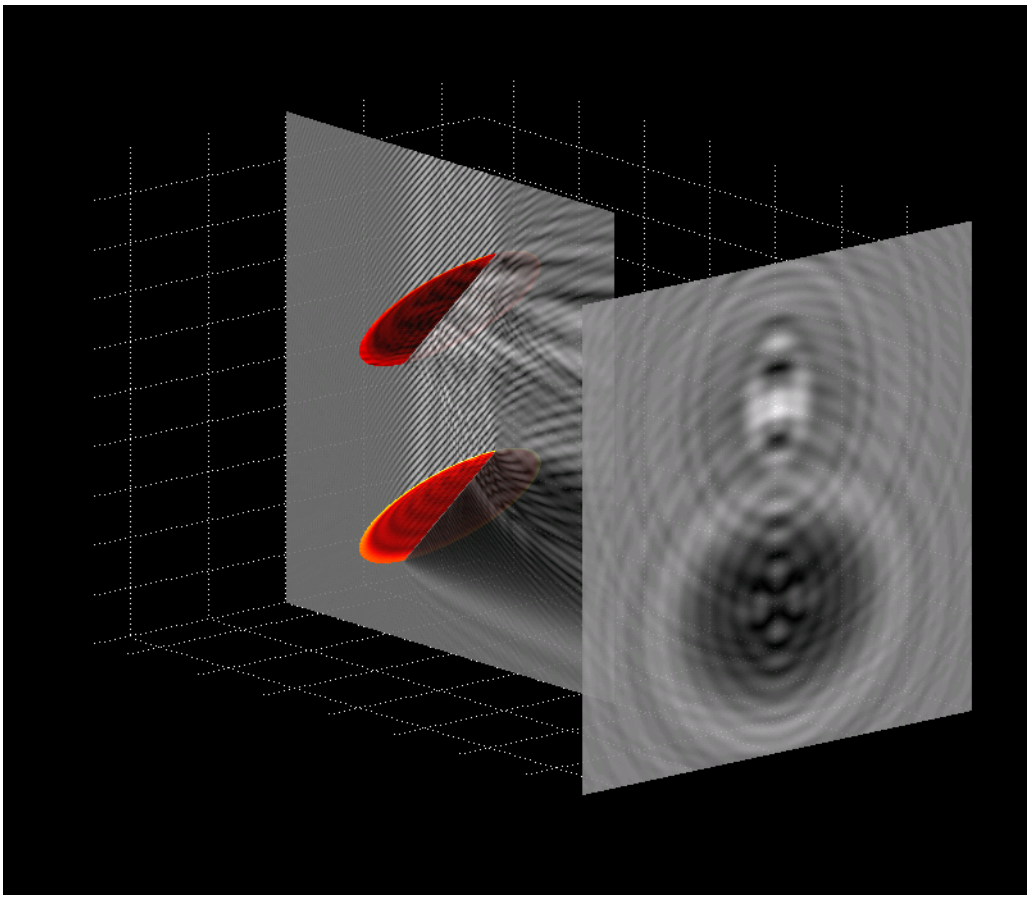

Figure 4.11: Multiple scattering examples: Neumann problem on two parallel discs 24λ in diameter, illuminated at a 45° degree angle. The coloring on the discs represents the values of the surface unknown ψ.

4.6.4 Type VI integral (principal value)

Our algorithm evaluates the principal-value edge-patch Type VI canonical integral $\mathcal{I}_2^{q,pv}$ in a manner similar to that used for Type IV treated in Section 4.6.3: introducing the local polar change of variables around the point $\mathbf{r}$ we obtain

$$\mathcal{I}_2^{q,pv}[\phi_2](u_0,v_0) = \int_0^{\pi} \left(p.v. \int_{\frac{-v_0}{\sin\theta}}^{\infty} \frac{H^T(u_0,v_0,\rho,\theta)}{\rho} \frac{d\rho}{\sqrt{v_0+\rho\sin\theta}} \right) d\theta, \tag{4.49}$$

where

$$H^T(u_0,v_0,\rho,\theta) = \phi_2(u_0+\rho\cos\theta, v_0+\rho\sin\theta)\frac{|\rho|^3}{R^3}\frac{\mathbf{R}.\mathbf{T}}{\rho} \tag{4.50}$$

is again, a smooth function of ρ and θ which vanishes identically for $\rho > \rho_0$. Resorting to the quadratic change of variables $t = \sqrt{v_0 + \rho \sin\theta}$ we obtain

$$\mathcal{I}_2^{q,pv}[\phi_2](u_0, v_0) = \int_0^\pi I_{\rho,2}^{q,pv}[\phi_2](u_0, v_0, \theta) d\theta. \tag{4.51}$$

where the radial integral

$$I_{\rho,2}^{q,pv}[\phi_2](u_0, v_0, \theta) = p.v. \int_0^\infty H^T(u_0, v_0, \frac{t^2 - t_0^2}{\sin\theta}, \theta) \frac{dt}{t^2 - t_0^2}, \quad t_0 = \sqrt{v_0} \tag{4.52}$$

can be expressed in the form

$$I_{\rho,2}^{q,pv} = \text{p.v.} \int_0^\infty \frac{v(t^2)}{t^2 - t_0^2} dt \quad , \quad \text{where } v(t) \text{ is smooth for } t \geq 0 \text{ and vanishes for } t \text{ large enough.} \tag{4.53}$$

Simple algebra then yields

$$I_{\rho,2}^{q,pv} = \text{p.v.} \int_0^\infty v(t^2) \left\{ \frac{1}{t - t_0} - \frac{1}{t + t_0} \right\} dt = \text{p.v.} \int_{-\infty}^\infty \frac{v(t^2)}{t - t_0} dt; \tag{4.54}$$

clearly, the right-hand-side integral in equation (4.54) can be evaluated with high-order accuracy by means of the trapezoidal rule (4.39).

Using this algorithm for evaluation of the integral (4.52) for any fixed value of θ our algorithm for evaluation of the θ integral (4.51), and thus (4.49), is completed, as in Section 4.6.3, by relying on (a) The quadratic change of variable $\theta = \alpha^2$ and (b) The boundary layer split (4.48).

4.7 Parameter Selection

A number of parameters are implicit in the algorithm laid out in Section 4.1, including parameters that relate to the overall surface patching and discretization strategies described in Section 4.1.2 as well as parameters that arise in the polar integration rules introduced in Sections 4.5.3, 4.5.4, 4.6.3 and 4.6.4. Clearly, the values of such parameters have an impact on both, accuracy for a given discretization density, as well as computing time for a given accuracy tolerance. A degree of experimentation is necessary to produce an adequate selection of such parameters for a given problem. Without entering a full description of the choices inherent in our own implementations, in what follows we provide an indication of

the strategies we have used to select two types of parameters, namely, (a) The width of the edge patches (see Figure 4.1), and (b) The number of discretization points used in both the radial and angular directions for each polar integration problem for which the corresponding floating partition of unity does not vanish at the open edge, as illustrated in Figure 4.10. Similar (but simpler) considerations apply to other parameters, such as width of floating partitions of unity, extents of overlap between patches, etc.

With respect to point (a) above we note that, for scattering solutions to be obtained with a fixed accuracy tolerance, the discretization densities must be increased as frequencies are increased, and, thus, the width of the edge patches can be decreased accordingly—in such a way that the number of discretization points in the v direction for each one of the edge patches is kept constant. This strategy is crucial for efficiency, since the edge patches require use of the two-dimensional interpolation method mentioned in Remark 12, which is significantly more costly than the corresponding one-dimensional interpolation method used in the interior patches. Use of constant number of v-discretization points within shrinking edge patches for increasing frequencies thus enables fixed-accuracy evaluation of edge-patch integrals with an overall computing cost that is not dominated by the edge-patch two-dimensional interpolation procedure.

Concerning point (b) above, in turn, as mentioned in Remark 11, we make use of a fixed number of equispaced integration points in the scaled radial variable t (see equation (4.45)) for all values of the angular variable θ. In practice, we select the number of t-integration points to equal the maximum value N_t of the numbers N_u and N_v of points in the u-v discretization mesh that are contained in the $\theta = 0$ and $\theta = \pi/2$ lines, respectively, and which lie within the support of the corresponding floating POU. In order to preserve the wavelength sampling in the angular integral (4.45), finally, the two integrals on the right-hand side of equation (4.48) are evaluated on the basis of the Clenshaw-Curtis quadrature rule [54] using an α discretization mesh containing $\frac{\pi}{2}N_t$ points—since the length of half a circumference equals $\frac{\pi}{2}$ times its diameter.

4.8 Numerical Results

In this section, we present results obtained by means of a C++ implementation of the algorithm outlined in Section 4.1.1, incorporating the canonical operator decompositions

N	$\mathrm{Dir}(\mathbf{S}_\omega)$	$\mathrm{Dir}(\mathbf{N}_\omega\mathbf{S}_\omega)$	$\mathrm{Neu}(\mathbf{N}_\omega)$	$\mathrm{Neu}(\mathbf{N}_\omega\mathbf{S}_\omega)$
$16\times 16+2\times 24\times 16$	2.4×10^{-4}	2.5×10^{-4}	5.0×10^{-4}	2.6×10^{-4}
$32\times 32+2\times 48\times 32$	4.8×10^{-6}	4.8×10^{-6}	5.3×10^{-6}	5.2×10^{-6}
$64\times 64+2\times 98\times 64$	4.7×10^{-8}	9.7×10^{-8}	4.9×10^{-8}	5.1×10^{-8}

Table 4.1: Scattering by a disc of diameter 3λ, similar to the corresponding 24λ simulation depicted in Figure 4.2: maximum errors in the acoustic field on the square projection plate shown in the figure. This table demonstrates spectral convergence for all the formulations considered: doubling the discretization density results in orders-of-magnitude decreases in the numerical error. (The notation $Q_1\times m_1\times n_1+Q_2\times m_2\times n_2$ indicates that a number Q_1 of patches containing $m_1\times n_1$ discretization points together with a number Q_2 of patches containing $m_2\times n_2$ discretization points were used for the corresponding numerical solution.)

introduced in Sections 4.2 through 4.4 for the operators $\mathbf{S}_\omega$, $\mathbf{N}_\omega$ and $\mathbf{N}_\omega\mathbf{S}_\omega$, together with the high-order integration rules put forth in Sections 4.5 and 4.6 and the iterative linear algebra solver GMRES. Errors reported were evaluated through comparisons with highly resolved numerical solutions. Computation times correspond to single-processor runs (on a 2.67 GHz Intel core), *without use of the acceleration methods or parallelization.* As mentioned in Section 4.1.4, application of the acceleration method [17] in the present context does not present difficulties; such extension will be considered in forthcoming work.

4.8.1 Spectral convergence

We demonstrate the spectral properties of our algorithm through an example concerning a canonical geometry, namely, the unit disc

$$x^2+y^2\leq 1,\quad z=0. \tag{4.55}$$

For this surface we utilize three coordinate patches (see Figure 4.1), including a large central patch given by equations $\{x(u,v)=u,\quad y(u,v)=v,\quad z(u,v)=0\}$, and two edge patches parametrized by the equations $\{x(u,v)=(1-v)\cos u,\quad y(u,v)=(1-v)\sin u,\quad z(u,v)=0\}$ for values of u and v in adequately chosen intervals. The two edge-patches overlap as illustrated in Figure 4.1, and their width is defined by the range of the v variable, which, in accordance with Section 4.7, is reduced as the frequency increases. With reference to equation (2.1), the integral weight is set to $\omega=\sqrt{1-x^2-y^2}$.

The sound-soft (Dirichlet) problem can be solved by means of either the first-kind equa-

		Dir($\mathbf{S}_\omega$)			Dir($\mathbf{N}_\omega\mathbf{S}_\omega$)		
Disc Size	Unknowns	It.	Time	ϵ_r	It.	Time	ϵ_r
3λ	4096	6	58s	1.0×10^{-4}	6	5m20s	1.4×10^{-4}
6λ	10240	9	3m5s	8.2×10^{-5}	6	11m14s	5.4×10^{-5}
12λ	28672	13	15m21s	1.2×10^{-4}	7	36m31s	3.7×10^{-4}
24λ	90112	18	2h30m	2.8×10^{-4}	7	3h41m	4.1×10^{-4}

		Neu($\mathbf{N}_\omega$)			Neu($\mathbf{N}_\omega\mathbf{S}_\omega$)		
Disc Size	Unknowns	It.	Time	ϵ_r	It.	Time	ϵ_r
3λ	4096	16	9m21s	1.3×10^{-4}	6	5m50s	1.3×10^{-4}
6λ	10240	28	36m31s	$2. \times 10^{-4}$	6	11m36s	5.8×10^{-5}
12λ	28672	49	2h43m	1.7×10^{-4}	7	37m04s	5.2×10^{-4}
24λ	90112	80	21h10m	1.9×10^{-4}	7	3h51m	6.1×10^{-4}

Table 4.2: Iteration numbers and computing times for the problem of scattering by a disc at normal incidence. Top: Dirichlet problem. Bottom: Neumann problem. In each case, use of the second-kind combined operator $\mathbf{N}_\omega\mathbf{S}_\omega$ gives rise to significantly smaller iteration numbers than the corresponding first-kind formulation. In the case of the Neumann problem, the reduction in iteration numbers results in substantially improved computing times. Note: all reported computing times correspond to *non-accelerated single-processor runs*. Dramatic reductions in computing times would result from use of the acceleration method [17]—see, e.g., the recent contribution [14] for the closed-surface case.

tion (2.4), or the second-kind equation (2.26) which, in what follows, are called Dir($\mathbf{S}_\omega$) and Dir($\mathbf{N}_\omega\mathbf{S}_\omega$), respectively. The sound-hard (Neumann) problem, similarly, can be tackled by means of either the first-kind equation (2.5) or the second-kind equation (2.27); we call these equations Neu($\mathbf{N}_\omega$) and Neu($\mathbf{N}_\omega\mathbf{N}_\omega$), respectively. Table 4.1 demonstrates the high-order convergence of the solutions produced by our implementations for each one of these equations on a disc of diameter 3λ; clearly errors decrease by orders of magnitude as a result of a mere doubling of the discretization density.

4.8.2 Solver performance under various integral formulations

In this section we demonstrate the performance of the open-surface solvers based on use of the operators Dir($\mathbf{S}_\omega$) and Dir($\mathbf{N}_\omega\mathbf{S}_\omega$) for the Dirichlet problem, as well as the operators Neu($\mathbf{N}_\omega$) and Neu($\mathbf{N}_\omega\mathbf{S}_\omega$) for the Neumann problem. We base our demonstrations on two open surfaces: a disc and a spherical cavity defined by

$$x^2 + y^2 + z^2 = 1, \quad z > \cos(\theta_0), \tag{4.56}$$

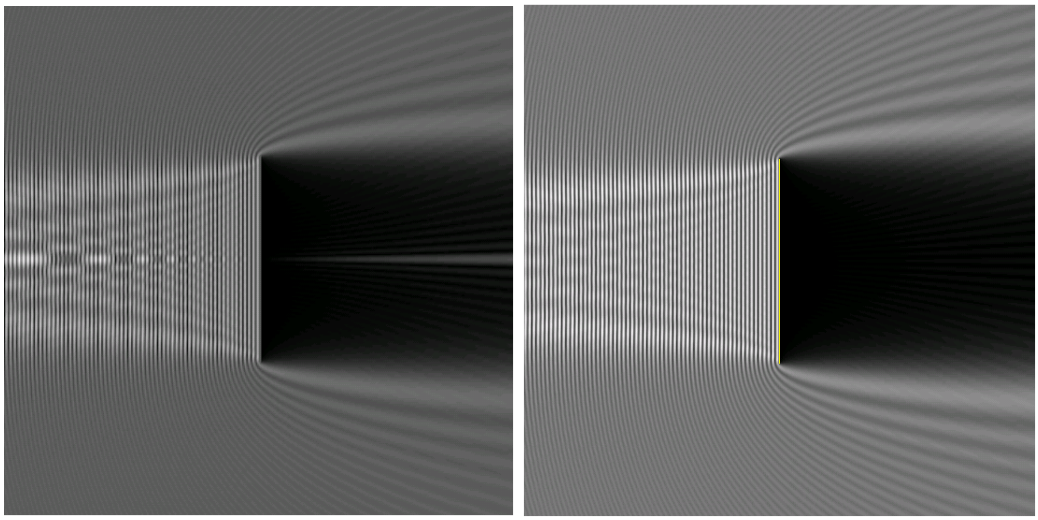

Figure 4.12: Poisson-spot phenomenon. Left: cross-sectional view on a of the diffraction pattern produced by a disc 24λ in diameter in three- dimensional space (Dirichlet problem, normal incidence). Right: Diffraction by an arc of length 24λ in two-dimensional space (Dirichlet problem, normal incidence). Note that only in the three-dimensional case does a "Poisson cone" and corresponding "Poisson spot" develop in the shadow region.

		Dir($\mathbf{S}_\omega$)			Dir($\mathbf{N}_\omega\mathbf{S}_\omega$)		
Spherical Cavity Size	Unknowns	It.	Time	ϵ_r	It.	Time	ϵ_r
3λ	9344	17	7m16s	1.8×10^{-4}	13	1h18m	4.5×10^{-4}
9λ	84096	39	4h06m	2.1×10^{-4}	24	13h20m	2.9×10^{-4}
18λ	336384	65	57h48m	4.0×10^{-4}	43	124h	1.4×10^{-4}

		Neu($\mathbf{N}_\omega$)			Neu($\mathbf{N}_\omega\mathbf{S}_\omega$)		
Spherical Cavity Size	Unknowns	It.	Time	ϵ_r	It.	Time	ϵ_r
3λ	9344	57	1h24m	1.2×10^{-4}	13	1h20m	8.8×10^{-4}
9λ	84096	243	52h14m	$2. \times 10^{-4}$	24	13h21m	5.6×10^{-4}
18λ	336384	> 600	-	-	43	124h	3.1×10^{-4}

Table 4.3: Iteration numbers and computing times for the problem of scattering by the spherical cavity defined by equation (4.56) and depicted in Figures 4.4 and 4.5. Top: Dirichlet problem. Bottom: Neumann problem. Reductions in numbers of iterations and computing times occur as detailed in the caption of Table 4.2, but, owing to the rich multiple scattering phenomena that arise within the cavity, the iteration numbers are significantly higher, in all cavity cases, than those required for the corresponding disc problems.

where θ_0 denotes the cavity aperture. For the examples discussed here we set $\theta_0 = \frac{3\pi}{4}$, and we made use of the weight function $\omega = \sqrt{z - z_0}$ where $z_0 = \cos(\theta_0)$.

For both geometries, computational times and accuracies at increasingly large frequencies are reported in Tables 4.2 and 4.3. In all tables the acronym It. denotes the number

of iterations required to achieve a relative error (in a screen placed at some distance from the diffracting surface) equal to "ϵ_r" (relative the the maximum field value on the screen), and "Time" denotes the total time required by the solver to evaluate the solution. As can be seen from these tables, the equation Neu($\mathbf{N}_\omega$) requires very large number of iterations for the higher frequencies. The computing times required by the low-iteration equation Neu($\mathbf{N}_\omega\mathbf{S}_\omega$) are thus significantly lower than those required by Neu($\mathbf{N}_\omega$). The situation is reversed for the Dirichlet problem: although the equation Dir($\mathbf{N}_\omega\mathbf{S}_\omega$) requires fewer iterations than Dir($\mathbf{S}_\omega$), the total computational cost of the low-iteration equation is significantly higher in this case—since the application of the operator in Dir($\mathbf{S}_\omega$), which, fortunately, suffices for the solution of the Dirichlet problem, is substantially less expensive than the application of the operator in Dir($\mathbf{N}_\omega\mathbf{S}_\omega$). As it happens, at high-frequency, the bulk of the computational time used by our solver is spent on interior-patch work: application of the acceleration method of [17] (see also [14]) would therefore reduce dramatically overall computing times for high-frequency problems.

Figures 4.2 and 4.3 display three-dimensional renderings of patterns of diffraction by the disc under normal incidence with Neumann boundary condition, and under horizontal incidence with Dirichlet boundary condition. Corresponding images for the spherical-cavity problem are presented in Figures 4.4 and 4.5; note the interesting patterns of multiple-scattering and caustics that arise in the cavity interior.

4.8.3 Miscellaneous examples

This section presents a variety of results produced by the open-surface solver introduced in this chapter, including demonstration of well known effects such as the Poisson spot, and applications in classical contexts such as that provided by the Young experiment.

4.8.3.1 Poisson spot

As mentioned in the Introduction, the experimental observation of a bright area in the shadow of the disc, the famous Poisson spot, provided one of the earliest confirmations of the wave-theory models of light. The Poisson spot is clearly visible in the diffraction patterns presented in Figure 4.2 and the left portion of Figure 4.12. The left portion of Figure 4.12 displays a slice of the total field around the disc along the $x - z$ plane, which gives a better view of the Poisson-spot phenomenon: the "Poisson cone" is clearly visible

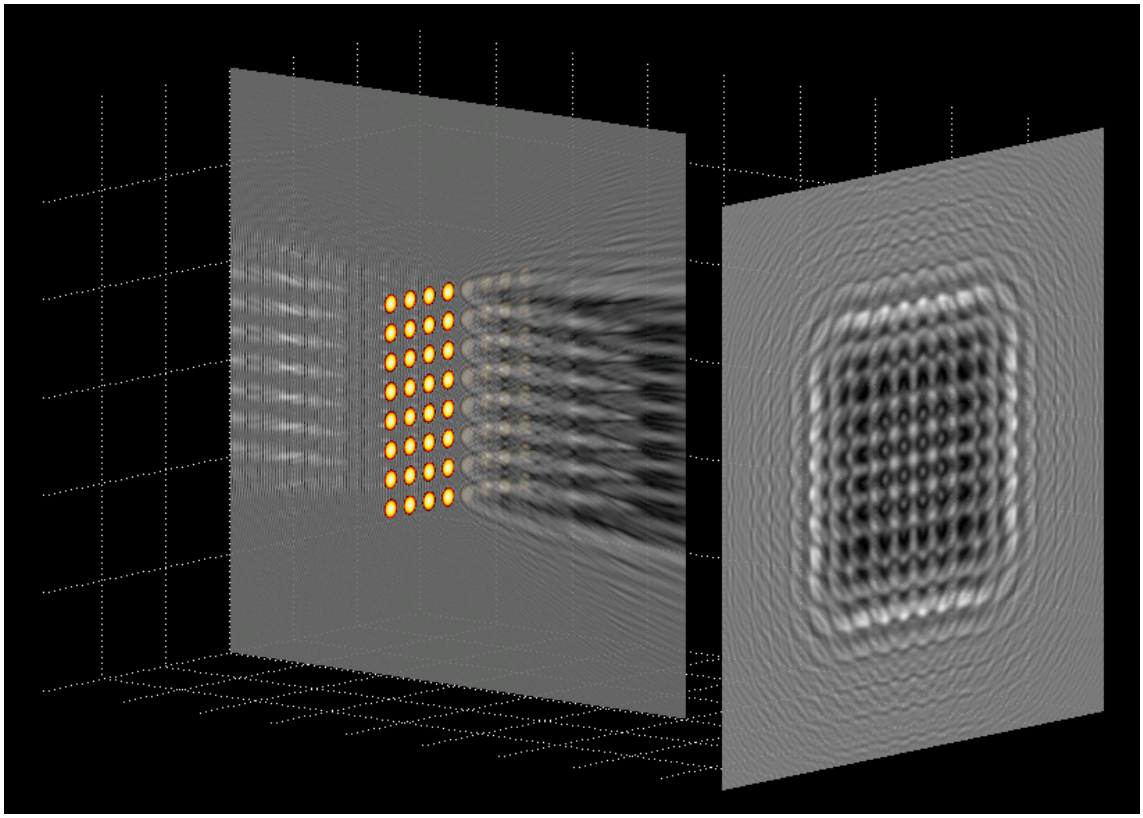

Figure 4.13: Dirichlet problem on an array of 8×8 discs of diameter 6λ (Overall diameter: 96.6λ; 192 patches used). The coloring on the discs represent the values of the surface unknown φ.

in this figure. Interestingly, this phenomenon does not occur in the two-dimensional case. This is demonstrated in the image presented on the right portion of Figure 4.12: the two-dimensional diffraction pattern arising from the flat unit strip (which was obtained by the solver presented in Chapter 3) gives rise to a dark dark shadow area which does not contain a diffraction spot.

4.8.4 Babinet's principle, apertures and Young's experiment

For a flat open surface Γ contained in a plane Π one may consider the corresponding problem of diffraction by the complement $\Gamma^c = \Pi \setminus \Gamma$ of Γ within Π. As is well known, the diffraction pattern resulting from Γ^c can be computed easily, by means of the Babinet principle (see Appendix 4.9.3 and, in particular, equation (4.75)), from a corresponding diffraction pattern associated with the surface Γ. (For ease of reference, a derivation of the Babinet principle for scalar waves is presented in Appendix 4.9.3.) In what follows we present three applications of

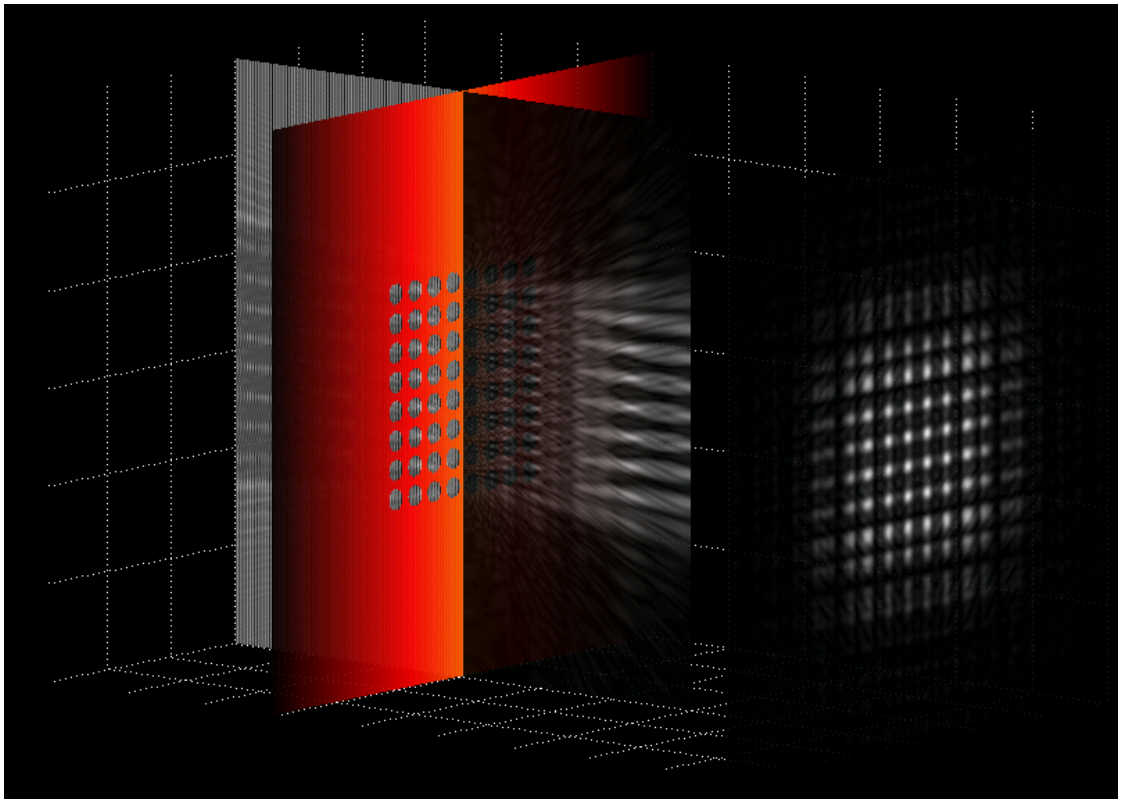

Figure 4.14: Neumann problem for an array of 8×8 circular apertures of diameter 6λ. The diffracted field depicted in this figure was produced by means of Babinet's principle from the diffraction pattern displayed in Figure 4.13. As in Figure 4.6, the coloring on the plane is introduced for visual quality, and does not represent any physical quantity.

the Babinet principle, namely, the diffraction by a circular aperture, the Young phenomenon, and diffraction across an array of apertures (in Section 4.8.4.1).

As our first application of Babinet's principle, in Figure 4.6 we present the field diffracted by a circular aperture which is 24λ in diameter. The incident field for this image was taken to be a point source located at the point $(0, 0, -10)$, outside the region displayed on the figure. In Figure 4.7, we display the total field on screens located behind the aperture at varying distance from the punctured plane. Interestingly, under some configurations a dark spot appears in the center of the bright area, in full accordance with Arago's prediction that a 'Poisson shadow' must exist [52]. As our second application of Babinet's principle, in Figure 4.8 we present the field diffracted by a pair of nearby circular holes in an otherwise perfectly sound-hard plane, under normal plane-wave incidence: this is a setup of the classical Young experiment. This diffraction pattern was produced, by means of Babinet's principle, from a corresponding solution of a Dirichlet problem for two coplanar discs in

space. As in Young's experiment, interference fringes arise: these can be seen clearly on the right-most image in Figure 4.9. Again, sharp dark spots at the center of the circular illuminated areas can be seen in the leftmost image in Figure 4.9.

4.8.4.1 Arrays of scatterers/apertures

Geometries consisting of a number of disjoint open-surface scattering bodies can be treated easily by the solvers introduced in this chapter—since the decomposition in patches inherent in equation (4.1) is not restricted to sets of patches representing a connected surface. The solution for the two-disc diffraction problem presented in the previous section, for example, was obtained in this manner. In what follows we provide a few additional test cases involving composites of open surfaces.

Figure 4.11 presents the solution of a problem of scattering by two parallel discs illuminated at an angle of $\frac{\pi}{4}$, with Neumann boundary conditions. The beam reflected by the bottom disc, which can clearly be traced onto the upper disc, gives rise to a bright area in the projection screen behind that disc. Two final examples concern an array of 64 discs and the corresponding array of 64 circular apertures on a plane—where each disc is 6λ in diameter and the discs are separated by 3λ spacings, for a total array diameter of 96.6λ. The corresponding diffracted fields are presented in Figures 4.13 and 4.14. The solution of the Dirichlet problem for the 64 disc array was obtained in 23 GMRES iterations on a 192 patch geometry representation.

4.9 Appendix to Chapter 4

4.9.1 Expression of the operator $\mathbf{N}_\omega$ in terms of tangential derivatives

In this section, we provide a proof of Lemma 15.

Proof. It suffices to show that the operators on the left- and right-hand sides of equation (4.17) coincide when applied to any smooth function ψ defined on Γ. Following the derivation in [24] for the closed-surface case, we define the weighted double-layer operator

$$\mathbf{D}_\omega[\psi](\mathbf{r}) = \int_\Gamma \frac{\partial G_k(\mathbf{r},\mathbf{r}')}{\partial \mathbf{n}'_\mathbf{r}} \psi(\mathbf{r}')\omega(\mathbf{r}')dS', \tag{4.57}$$

and we evaluate the limit of its gradient as $\mathbf{r}$ tends to Γ. For $\mathbf{r}$ outside Γ, (4.57) can be

expressed in the form

$$\mathbf{D}_\omega[\psi](\mathbf{r}) = -\mathrm{div} \int_\Gamma G_k(\mathbf{r},\mathbf{r}')\psi(\mathbf{r}')\omega(\mathbf{r}')\mathbf{n}_{\mathbf{r}'}dS'. \tag{4.58}$$

Thus, using the identity

$$\mathrm{curl}\ \mathrm{curl} A = -\Delta A + \nabla \mathrm{div}\ A,$$

we obtain

$$\begin{aligned}\nabla\mathbf{D}_\omega[\psi](\mathbf{r}) = k^2 \int_\Gamma G_k(\mathbf{r},\mathbf{r}')\psi(\mathbf{r}')\omega(\mathbf{r}')\mathbf{n}_{\mathbf{r}'}dS' \\ -\mathrm{curl}\ \mathrm{curl} \int_\Gamma G_k(\mathbf{r},\mathbf{r}')\psi(\mathbf{r}')\mathbf{n}_{\mathbf{r}'}dS'.\end{aligned} \tag{4.59}$$

But, for $\mathbf{r}$ outside Γ we have

$$\begin{aligned}\mathrm{curl} \int_\Gamma G_k(\mathbf{r},\mathbf{r}')\psi(\mathbf{r}')\mathbf{n}_{\mathbf{r}'}dS' = \\ \int_\Gamma \left[\mathbf{n}_{\mathbf{r}'}, \psi(\mathbf{r}')\omega(\mathbf{r}')\nabla^s_{\mathbf{r}'}G_k(\mathbf{r},\mathbf{r}')\right] dS',\end{aligned} \tag{4.60}$$

where $[\,\cdot\,,\cdot\,]$ and ∇^s denote the vector product and surface gradient operator, respectively. Integrating by parts the surface gradient (see, e.g., [24, eq. (2.2)]) and noting that the boundary terms vanish in view of the presence of the weight ω, we obtain

$$\begin{aligned}\mathrm{curl} \int_\Gamma G_k(\mathbf{r},\mathbf{r}')\psi(\mathbf{r}')\mathbf{n}_{\mathbf{r}'}dS' = \\ -\int_\Gamma G_k(\mathbf{r},\mathbf{r}') \left[\mathbf{n}_{\mathbf{r}'}, \nabla^s \left(\psi(\mathbf{r}')\omega(\mathbf{r}')\right)\right] dS'.\end{aligned} \tag{4.61}$$

In the limit as $\mathbf{r}$ tends to an interior point in Γ we therefore obtain the expression

$$\begin{aligned}\nabla\mathbf{D}_\omega[\psi](\mathbf{r}) = k^2 \int_\Gamma G_k(\mathbf{r},\mathbf{r}')\psi(\mathbf{r}')\omega(\mathbf{r}')\mathbf{n}_{\mathbf{r}'}dS' \\ +\mathrm{p.v.} \int_\Gamma \left[\nabla_{\mathbf{r}} G_k(\mathbf{r},\mathbf{r}'), \left[\mathbf{n}_{\mathbf{r}'}, \nabla^s \left(\psi(\mathbf{r}')\omega(\mathbf{r}')\right)\right]\right] dS' \qquad (\mathbf{r}\in\Gamma),\end{aligned} \tag{4.62}$$

in terms of a principal value integral, for the surface values of the gradient of the double-layer operator $\mathbf{D}_\omega$. Taking the scalar product with $\mathbf{n}_\mathbf{r}$ on both sides of (4.62) now yields the desired result: equation (4.17).

□

4.9.2 Boundary-layer character of the inner integral in equation (4.44)

In order to demonstrate the difficulties inherent in the numerical evaluation of the outer integral in equation (4.44) we consider the integration problem

$$\int_0^{\pi} \tilde{I}_\rho(v_0, \rho_0, \theta) d\theta, \tag{4.63}$$

in which the (u_0, v_0)-dependent inner integral in (4.44) is substituted by the v_0-dependent integral

$$\tilde{I}_\rho(v_0, \rho_0, \theta) = \int_{-\frac{v_0}{\sin\theta}}^{\infty} \tilde{H}_{\rho_0}(\rho, \theta) \frac{d\rho}{\sqrt{v_0 + \rho \sin\theta}} \quad , \quad 0 \le \theta \le \pi. \tag{4.64}$$

Here

$$\tilde{H}_{\rho_0}(\rho, \theta) = \begin{cases} 1, & |\rho| < \rho_0 \\ 0, & |\rho| \ge \rho_0, \end{cases} \tag{4.65}$$

so that, in the present example, ρ_0 is the polar-integration radius. (The inner integral in (4.44) varies smoothly with u_0, and, thus, the u_0 dependence does not need to be built into the present analogy.) The integral $\tilde{I}_\rho(v_0, \rho_0, \theta)$ is given by

$$\tilde{I}_\rho(v_0, \rho_0, \theta) = \begin{cases} \frac{2\rho_0}{\sqrt{v_0 + \rho_0 \sin\theta} + \sqrt{v_0 - \rho_0 \sin\theta}} & \text{if} \quad \sin\theta \le \frac{v_0}{\rho_0} \\ \\ 2\frac{\sqrt{\frac{v_0}{\sin\theta} + \rho_0}}{\sqrt{\sin\theta}} & \text{if} \quad \sin\theta > \frac{v_0}{\rho_0}. \end{cases} \tag{4.66}$$

Clearly, as v_0 tends to zero, $\tilde{I}(v_0, \rho_0, \theta)$ becomes increasingly singular (as demonstrated in the left portion of Figure 4.15): in view of the last equation on the right-hand-side of (4.66), we have

$$\lim_{v_0 \to 0} \tilde{I}_\rho(v_0, \rho_0, \theta) = \left(\frac{1}{\sqrt{\sin\theta}} \right). \tag{4.67}$$

To treat the singularity in (4.67) we introduce quadratic changes of variables in the θ integration in equation (4.63)—of the form $\theta = \alpha^2$ in the interval $[0, \frac{\Pi}{2}]$ and $\theta = \Pi - \alpha^2$ in the interval $[\frac{\pi}{2}, \pi]$). As a result of these operations we obtain bounded integrands: for example, the integrand resulting from the first of these changes of variables is $\tilde{J}(v_0, \rho_0, \alpha) = \alpha \tilde{I}(v_0, \rho_0, \alpha^2)$, which is a bounded function of α. This integrand is depicted on the right portion of Figure 4.15; clearly $\tilde{J}(v_0, \rho_0, \alpha)$ develops a boundary layer as v_0 tends to zero.

The two changes of variables mentioned above result in integrals over the domain

$[0, \sqrt{\frac{\pi}{2}}])$, and in both cases boundary layers result at and around $\alpha = 0$. To resolve these boundary layers we decompose the integration interval into two subintervals, namely $[0, \alpha^*(v_0, \rho_0)]$ and $[\alpha^*(v_0, \rho_0), \sqrt{\frac{\pi}{2}}]$. Here, for a given value of v_0, the point $\alpha^*(v_0, \rho_0)$ is chosen to lie to right of the coordinate for which the peak occurs in the right portion of Figure 4.15, in such a way that the slope of the function $\tilde{J}(v_0, \rho_0, \alpha)$ as a function of α at $\alpha = \alpha^*(v_0, \rho_0)$ remains constant as v_0 approaches zero—with a slope that equals a certain user-prescribed constant value. In practice we have found that the integral to the right of the point $\alpha = \alpha^*(v_0, \rho_0)$ can be performed, with fixed accuracy, by means of a number of discretization points that grows very slowly as $v_0 \to 0$. (In our implementations we typically use a number of discretization points to evaluate this integral that remains constant for all required small values of v_0.) The evaluation of the integral on the left of the point $\alpha = \alpha^*(v_0, \rho_0)$ with fixed accuracy requires a number of discretization points that does grow somewhat faster, as $v_0 \to 0$, than the one on the right, but, we have found in practice that the latter integral can be obtained with fixed accuracy by means of a number of discretization points that grows only logarithmically with v_0 as $v_0 \to 0$.

To obtain an approximate expression for $\alpha^*(v_0, \rho_0)$ we note that, since

$$\tilde{J}(v_0, \rho_0, \alpha) = \alpha \frac{\sqrt{v_0 + \rho_0 \sin \alpha^2}}{\sin \alpha^2} \quad \text{for} \qquad \alpha > \sqrt{\arcsin(\frac{v_0}{\rho_0})}, \tag{4.68}$$

for $\alpha \ll 1$ and for sufficiently small values of v_0 (such that the inequality constraint in (4.68) is satisfied) we have $\alpha^2 \sim \sin \alpha^2$, and thus letting $\eta = \frac{v_0}{\rho_0}$,

$$\tilde{J}(v_0, \rho_0, \alpha) \sim \sqrt{\rho_0} f_n(\alpha) \quad \text{where} \quad f_\eta(\alpha) = \frac{\sqrt{\eta + \alpha^2}}{\alpha}. \tag{4.69}$$

It follows that, for a given constant $C > 0$, the fixed-slope point α_η for which $f'_\eta(\alpha_\eta) = -C$ is approximately given as a root of the equation

$$-\frac{\eta}{\alpha_\eta^2 \sqrt{\eta + \alpha_\eta^2}} = -C, \quad \text{or equivalently,} \quad \frac{\alpha_\eta^4}{\eta} + \frac{\alpha_\eta^6}{\eta^2} - \frac{1}{C^2} = 0. \tag{4.70}$$

Clearly, thus, an approximation of the quantity α_η^2 can be obtained, in closed form, as a root of a certain polynomial of degree three. A Taylor expansion of the resulting root as a

function of η around $\eta = 0$ shows that

$$\alpha_\eta = O\left(\eta^{\frac{1}{3}}\right) \quad \text{as} \quad \eta \to 0, \tag{4.71}$$

and, since $\eta = \frac{v_0}{\rho_0}$, it follows that the constant slope point $\alpha^*(v_0, \rho_0)$ is given, for each constant ρ_0, by

$$\alpha^*(v_0, \rho_0) \sim v_0^{\frac{1}{3}} \quad \text{as} \quad v_0 \to 0. \tag{4.72}$$

.

Since the function $H = H(u_0, v_0, \rho, \theta)$ in equation (4.44) is modulated by a smooth windowing function that is akin to the "discontinuous window function" $\tilde{H}_{\rho_0}$ in equation (4.66), it is reasonable to expect that the inner ρ-integral in (4.44) gives rise to a α-integrand which develops a similarly behaved, albeit smoother, boundary layer. We illustrate this in Figure 4.16 (the left portion of which should be compared to the right portion of Figure 4.15), which displays the function

$$J(v_0, \rho_0, \alpha) = \alpha \int_{-\frac{v_0}{\sin \alpha^2}}^{\infty} H(v_0, \rho, \alpha^2) \frac{\rho_0 \rho}{\sqrt{v_0 + \rho_0 \sin \alpha^2}}, \tag{4.73}$$

where

$$H_{\rho_0}(\rho, \theta) = W(\frac{\rho}{\rho_0}), \quad W(\rho) = \begin{cases} e^{-\frac{1}{1-\rho^2}}, & \rho < 1 \\ 0, & \rho \geq 1. \end{cases} \tag{4.74}$$

It follows that the θ-integration strategy outlined above in this section for the function $\tilde{I}$ (based on the change of variables $\theta = \alpha^2$ and partitioning of integration intervals at the point $\alpha = \alpha^*$) applies to the integrand given by the inner integral in equation (4.44): this strategy is incorporated as part of our algorithm, and is thus demonstrated in the numerical examples presented in Section 4.8.

4.9.3 Babinet principle for acoustic problems

As mentioned in Section 4.8.4, for ease of reference, in this appendix we present a derivation of the Babinet principle for scalar waves; see also [9]. Let Γ be an open (bounded) flat screen which lies in the $z = 0$ plane, and let u^i and u^s_Γ denote the incident wave (with sources contained in the semispace $z < 0$), and the corresponding field scattered by Γ under the Dirichlet boundary condition given by equation (1.31) with $f = -u^i_{|\Gamma}$. The corresponding

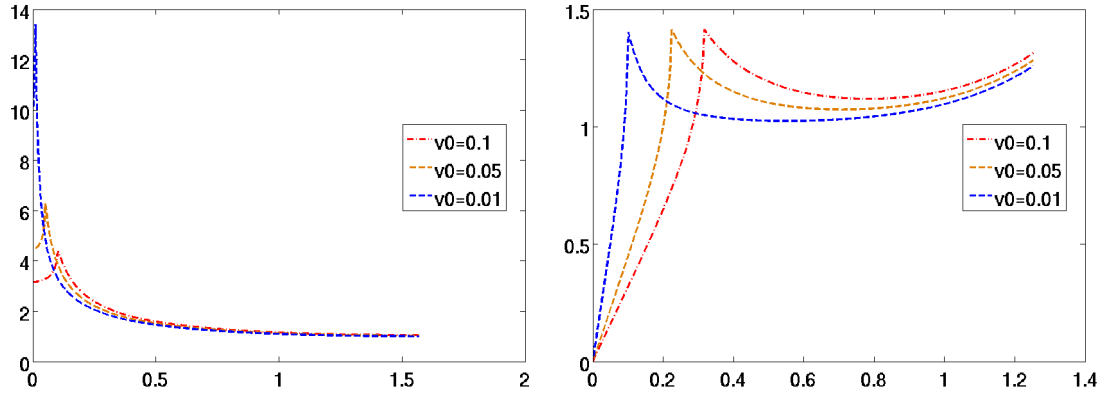

Figure 4.15: Left: boundary layer for $\tilde{I}(v_0, \rho_0, \theta)$ on the interval $[0, \frac{\pi}{2}]$. Right: quadratic regularization $\tilde{J}(v_0, \rho_0, \alpha) = \alpha \tilde{I}(v_0, \rho_0, \alpha^2)$, where $\alpha \in [0, \sqrt{\frac{\pi}{2}}]$

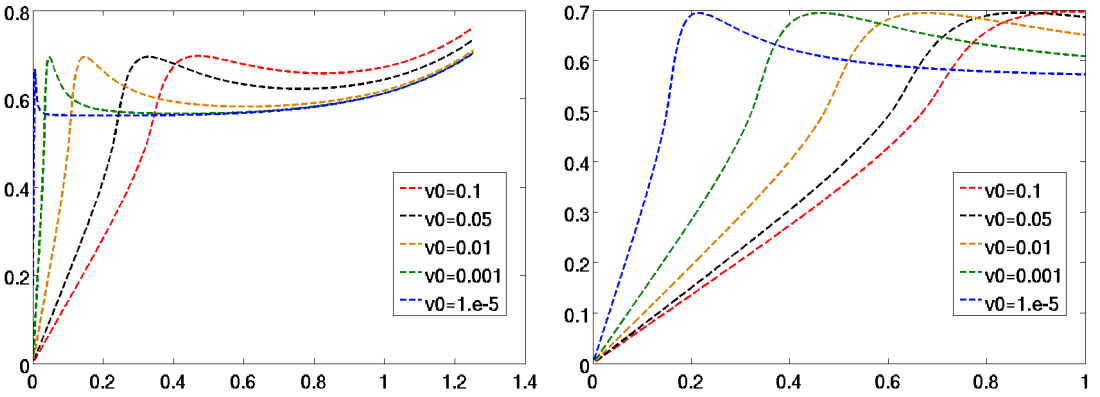

Figure 4.16: Left: numerical values of $J(v_0, \rho_0, \alpha)$ for the smooth function $H_{\rho_0}(\rho, \theta)$ given in equation (4.74). Right: normalized view on the interval $[0, \alpha^*(v_0)]$ for various values of v_0

total field is denoted as $u_\Gamma^T = u^i + u_\Gamma^s$.

Calling Γ^c the complement of Γ in the $z = 0$ plane, let $v_{\Gamma^c}^s$ denote the field scattered by Γ^c under Neumann boundary conditions, and let $v_{\Gamma^c}^T$ denote the corresponding total field. We now establish the Babinet principle that relates the Dirichlet-screen problem to the Neumann aperture problem, namely

$$u_\Gamma^T + v_{\Gamma^c}^T = u^i \quad \text{for} \quad z > 0, \tag{4.75}$$

with an associated formula, given below, for $z < 0$. The corresponding Babinet principle relating the Neumann-Screen problem to the Dirichlet-aperture problem follows similarly.

In the Dirichlet-screen/Neumann-aperture problem the total field $v_{\Gamma^c}^T$ satisfies $v_{\Gamma^c}^T = u^i$

on Γ—since $v^T_{\Gamma^c} = u^i + v^s_{\Gamma^c}$, and since $v^s_{\Gamma^c}$ is an odd function of z (as it equals a double-layer potential with source density on Γ^c). Thus, defining $w(x, y, z) = v^T_{\Gamma^c}(x, y, z)$ for $z > 0$, and $w(x, y, z) = v^T_{\Gamma^c}(x, y, -z)$ for $z < 0$, we see that w satisfies the following properties:

— The boundary values of w on Γ satisfy $w_{|\Gamma} = u^i_{|\Gamma}$.

— w is a radiative solution in $\mathbb{R}^3$ (since $v^T_{\Gamma^c}$ is radiating behind the screen).

— w is continuous across Γ^c (by definition) and its normal derivative across Γ^c is continuous (since $v^T_{\Gamma^c}$ satisfies homogeneous Neumann boundary conditions on Γ^c).

It follows that $w = -u^s_\Gamma$ (by uniqueness of solution to the Dirichlet problem on Γ) and, therefore, that $v^T_{\Gamma^c} = -u^s_\Gamma$ for $z > 0$ or, in other words, that $v^s_{\Gamma^c} = -u^s_\Gamma - u^i$ for $z > 0$—and thus equation (4.75) follows. Since, as stated above, $v^s_{\Gamma^c}$ is an odd function, its values in the region $z < 0$ follow by symmetry.

Chapter 5

Conclusions and Future Work

We have introduced a new framework consisting of a set of regularized first- and second-kind integral equations, with a corresponding theoretical analysis in the two-dimensional case, and associated high-order numerical algorithms for the solution of scalar problems of diffraction by open surfaces in two- and three-dimensional space. The new open-surface solvers are the first ones in the literature that produce high-order solutions in reduced number of GMRES iterations for general (smooth) open surfaces and arbitrary frequencies. In both, the three- and two-dimensional cases, the second-kind formulations Neu($\mathbf{N}_\omega\mathbf{S}_\omega$) and TM($\tilde{N}\tilde{S}$) are highly beneficial in the context of the Neumann problem, as they require computing times that are orders-of-magnitude shorter than those required by the alternative hypersingular formulation Neu($\mathbf{N}_\omega$) and TM($\tilde{N}$) . Such gains do not occur for the Dirichlet problem: the proposed solvers produce high-order solutions to Dir($\mathbf{S}_\omega$) and TE($\tilde{S}$) in very short computational times, and the gains in iteration numbers that result from use of the formulations Dir($\mathbf{N}_\omega\mathbf{S}_\omega$) and TE($\tilde{N}\tilde{S}$) do not suffice to compensate for the significantly higher cost required for evaluation of the combined operator $\mathbf{N}_\omega\mathbf{S}_\omega$.

While the framework presented here lays a solid foundation for the resolution of open-surface scattering problems, much remains to be done. On one hand, we expect that extension of the theoretical work to three-dimensional problems and to the full Maxwell equations should prove fruitful. As a first immediate next step in terms of numerical implementations, in turn, the solvers should be accelerated via the techniques described in [14, 17]; we anticipate that the acceleration will enable very fast calculations on open scatterers at least an order of magnitude larger than those presented in this contribution. To reach even higher-frequency regimes, it will be necessary to explore the extension of the high-frequency methodology introduced in [15] by developing the correct Ansatz for the density

solutions of our weighted integral equations. The scalar work presented here should also be generalized to the full electromagnetic problem, by defining appropriate weighted operators which correctly capture the well-know singular behavior of the open-surface currents; such work is currently ongoing within Professor Bruno's group. The generalization of the method to treat screens with corners (such as large conducting rectangular plates) also deserves investigation: the work presented here, while resolving the edge-singularity, is limited to open-surfaces with *smooth edges*. Finally, the methods developed in this contribution should allow the undertaking of a comprehensive program to assess the validity and numerical accuracy of traditional approximation methods such as those mentioned in the introduction of this thesis: from Kirchhoff's formula to Keller's theory.

In sum, a rigorous numerical framework now exists which should facilitate a richer exploration of the phenomenon of diffraction to a level of precision which was unachievable until now. We hope that a further understanding of the physics of diffraction will follow as a consequence of this work and its natural continuations.

Bibliography

[1] X. Antoine, A. Bendali, and M. Darbas. Analytic preconditioners for the boundary integral solution of the scattering of acoustic waves by open surfaces. *J. Comput. Acoust.*, 13(3):477–498, 2005.

[2] K. Atkinson and I. Sloan. The numerical solution of first-kind logarithmic-kernel integral equations on smooth open arcs. *Math. Comp.*, 56(193):119–139, 1991.

[3] I. Babuška and S. Sauter. Is the pollution effect of the FEM avoidable for the Helmholtz equation considering high wave numbers? *SIAM Rev.*, 42(3):451–484, 2000. Reprint of SIAM J. Numer. Anal. **34** (1997), no. 6, 2392–2423 [MR1480387 (99b:65135)].

[4] H. A. Bethe. Theory of diffraction by small holes. *Phys. Rev. (2)*, 66:163–182, 1944.

[5] E. Bleszynski, M. Bleszynski, and T. Jaroszewicz. AIM: Adaptive integral method for solving large-scale electromagnetic scattering and radiation problems. *Radio Sci.*, 31(5):1225–1251, 1996.

[6] M. Born and E. Wolf. *Principles of Optics.* Cambridge University Press, seventh edition, 2002.

[7] C. J. Bouwkamp. A note on singularities occurring at sharp edges in electromagnetic diffraction theory. *Physica XII*, 7, 1946.

[8] C. J. Bouwkamp. On Bethe's theory of diffraction by small holes. *Philips Research Rep.*, 5:321–332, 1950.

[9] C. J. Bouwkamp. Diffraction theory. *Reports on Progress in Physics*, 17:35–100, 1954.

[10] J.J. Bowman, Senior T.B.A., and P.L.E. Uslenghi. *Electromagnetic and acoustic scattering by simple shapes.* North-Holland Pub. Co, New York, 1969. First Edition.

[11] H. Brakhage and P. Werner. über das dirichletsche aussenraum problem für die helmhotzsche schwingungsgleichung. *Arch. Math.*, 16:325–329, 1965.

[12] A. Brown, P. R. Halmos, and A. L. Shields. Cesàro operators. *Acta Sci. Math. (Szeged)*, 26:125–137, 1965.

[13] O. Bruno, T. Elling, R. Paffenroth, and C. Turc. Electromagnetic integral equations requiring small numbers of krylov-subspace iterations. *Journal of Computational Physics*, 2009.

[14] O. P. Bruno, T. Elling, and Turc C. Regularized integral equations and fast high-order solvers for sound-hard acoustic scattering problems. *Int. J. Numer. Meth. Engng., In press*, 2012.

[15] O. P. Bruno, C. A. Geuzaine, J. A. Monro, and F. Reitch. Prescribed error tolerances within fixed computational times for scattering problems of arbitrarily high frequency: The convex case. *Phil. Trans. R. Soc. Lond. A*, pages 629–645, 2004.

[16] O. P. Bruno and M. Haslam. Regularity theory and superalgebraic solvers for wire antenna problems. *SIAM J. Sci. Comput.*, 29(4):1375–1402, 2007.

[17] O. P. Bruno and L. Kunyansky. A fast, high-order algorithm for the solution of surface scattering problems: basic implementation, tests, and applications. *J. Comput. Phys.*, 169(1):80–110, 2001.

[18] O. P. Bruno and L. A. Kunyansky. A fast high-order algorithm for the solution of surface scattering problems: Basic implementation, tests, and applications. *Journal of Computational Physics*, pages 80–110, 2001.

[19] Flammer C. The vector wave function of the diffraction of electromagnetic waves by circular disks and apertures. I. oblate spheroidal vector wave functions. *J. Appl. Phys.*, 24:1218–1223, 1953.

[20] Flammer C. *Spheroidal wave Functions*. Stanford University Press, 1957.

[21] R. Cecchini and G. Pelosi. Diffraction: the first recorded observation. *IEEE, Antennas and Propagation Magazine*, 32:27–30, 1990.

[22] S. H. Christiansen and J.-C. Nédélec. Preconditioners for the boundary element method in acoustics. In *Mathematical and numerical aspects of wave propagation (Santiago de Compostela, 2000)*, pages 776–781. SIAM, Philadelphia, PA, 2000.

[23] P. Ciarlet and J. L. Lions. *Handbook of numerical analysis, Vol. II, Finite element methods (Part 1).* North-Holland, 1991.

[24] D. Colton and R. Kress. *Integral Equation Methods in Scattering Theory.* John Wiley & Sons, 1983.

[25] D. Colton and R. Kress. *Inverse Acoustic and Electromagnetic Scattering Theory.* Springer, 1997.

[26] M. Costabel. Boundary integral operators on lipschitz domains: Elementary results. *SIAM J. Math. Anal.*, pages 613–626, 1988.

[27] A. Erdélyi, W. Magnus, F. Oberhettinger, and F. Tricomi. *Higher transcendental functions. Vol. II.* Robert E. Krieger Publishing Co. Inc., Melbourne, Fla., 1981. Based on notes left by Harry Bateman, Reprint of the 1953 original.

[28] I. S. Gradshteyn and I. M. Ryzhik. *Table of integrals, series, and products.* Academic Press Inc., San Diego, CA, sixth edition, 2000. Translated from the Russian, Translation edited and with a preface by Alan Jeffrey and Daniel Zwillinger.

[29] P. Grisvard. *Boundary Value Problems in Non-Smooth Domains.* Pitman, 1985.

[30] R. F. Harrington. *Field Computation by Moment Methods.* MacMillan Company, 1968.

[31] N. Heuer, M. Maischak, and E. P. Stephan. Exponential convergence of the $hp-$version for the boundary element method on open surfaces. *Numer. Math.*, 83:641–666, 1999.

[32] N. Heuer, M. E. Mellado, and E. P. Stephan. A $p-$adaptive algorithm for the bem with the hypersingular operator on the plane screen. *Int. J. for Num. Meth. in Eng.*, 53:85–104, 2002.

[33] George C. Hsiao, Ernst P. Stephan, and Wolfgang L. Wendland. On the Dirichlet problem in elasticity for a domain exterior to an arc. *J. Comput. Appl. Math.*, 34(1):1–19, 1991.

[34] Keller J. Geometrical theory of diffraction. *J. Optic. Soc. Am.*, 52(2):116–130, 1962.

[35] J. D. Jackson. *Classical Electrodynamics*. Wiley, 1999.

[36] L. Jameson. High order schemes for resolving waves: Number of points per wavelength. *J. Sci. Comput.*, 15(4):417–433, 2000.

[37] S. Jiang and V. Rokhlin. Second kind integral equations for the classical potential theory on open surfaces. II. *J. Comput. Phys.*, 195(1):1–16, 2004.

[38] J. B. Keller. Rays, waves, and asymptotics. *American Mathematical Society*, 84(5), 1978.

[39] R. Kress. *Linear integral equations*, volume 82 of *Applied Mathematical Sciences*. Springer-Verlag, New York, second edition, 1999.

[40] R. Kussmaul. Ein numerisches Verfahren zur Lösung des Neumannschen Neumannschen Aussenraumproblems für die Helmholtzsche Schwingungsgleichung. *Computing (Arch. Elektron. Rechnen)*, 4:246–273, 1969.

[41] J.-L. Lions and E. Magenes. *Non-homogeneous boundary value problems and applications. Vol. I.* Springer-Verlag, New York, 1972. Translated from the French by P. Kenneth, Die Grundlehren der mathematischen Wissenschaften, Band 181.

[42] R. Duduchava M. Costabel, M. Dauge. Asymptotics without logarithmic terms for crack problems. *Communications in PDE*, pages 869–926, 2003.

[43] Erich Martensen. Über eine Methode zum räumlichen Neumannschen Problem mit einer Anwendung für torusartige Berandungen. *Acta Math.*, 109:75–135, 1963.

[44] J. C. Mason and D. C. Handscomb. *Chebyshev polynomials*. Chapman & Hall/CRC, Boca Raton, FL, 2003.

[45] A.-W. Maue. Zur Formulierung eines allgemeinen Beugungsproblems durch eine Integralgleichung. *Z. Physik*, 126:601–618, 1949.

[46] J. Meixner. Theorie der Beugung elektromagnetischer Wellen an der vollkommen leitenden Kreisscheibe und am vollkommen leitenden ebenen Schirm mit kreisförmiger Öffnung. *Nachr. Akad. Wiss. Göttingen. Math.-Phys. Kl. Math.-Phys.-Chem. Abt.*, 1946:74–75, 1946.

[47] J. Meixner. Die Kantenbedingung in der Theorie der Beugung elektromagnetischer Wellen an vollkommen leitenden ebenen Schirmen. *Ann. Physik (6)*, 6:2–9, 1949.

[48] D. Mitrovic and D. Zubrinic. *Fundamentals of applied functional analysis.* Addison Wesley Longman Limited, 1998.

[49] L. Mönch. On the numerical solution of the direct scattering problem for an open sound-hard arc. *J. Comput. Appl. Math.*, 71(2):343–356, 1996.

[50] J. C. Nedelec. *Notions sur les techniques d'éléments finis.* Publications SMAI, 1991.

[51] JC. Nédélec. *Acoustic and electromagnetic equations*, volume 144 of *Applied Mathematical Sciences.* Springer-Verlag, New York, 2001.

[52] D. Pestre. La tache de poisson fit triompher fresnel. *La Recherche.*

[53] A. Ya. Povzner and I. V. Suharevskiĭ. Integral equations of the second kind in problems of diffraction by an infinitely thin screen. *Soviet Physics. Dokl.*, 4:798–801, 1960.

[54] W. H. Press, Teukolsky S., W. Vetterling, and B. Flannery. *Numerical Recipes in C.* Cambridge University Press, 1992. Second Edition.

[55] V. Rokhlin. Diagonal forms of translation operators for the Helmholtz equation in three dimensions. *Appl. Comput. Harmon. Anal.*, 1(1):82–93, 1993.

[56] Y. Saad and M. H. Schultz. GMRES: a generalized minimal residual algorithm for solving nonsymmetric linear systems. *SIAM J. Sci. Statist. Comput.*, 7(3):856–869, 1986.

[57] A. Sommerfeld. Mathematische Theorie der Diffraction. *Math. Ann.*, 47(2-3):317–374, 1896.

[58] E. Stephan. Boundary integral equations for mixed boundary value problems, screens and transmission problems in $\mathbb{R}^3$. *Habilitationsscrhift*, 1984.

[59] E. Stephan. Boundary integral equations for screen problems in $\mathbf{R}^3$. *Integral Equations Operator Theory*, 10(2):236–257, 1987.

[60] E. Stephan and T. Tran. Domain decomposition algorithms for indefininte hypersingular integral equations: the h and p versions. *SIAM J. Sci. Comp.*, 19(4):1139–1153, 1998.

[61] E. Stephan and W. Wendland. An augmented Galerkin procedure for the boundary integral method applied to two-dimensional screen and crack problems. *Applicable Anal.*, 18(3):183–219, 1984.

[62] E. P. Stephan. Multilevel methods for the h', $p-$, and $hp-$ versions of the boundary element method. *Journal of Computational and Applied Mathematics*, pages 503–519, 2000.

[63] A Taflove. *Computational Electrodynamics: The Finite-Difference Time-Domain Method, Third Edition.* Artech House Publishers, 2005.

[64] F. G. Tricomi. *Integral equations.* Dover Publications Inc., New York, 1985. Reprint of the 1957 original.

[65] W. L. Wendland and E. P. Stephan. A hypersingular boundary integral method for two-dimensional screen and crack problems. *Arch. Rational Mech. Anal.*, 112(4):363–390, 1990.

[66] Y. Yan and I. H. Sloan. On integral equations of the first kind with logarithmic kernels. *J. Integral Equations Appl.*, 1(4):549–579, 1988.

[67] L. Ying, G. Biros, and D. Zorin. A high-order 3D boundary integral equation solver for elliptic PDEs in smooth domains. *J. Comput. Phys.*, 219(1):247–275, 2006.